DIPLOMARBEIT

Dosimetric characteristic of an amorphous silicon based Electronic Portal Imaging Device and verification of Intensity Modulated Radiation Therapy Plans

Ausgeführt am

Atominstitut der österreichischen Universitäten

der Technischen Universität Wien

unter Anleitung von:

O. Univ. Prof. DI Dr. Hannes Aiginger (ATI)

Ass. Prof. DI Dr. Karin Poljanc (ATI)

und

DI Norbert Zagler

Landesklinikum Wiener Neustadt

durch

Lukas Jägerhofer

Komarigasse 17b

2700 Wiener Neustadt

Wien, September 2008

Acknowledgements

I would like to thank my parents Anneliese and Manfred, who gave me emotional and financial support during my academic studies.

Of course I want to thank Univ. Prof. D.I. Dr. Hannes Aiginger (ATI) and D.I. Michael Vejda (LK Wiener Neustadt), who made it possible to work on my thesis in their departments.

I really want to thank Ass. Prof. D.I. Dr. Karin Poljanc (ATI) and D.I. Norbert Zagler (LK Wiener Neustadt) for their supervision, for their time, and their intellectual support.

Last but definitely not least I would like to thank my girlfriend Eva-Maria, who supported me, listened to me when I had problems and helped me to relax when I was stressed out.

Contents

Contents

Contents

Abstract

Intensity modulated radiation therapy (IMRT) is today among the most advanced techniques in radiation therapy. This technique enables the dose distribution in the body to be modelled very accurately in three dimensions. Compared to conventional and conformal radiation therapy it allows to deposit more dose in the target volume and reduce the dose in healthy tissue around the tumour.

Due to complex fields in IMRT it is necessary to verify the fields of the IMRT plans at a high resolution. With an amorphous electronic portal imaging device, like the aS1000 by Varian, it is possible to measure dose distributions produced by IMRT fields in real time.

Goal of this thesis was to introduce a Varian aS1000 EPID for verification of IMRT plans into the department of oncology at the Landesklinikum Wiener Neustadt. Therefore the device had to be calibrated for absolute dosimetric measruements. After that, dosimetric properties of the EPID like linearity, fieldsize dependence on source to dedector distance (SDD), ghosting and depth dose curves were measured. Then the EPID was dismounted and computerized tomography (CT) images of the device were produced. Based on these images a set of test patterns were planned in Varian Eclipse and compared to the measured dose distributions with the gamma evaluation method.

Finally the plans of all six patients, treated at the Landesklinikum Wiener Neustadt with IMRT, were successfully verified with the EPID.

Zusammenfassung

Intensitätsmodulierte Strahlentherapie (IMRT) gehört zu den fortschrittlichsten Techniken, die heute im Bereich der Teletherapie existieren. Die Technik ermöglicht es die im Körper platzierte Dosis in drei Dimensionen an die Form des Tumors anzupassen. So kann im Vergleich zu konventioneller und konformaler Strahlentherapie im Tumor eine höhere Dosis platziert werden, während umliegendes, gesundes Gewebe besser geschont werden kann.

Da IMRT Felder sehr komplex sein können, werden im Verfikationsprozess hohe Anforderungen an räumliche Auflösung des Messgeräts gestellt. Mit einem, auf amorphen Silizium basierenden, Electronic Portal Imaging device (EPID), wie dem Varian aS1000, können die komplexen Dosisverteilungen die bei der Planung von IMRT Plänen entstehen, in Echtzeit mit Hilfe eines Computerprogramms aufgenommen werden.

Ziel dieser Diplomarbeit war es, ein Varian aS1000 im Landesklinikum Wiener Neustadt zur Verifikation von IMRT Plänen in den Arbeitsablauf zu integrieren. Dazu musste das Gerät für Absolutdosismessungen kalibriert werden um danach verschiedene dosimetrische Eigenschaften, wie die Linearität, die Abhängigkeit der Feldgröße vom Fokus-Detektor-Abstand (SDD), Ghosting und Tiefendosiskurven messen zu können. Dann wurde das Gerät abmontiert und Schnittbilder in einem Computertomographen (CT) angefertigt. Auf diesen CT Bildern basierend wurden eigens dafür entwickelte Testmatrizen geplant und ausgelesen, die dann mittels der Gamma Evaluation mit den gemessenen Dosisverteilungen verglichen wurden.

Letztendlich wurden die Pläne der sechs Patienten, die bisher am LK Wiener Neustadt mittels IMRT bestrahlt wurden, mit dem EPID erfolgreich verifiziert.

List of Abbreviations

aSi or αSi	Amorphous Silicon
CFRT	Conformal Radiation Therapy
CT	Computerized Tomography
CU	Calibrated Units
dMLC	dynamic Multi Leaf Collimator
DTA	Distance-To-Agreement
E_G	Energy Gap
EPID	Electronic Portal Imaging Device
H&N	Head & Neck
IDU	Image Detection Unit
ICRU	International Commission on Radiation Units and Measurements
IMB	Intensity Modulated Beam
IMRT	Intensity Modulated Radiation Therapy
LET	Linear Energy Transfer
LINAC	Linear Accelerator
MLC	Multi Leaf Collimator
MRI	Magnetic Resonance Imaging
MU	Monitor Unit
OAR	Organ At Risk
OER	Oxygen Enhancement Ratio
PET	Positron Emission Tomography
RBE	Relative Biological Efficiency
SDD	Source to Detector Distance
SSD	Source to Surface Distance

TFT   Thin Film Transistor

PD   Portal Dose

QA   Quality Assurance

RW3   Goettingen White Water

Introduction

The first patient cured by radiation therapy was reported in 1899, four years after Wilhelm Conrad Roentgen discovered the x-rays. Back in those days until now the main goal of radiation therapy has been to deposit dose in malignant cells and to spare healthy tissue. Over the years the peak energies of the x-ray tubes have been increased to increase depth of penetration. In consequence of that development, particle accelerators were introduced in the 1940's and betatrons became available for megavoltage x-ray treatment. The introduction of computers in the 1960's had a revolutionary impact on the fields of cancer therapy and diagnosis. Nowadays very powerful diagnostic methods like computerized tomography (CT), positron emission tomography (PET) and magnetic resonance imaging (MRI) are available and provide very exact information of size, location and type of tumours.

These exact diagnostic devices have initiated the development of more accurate radiation treatment methods like conformal radiation therapy (CFRT) and finally intensity modulated radiation therapy (IMRT), where the dose distribution in the tumour area can be adapted to the three dimensional shape of the tumour. The dose deposited in healthy tissue is kept as low as possible.

One important necessity for exact dose deposition in the tumour is the correct positioning of the patient's body in the treatment beam. To assure that, electronical portal imaging devices (EPIDs) have been developed. The newest generation of EPIDs are pixel based detectors with a resolution of 1024 x 768 pixels. These devices can also be used in an integration mode for absolute dosimetry with high resolutions and are therefore appropriate to verify the complex dose patterns in the fields of an IMRT treatment plan.

The goal of this work was to adapt a VARIAN aS1000 EPID, which had already been in use for imaging at the Landesklinikum (LK) Wiener Neustadt, but not for absolute dosimetric measurements. Therefore the EPID has to be calibrated properly, the image acquisition software has to be understood, the dosimetric properties of the EPID have to be measured and the achieved images have to be evaluated.

The final task was, to evaluate real patients' IMRT treatment plans and compare the measured dose distributions to matrices, which were produced by the VARIAN Eclipse planning software.

All measurements in this work were taken with photon beams emitted by a VARIAN CLINAC 2300 C/D at photon energies of 6 MV and 15 MV.

Theory

1   The Physics of Radiation Therapy

1.1   Interaction of photon beams with matter

If a photon beam (x- or γ-ray) impinges on a medium, the photons may be

- transmitted through without any interaction,
- scattered in different directions by one or more interactions
- or absorbed by transfer of its energy through one or more interactions. [7]

The electrons transfer their energy by producing ionization and excitation along their path through the medium. In case of living cells there is a chance of deposing enough energy inside the cell to destroy their reproducing capability. In fact most of the absorbed energy is converted to heat, producing no biologic effect. [8]

Photons that pass a medium without interaction are referred to as primary radiation, while photons that undergo interactions in the matter are named secondary radiation. If photons are scattered or absorbed, the beam has undergone attenuation. [8] Attenuation is caused by five major types of interactions. The coherent scattering, photoelectric effect, Compton effect and pair building are dominant at most therapeutic photon energies. Photo disintegration is a reaction between photon and nucleus and is therefore only relevant at high photon energies above 10 MeV. [7]

The probabilities of these five different mechanisms of interactions can be described as

$$e^{-\mu * x} = e^{-\varpi * x} e^{-\tau * x} e^{-\sigma * x} e^{-\kappa * x} e^{-\pi * x} = e^{-(\varpi + \tau + \sigma + \kappa + \pi) x}$$

Where $e^{-\mu x}$ is the probability that a photon passes a medium of thickness x without interaction and $e^{-\omega x}$… $e^{-\pi x}$ are the probabilities to not interact by a specific interaction. [7]

The linear attenuation coefficient μ is the sum of individual coefficients for coherent scattering (ω), photoelectric effect (τ), Compton effect (σ), pair production (κ) and photo disintegration (π). Therefore the differential equation for attenuation can be written as

$$I(x) = I_0 e^{-\mu^* x} = I_0 e^{-(\varpi + \tau + \sigma + \kappa + \pi)x}$$

where I(x) is the transmitted intensity, x is the thickness of the medium and I_0 is the intensity incident on the medium. [7]

A more fundamental coefficient is the mass attenuation coefficient where μ is divided by the mass density ρ. The mass attenuation coefficient is therefore independent of density ρ. [8]

$$\mu_m = \frac{\mu}{\rho}$$

All five effects have more or less relevance depending on the incident photon energy.
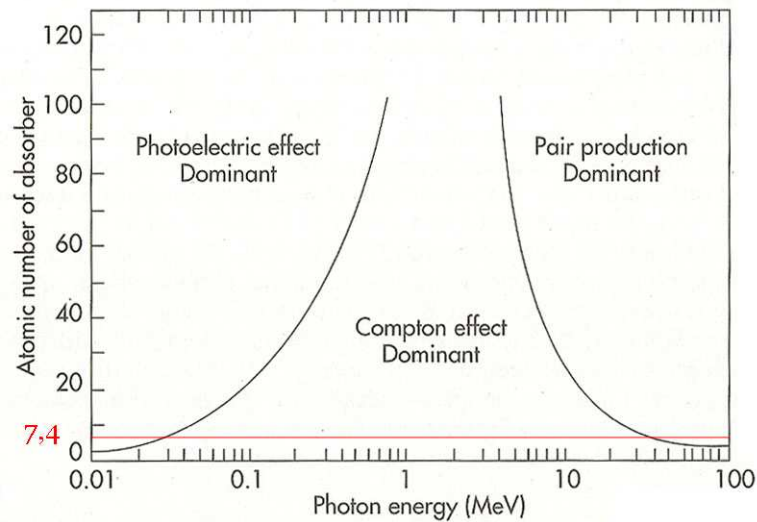

FIG. 1,   Occurrence of specific interactions depending on photon energy [8]

The plot shows that in an energy range between 1 MeV and 25 MeV, which is typical for a medical Linear Accelerator, Compton effect and pair production are the dominant interactions. But the red line marks Z_{eff}=7.4 which is the mean effective atomic number for muscles and water. This means that Compton effect is the major type of interaction in the body. [8]

1.1.1   Coherent scattering

Coherent or classical scattering, also known as Rayleigh scattering, is an interaction which can be visualized by considering the wave nature of photons: An

electromagnetic wave passes near a bound electron of an atom's outer shell and sets it into oscillation. The electron then reradiates the energy immediately in a slightly different direction. So the scattered x-rays have the same energy as the incident ones and produce an effect that looks like elastic scattering of particles because no energy is absorbed in the medium, just the direction is changed by a small angle. Coherent scattering tends to occur in high atomic number materials at low photon energies. For relatively high energy photons in radiation therapy with low atomic number materials, like bones and tissue in the human body, coherent scattering is neglectable in most applications. [8], [7]
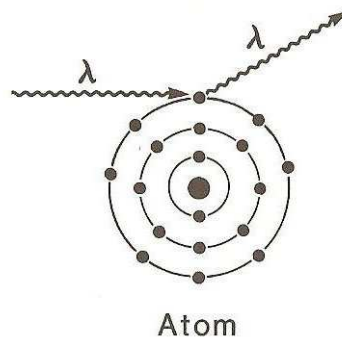

FIG. 2,   Coherent scattering [8]

1.1.2   Photoelectric effect

During photoelectric effect, a photon transfers its total energy to an inner shell electron of an atom and ejects it. This electron is called photoelectron and its kinetic energy is

$$E_{kin} = h\nu - E_b$$

where E_b is the binding energy of the electron. For low energy photons the electrons are mainly ejected at right angles. With increasing energies of the incident photon the electrons are ejected more and more in forward direction, meaning the direction of the incident photon. The vacancy produced by the ejection of the electron leaves the atom in an excited state. This hole can be filled by an electron of an outer shell accompanied with the emission of a photon with the energy corresponding to the energy difference between the outer shell electron and the inner shell electron. The energies of these photons are characteristic for each element. It is also possible, that

the characteristic photon ejects an outer shell electron, a so called Auger electron.
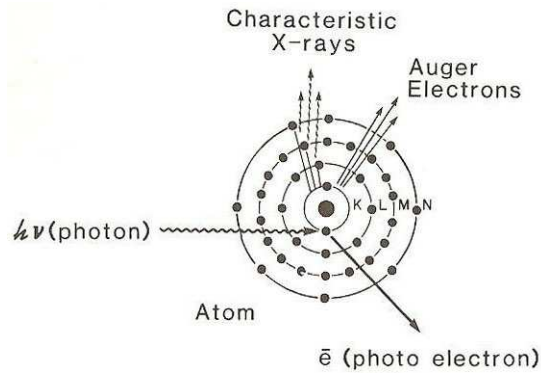

FIG. 3,   Photoelectric effect [8]

For low atomic number materials, like tissue, the emitted photons or Auger electrons have energies below 0.5 keV and are therefore absorbed in the immediate vicinity of the ejection site.

In general, the mass attenuation coefficient has a dependence on the atomic number Z of the absorbing material and the Energy E of the incident photon which is proportional to

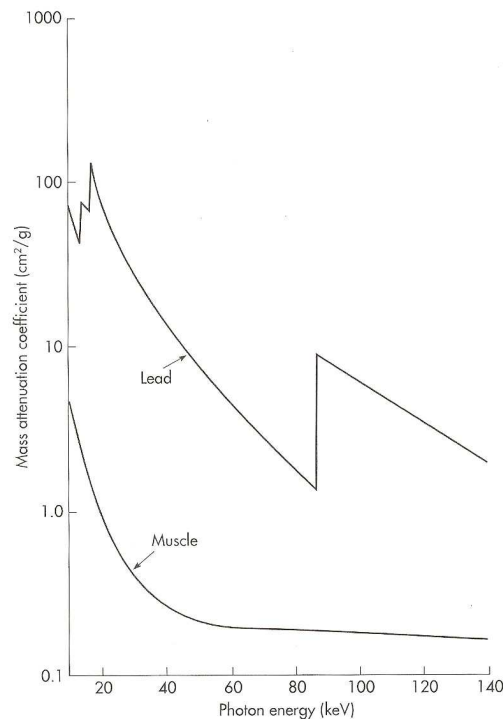$$\frac{\tau}{\rho} \propto \frac{Z^3}{E^3}$$

FIG. 4,   Mass attenuation coefficient for photons in muscle and lead [7]

Figure 4 shows the mass attenuation coefficient for lead and muscle. The graph for lead shows discontinuities at approximately 15 keV and 88 keV. These are called absorption edges for the L- and the K-electrons. Below 15 keV the photon's energy is not sufficient to eject an L-electron. When the photon has energy equal to the binding energy of an L-electron the probability of photoelectric absorption becomes suddenly higher. When the incident photon energy exceeds 88 keV, the photon is able to eject an electron out of the k-shell. [8], [7]

1.1.3   Compton effect

Compton scattering is the typical type of interaction for photons in an energy range between 30 keV and 30 MeV in soft tissue, where the binding energies of the outer electrons are much smaller than the energies of the photons. The electrons are therefore considered "free". During this process the photon interacts with the "free" electron and transfers part of its energy to the electron. The electron is emitted at an angle Θ and is called Compton electron, while the photon, with reduced energy, is scattered at an angle Φ.
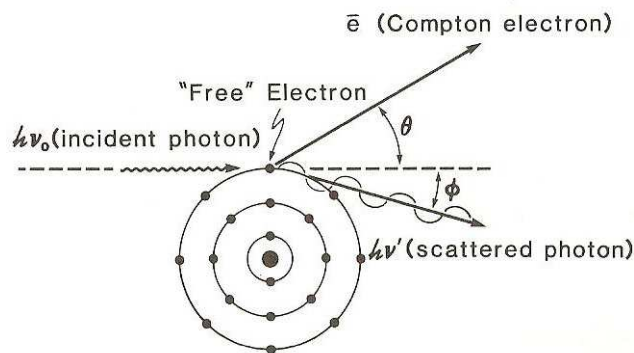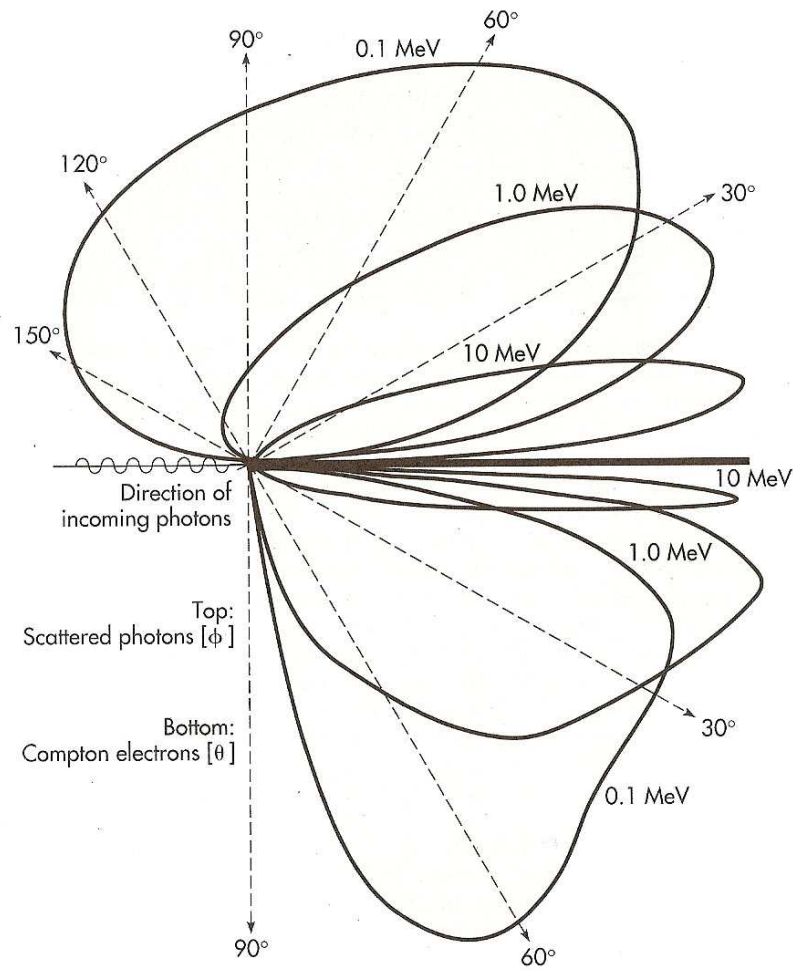

FIG. 5,   Compton effect [8]

FIG. 6,   Electron and photon scattering angles as functions of the energy of the incident photon [7]

Fig. 6 shows the dependence of the scattering angles of the photon and the electron on the energy of the incident photon. The scattering angle of the electron is confined to forward direction up to $\Theta = \pm 90°$. The photon's scattering angle can become backward directed up to $\Phi = 180°$ at low energies. Both angles Θ and Φ decrease with increasing energy of incoming photons. [8], [7]

1.1.4   Pair production

As predicted by Einstein's equation

$$E = mc^2$$

energy can be converted to mass. Since electrons have a rest energy of 511 keV, a photon with its energy above the threshold energy of 1.022 keV can produce a pair of an electron and a positron in the electromagnetic field of a nucleus. The photon

energy excess of this threshold energy is given to the electron and positron as kinetic energy. Above the threshold energy the probability of pair production increases with the logarithm of the incident photon energy. For photons up to about 20 MeV there is nearly no dependence on the atomic number Z, but above 20 MeV the higher atomic number materials show a lower attenuation coefficient compared to the low atomic number materials because of the screening of the nuclear charge by the orbital electrons. [8], [7]
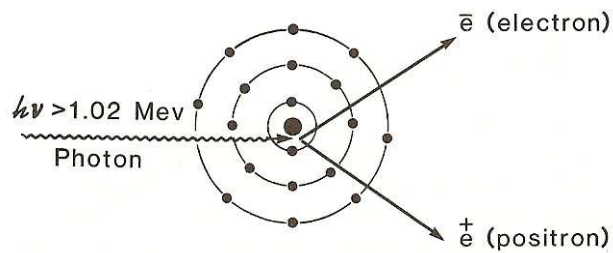
FIG. 7,   Pair production [7]

1.2   Biological effects on malignant cells

Biological effects on cells are caused either by primary radiation or by secondary radiation. Primary radiation are incident photons with enough energy to ionize atoms in tissue. If the electrons, produced during ionization, have enough energy to again ionize atoms, cascades of electrons are produced, which are referred to as secondary radiation. [33]

1.2.1   Linear Energy Transfer

Radiation Quality can be characterised by the Linear Energy Transfer (LET)

$$LET = \frac{dE}{dl}$$

which is the rate of energy loss E by unit path length l in collisions in which energy is locally absorbed. [8] The values of LET are usually given in keV / µm.

TAB. 1,   *LET values for different beam types [33]*

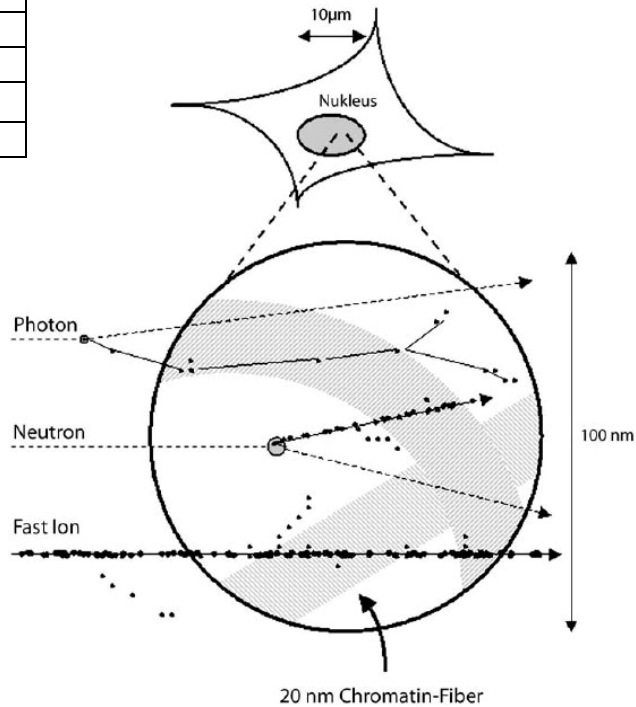|	LET [keV / µm]
250 kV photons	0.2
1,25 MeV photons	2
2 MeV protons	17
10 MeV ^{12}C ions	150
2,5 MeV α particles	170

FIG. 8,   *Different spatial patterns of energy transfer for different types of ionizing radiation [33]*

In the illustration the black dots represent ionization processes in the Chromatin-fiber. It can be seen that the density of ionization processes is much less for photons than for high LET particles.

The positive effect concerning radiation therapy is, that dose can be deposited more homogenously in a larger area.

1.2.2   Relative Biological Effectiveness

Typically particles with higher LET values also show a higher biological effectiveness. To quantify this effect, a coefficient called Relative Biological Effectiveness (RBE) was introduced.

$$RBE = \frac{\text{Dose from Standard Radiation to produce a given biological effect}}{\text{Dose from Test Radiation to produce a given biological effect}}$$

It is common to use 250 keV photons or ^{60}Co-radiation as a standard. RBE depends

on LET, radiation dose, number of dose fractions, doserate and on the irradiated biological system. [33]
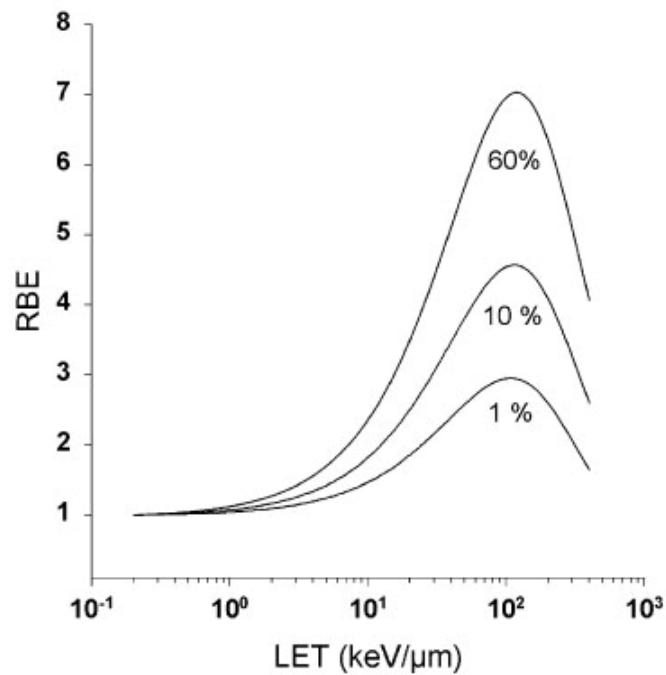

FIG. 9,   Dependence of RBE on density of ionization processes [33]

Different experimental setups for different biological systems showed the maximum RBE at approximately 100 keV / µm.

Simplified calculations show that the average distance between two ionizations in the cell at these LETs is approximately 2 nm, which is approximately the diameter of a DNA-doublehelix. [33]
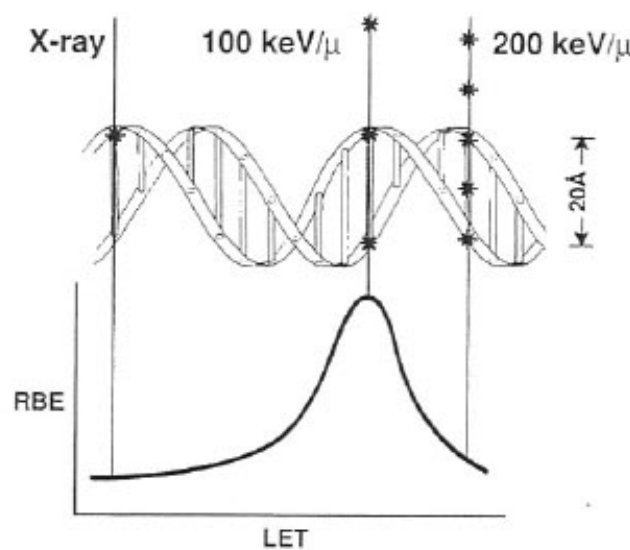

FIG. 10,   Illustration of the "over-kill" effect [11]

This illustration demonstrates why the RBE does not increase more after reaching the maximum value at approximately 100 keV / µm. Radiation of this quality most likely produces double strand breaks in the DNA double helix. [11]
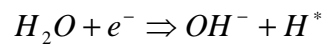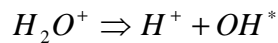
1.2.3   Indirect action cell damage

Direct action cell damage occurs, when the radiation directly interacts with the critical target in the cell. But this is a dominant process for high LET particles. Low LET particles produce mainly indirect action cell damage, where the particles interact indirectly with other molecules, mainly with water. The most important processes are [11]

<div align="center">

Ionization of water molecule:

$$H_2O + energy \Rightarrow H_2O^+ + e^-$$
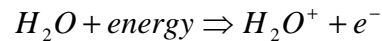
Ion radical forms free radical:

$$H_2O^+ \Rightarrow H^+ + OH^*$$

$$H_2O + e^- \Rightarrow OH^- + H^*$$

The hydroxyl radical then diffuses and attacks the DNA molecule
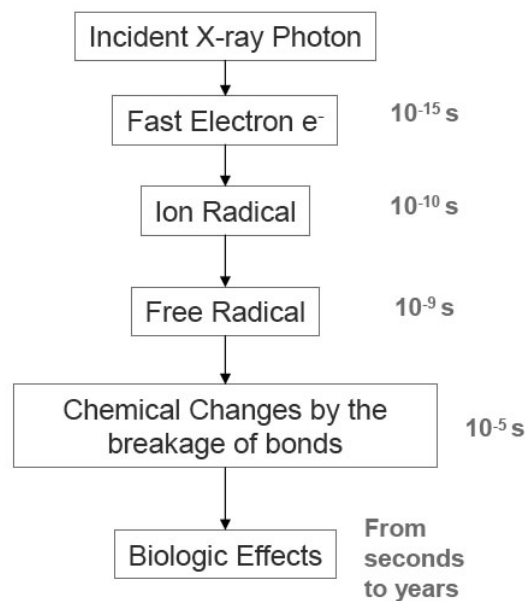
</div>

FIG. 11,   Timescale in indirect action cell damage [11]

1.2.4   The oxygen effect

The presence of molecular oxygen in tumours enhances the biological effect of radiation. Especially for low LET particles like photons it is crucial for a successful treatment to have a sufficient amount of O_2 in the tissue. To quantify the biological effect of O_2 in tissue the oxygen enhancement ratio (OER) is defined as [11]

$$OER = \frac{\text{Dose to produce a given effect without molecular oxygen}}{\text{Dose to produce a given effect with molecular oxygen}}$$

The highly reactive radicals, produced by the ionizing radiation, are fixated by the molecular oxygen while absence of oxygen restitutes the radicals. [1]

1.3   Teletherapy

1.3.1   Materials and Methods

1.3.1.1   Linear Accelerator

Linear Accelerators are devices that accelerate charged particles such as electrons to high energies in a linear tube by using high-frequency modulated electromagnetic fields. In clinical linacs it is common to use the electron beam itself to treat tumours or to strike a suitable target in order to produce photons. [8]
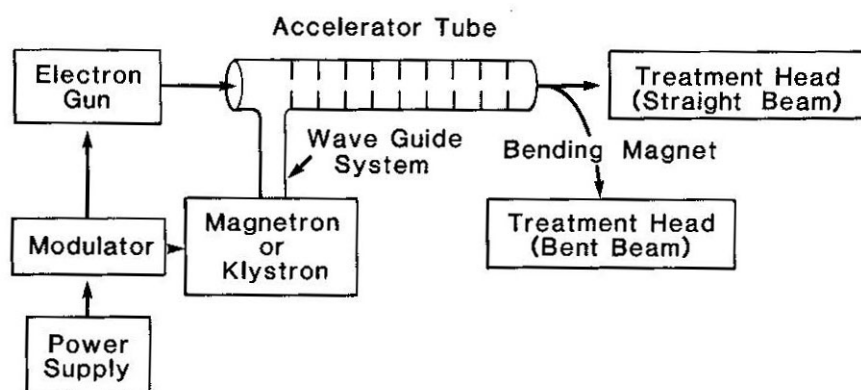

FIG. 12,   Block diagram of a typical medical linac [8]

Fig. 12 shows the block diagram of a typical medical linac, where the power supply provides DC power to the modulator, which includes a pulse-forming network to produce microsecond DC pulses. These high voltage pulses are delivered

simultaneously to the Electron Gun and the Magnetron or Klystron unit. This unit produces the microwaves which are transmitted to the Accelerator Tube via a Wave Guide System. The electron gun produces electrons synchronously to the produced microwaves and accelerates them towards the evacuated Accelerator Tube. [8]

1.3.1.1.1 Electron gun

The beam injection unit is basically an electrostatic accelerator with a heated cathode. The electrons are emitted thermoionically and subsequently focused by curved electrodes and accelerated toward a perforated anode. After passing the anode, the electrons enter the accelerator tube. [31]
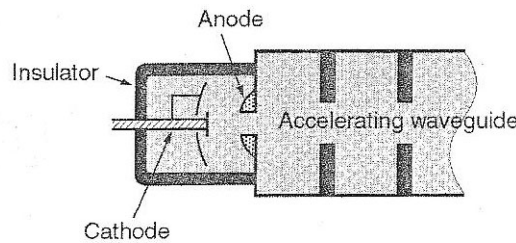
FIG. 13,   Schematic diagram of a simple electron gun [31]

1.3.1.1.2 Accelerator tube

Accelerator tubes or accelerating waveguides are evacuated metallic structures with mostly circular cross sections. The propagation of microwaves in these cylindrical structures is determinated by Maxwell's Equations. The boundary conditions at the metallic walls are that the tangential component of the electric field and the normal component of the magnetic field are zero. Most circular accelerating wave guides are energized in TM_{01} mode, where the magnetic field is transverse to the longitudinal axis of the waveguide and the electric field is axial. In order to accelerate electrons it is necessary to slow down the phase velocity of the microwaves. The phase velocity defines the velocity of the electric field pattern. Decreasing the phase velocity below the speed of light enables the electron to follow the electric field pattern. This can be done by adding a series of irises. The distance between the irises in the iris-loaded waveguide is given by the velocity of the particles [8], [7]:

$$L_n = \frac{v_n}{2f}$$

Where L_n is the distance between adjacent discs, v_n is the velocity of the particles and f is the frequency of the microwaves. If the microwaves are absorbed and not reflected at the end of the waveguide it is called moving wave accelerating waveguide.
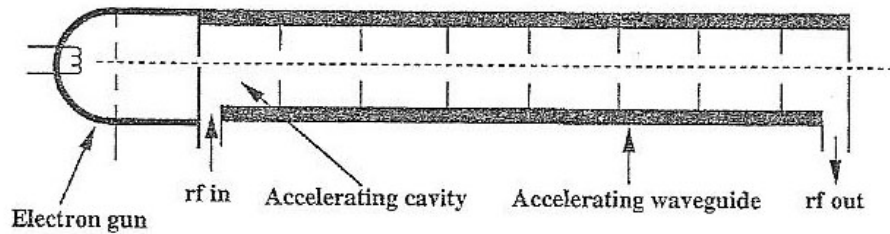

FIG. 14,   Schematic diagram of a travelling wave accelerating waveguide [31]

If the wave is reflected at the end of the waveguide the structure is called standing wave accelerating waveguide. In this structure the forward moving wave and the reflected wave interfere alternating constructively and destructively in adjacent cavities. Therefore the field size in every second cavity is doubled and zero everywhere else. By moving the cavities without field to the side, off waveguide axis, the waveguide can be shortened by effectively 50 % as shown in Fig. 15
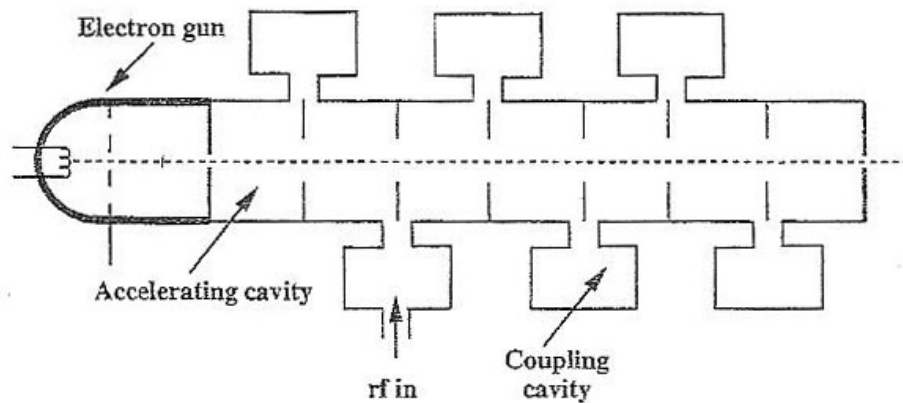
FIG. 15,   Schematic diagram of a standing wave accelerating waveguide [31]

1.3.1.1.3 Bending magnets

Since in most electron-linacs which are used for cancer therapy the accelerator tube is parallel to the floor, it is necessary to bend the electron beam by at least 90° to hit the isocentre of the machine. It is practical to bend the beam more than just 90° to produce an additional energy focusing effect. Bending magnets are designed to have the magnetic field perpendicular to the path of the electrons. Therefore Lorentz force

becomes:

$$\vec{F} = q\,\vec{v}\,\vec{B}$$

where $\vec{F}$ is the force on the particle, q is the elementary charge, $\vec{v}$ is the velocity of the electron and $\vec{B}$ is the magnetic field. By substituting the expression for the centripetal force

$$\vec{f}_c = \frac{m\,\vec{v}^2}{\vec{r}}$$

where $\vec{f}_c$ is the centripetal force, m is the mass of the electron, $\vec{v}$ is the velocity and $\vec{r}$ is the radius of the bend and by rearranging the variables one gets

$$\vec{r} = \frac{m\,\vec{v}}{q\,\vec{B}}$$

The radius is directly proportional to the velocity of the particle. This effect leads to a divergence in beam and a bigger spotsize on the target but on the other hand it can be used to remove off-energy particles with apertures inside the magnet.
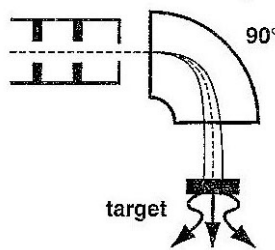
FIG. 16,   Electron beam bending by 90°[31]

Fig. 16 shows a simple 90° bending magnet and the p aths of three electrons with different energies. The electron with the highest energy takes the longest path. This increases the spot size on the target.
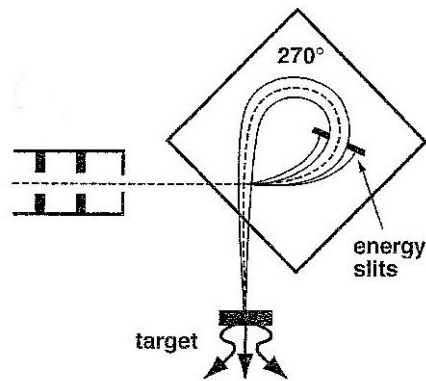
FIG. 17,   Electron beam bending by 270°[31]

The 270° system is achromatic and provides electron s with a long exposure to the magnetic field. The electrons are refocused again and thus the system has a small focal spot size on the target. Additionally the system is equipped with energy apertures which remove electrons that are not within ±5 % of the nominal energy. A clear disadvantage of this layout is that the system is bulky and needs a lot of space and therefore the lowest possible isocentre moves up.
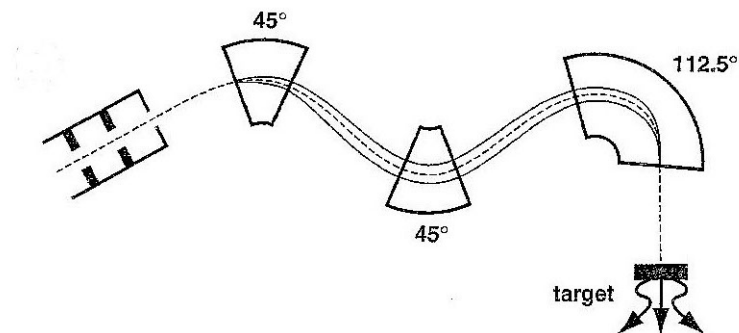

FIG. 18,   Electron beam bending by 202.5°[31]

The 202.5° system offers the advantages of both the 90° and the 270° system. It is achromatic and the required vertical space is less than for the 270° system.

1.3.1.2   Treatment head

The treatment head consists of a shell of high-density shielding material like lead or tungsten to shield leakage radiation. [8]
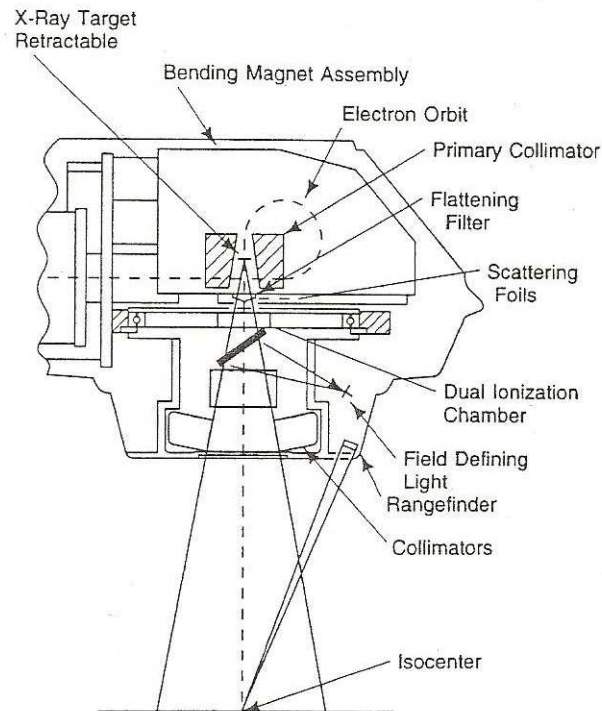
FIG. 19,   *Treatment head with its main components [31]*

The head includes several retractable x-ray targets, beam flattening filter and electron scattering foils, primary and adjustable secondary collimators, ionization chamber, a field defining light, a rangefinder and optionally a Multi Leaf Collimator (MLC). [31]

1.3.1.2.1   X-ray target and flattening filter

In contrast to diagnostically used x-ray tubes, the targets in medical linacs are mostly transmission targets. [7] In Fig. 20 it can be seen that at therapeutical energies the angular distribution of the produced photons is mostly forward directed.
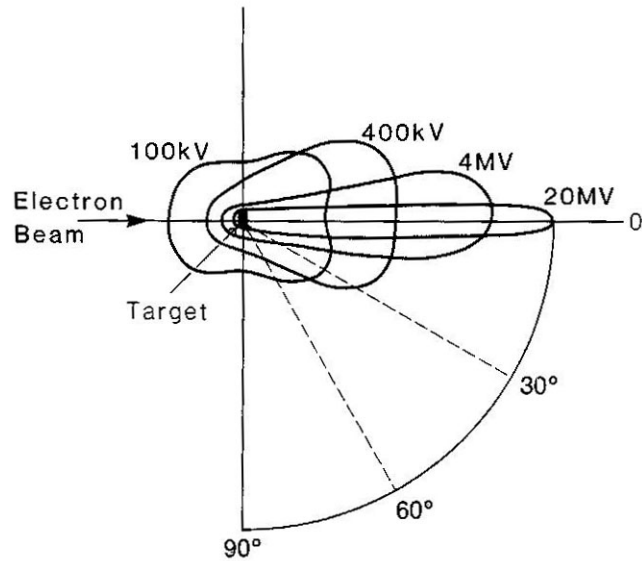
FIG. 20,   Schematic illustration of spatial distribution of x-rays around a target [8]

Since the x-ray yield is in first approximation (within an angle of ±15°, which corresponds to an 40 x 40 cm^2 field at an SSD of 100 cm) independent of the target, materials with diverse atomic numbers like Pb, Al, or Cu are used. [7] Fig. 21 shows the relative x-ray yield over distances from the central axis measured at a depth of 10 cm in a Lucite phantom at a SSD of 100 cm.
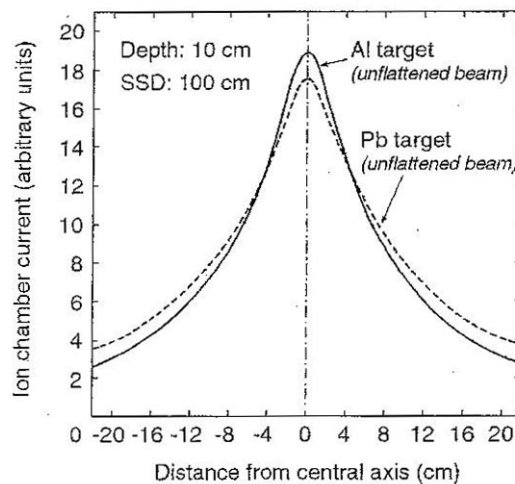
FIG. 21,   Relative x-ray yield against distance from central axis [7]

Specially designed filters flatten the beam, because for clinical use the beam profile scan in the central 80 % (±16 cm of the central axis at an SSD of 100 cm) must not deviate more than ±3 % from the central axis value. For electron beams these filters can be mechanically retracted from the beam.

1.3.1.2.2   Monitor ionization chamber

To make sure that exactly the planned dose irradiates the patient nowadays two monitor ionization chambers of transmission type are inserted into the beam line. The two chambers work completely independently to backup each other in case of a failure. These chambers should have a minimal effect on the radiation beam. In principle a low atomic number material would provide minimal perturbation of the beam but at the expense of chamber wall rigidity and stability. However it is also important that the chamber is not leaking, because the measurements should be independent of the ambient temperature and pressure and the geometry. Especially the distance between the electrodes should not change because of thermal fluctuations. Therefore a compromise between low atomic number material and rigidity and stability has to be found. To make sure that the ionization chambers work at a collection efficiency of well above 99 %, the biasing potential should be high enough to operate the chamber under saturation conditions. The dose measured by the ionisation chambers is given in Monitor Units (MUs). Typically the chambers are calibrated to measure 1 MU if a dose of 1 cGy is deposited in a 10 x 10 cm^2 field in the centre beam at a SSD of 100 cm in dose maximum depth of a water phantom. [31]

1.3.1.2.3   Mulit Leaf Collimator

Multi leaf collimators (MLCs) are specially designed collimators which consist of leafs that can be moved independently to collimate the beam according to the shape of the tumour. This technique replaces the very time consuming act of building field blocks for shielding vital organs or healthy tissue.
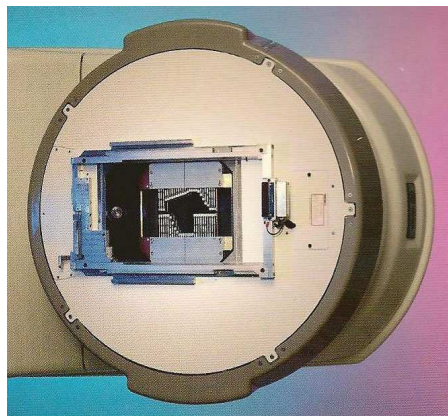

FIG. 22,   View from isocentre towards treatment head with installed MLC. Courtesy of Varian

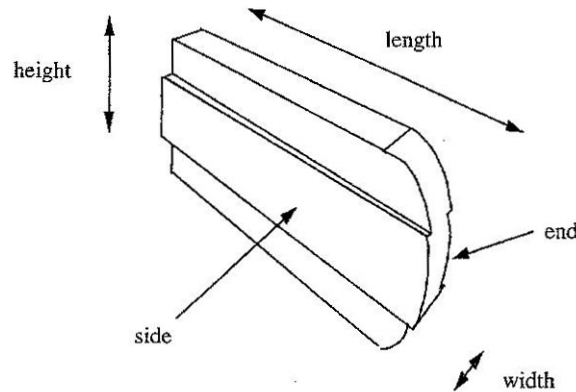*Ass. (Paolo Alto, CA)*

FIG. 23,   *Example of a single leaf of a MLC*

The challenge in designing a MLC comes from the fact that at larger field sizes photons hit the leafs at different angles than the ones close to the centre beam. A possible solution for this problem would be to adjust the alignment of the leafs (shown in Fig. 24), another one would be to move the leafs at a path along the circumference of a circle with its centre located in the x-ray target. Also the ends of the leaf show a curved shape to meet this criterion.
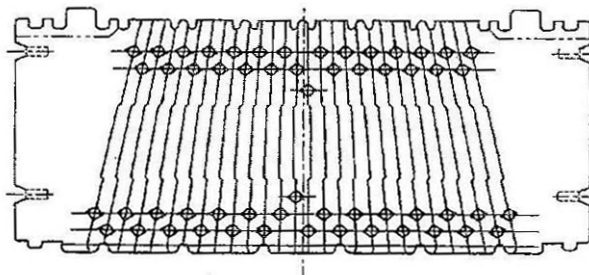

FIG. 24,   *MLC leaf bank with leaf alignment adapted to the divergence of the beam*

Fig. 23 and Fig. 24 show a technique to prevent interleave leakage between the sides of two adjacent leafes called tongue and groove [31]

1.3.1.3   Electronic Portal Imaging Device

International Commission on Radiation Units and Measurements (ICRU) recommend an accuracy of ± 5 % in dose delivery. One problem in reaching that goal is caused by geometric discrepancies due to patient positioning. EPID devices, built for monitoring the correct position of the patient, should prevent these deviations. Different technologies are available like films, arrays of liquid ionization chambers or arrays of photodiodes. [31]

1.3.1.4   Intensity modulated radiation therapy

1.3.1.4.1   Three evolutions of radiation Therapy

A technically simple method is called conventional radiation therapy, where rectangular fields are collimated to irradiate the whole volume of the tumour. This technique reaches its limits if organs at risk (OARs) are located near the tumour. A better technique to avoid irradiation of healthy tissue and OARs is called conformal radiotherapy (CFRT), where the field shape is adapted to the shape of the tumour either by custom made blocks or by MLC.

While in CFRT homogenous fields are distributed, the fields in intensity modulated radiation therapy (IMRT) are inhomogeneous and show a fluence pattern. By that, the dose distribution can be adapted to distribute lower dose in areas where OARs are in the field region. These lower dose sections can be compensated with fields coming from other angles. The goal is to distribute a homogenous dose inside the tumour and keep the dose in healthy tissue as low as possible. This can be achieved by using a large number of fields, which, on the other hand, makes the treatment planning very time consuming. Therefore a tradeoff has to be found between a good dose distribution and a reasonable fast planning procedure. [35]
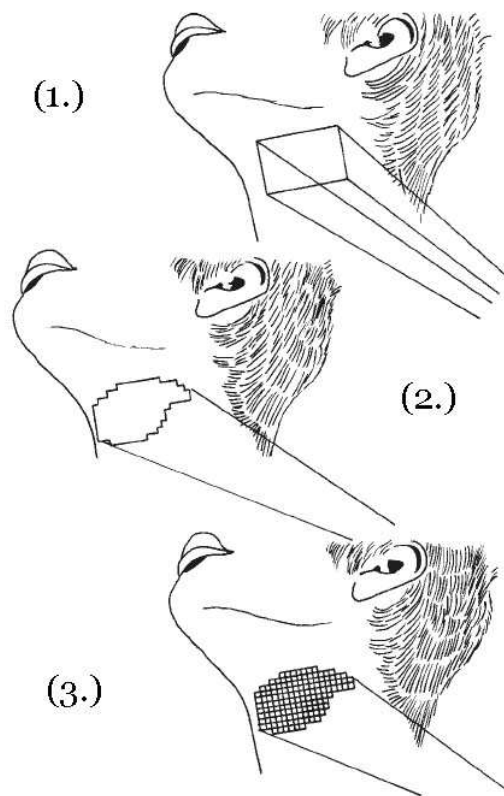
FIG. 25,   (1.) Conventional Radiation therapy - (2.) CFRT - (3.) IMRT [35]

1.3.1.4.2   Methods of IMRT

There are different techniques to create fluence patterns inside the field as

- IMRT with compensators,

- IMRT with MLC and step-and-shoot-technique,

- IMRT with dynamic MLC.

1.3.1.4.2.1 IMRT with compensators

The intensity of the photon beam can be varied by change in thickness of a compensator located in the beam. For every field an absorber profile has to be calculated which is inverse to the desired fluence map. These compensators have to be built for every planned field manually, which is a high effort. Advantages of this technique are that a high spatial distribution can be achieved with relatively low chosen monitor units. [33]
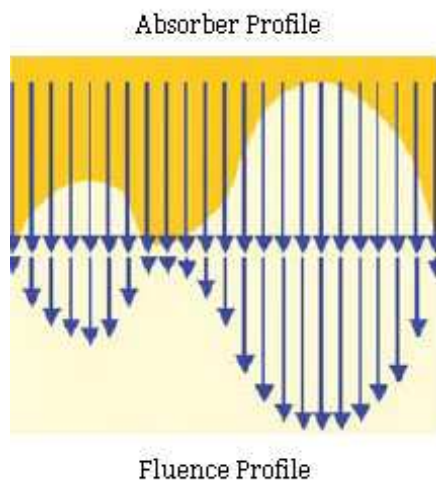
FIG. 26,   The principle of a compensator located in the beam [33]

1.3.1.4.2.2 IMRT with MLC and step-and-shoot-technique

With the step-and-shoot-technique different static MLC positions are superposed at each gantry angle to create a fluence pattern. The method is sequential, the beam is off when the MLC is moving and gets switched on when the MLC has reached the desired position.
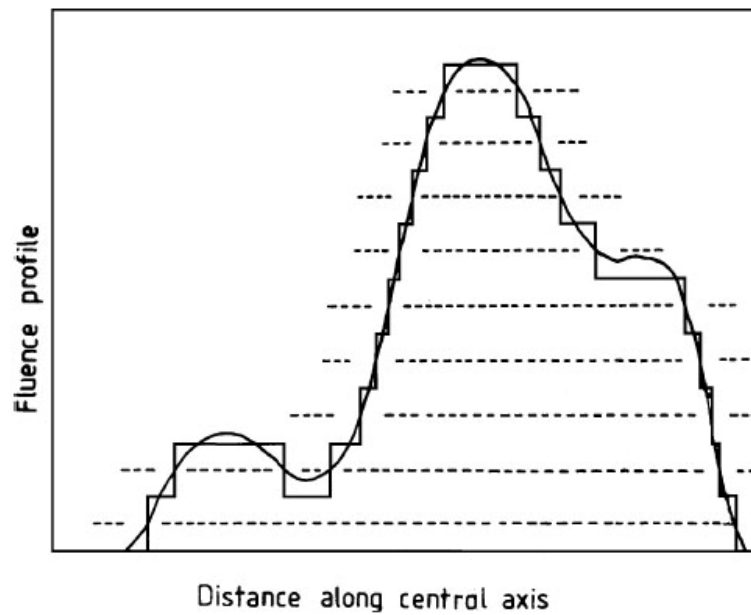
FIG. 27,   Example for a possible 1-D dose distribution [2]

Fig. 27 shows a one dimensional dose distribution which could be part of the fluence matrix for one specific gantry angle. The solid line shows a continuous fluence function while the square cut solid line marks the leaf edge positions on the left and the right side as a result of inverse planning.
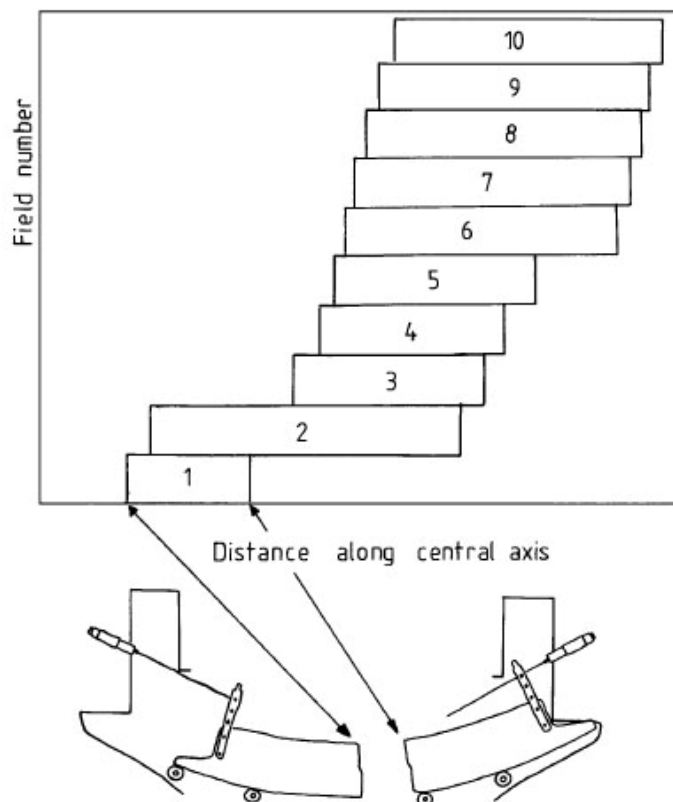
FIG. 28,   A possible combination of fields to achieve the desired dose distribution [2]

Fig. 28 shows one possible set of fields (in "leaf sweep" technique) which superpose to a fluence distribution shown in Fig. 27. Each rectangle symbolizes one field where the left vertical line is the right leaf edge of the leaf positioned left and the right vertical line is the left leaf edge of the leaf positioned right of the field. The method of setting the leafs shown here is known as "leaf sweep". [2]
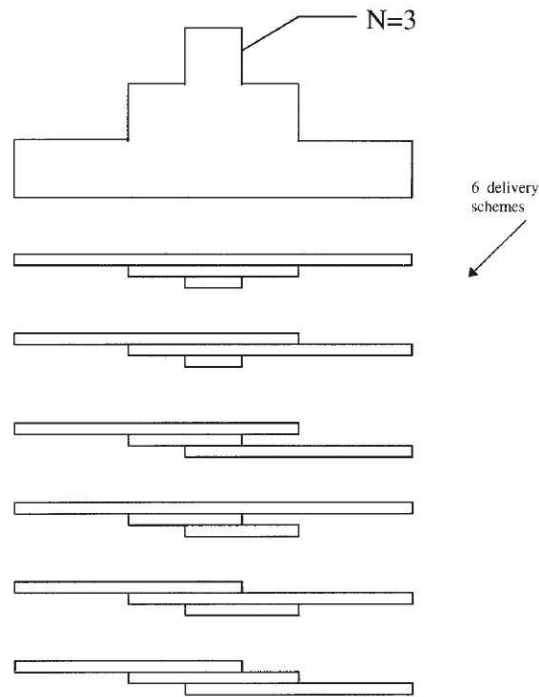
FIG. 29,   Different methods to acquire one specific fluence pattern in step-and-shoot technology

Fig. 29 shows a dose distribution with a single peak and 3 different dose levels on top of the scheme. There are 3! = 6 methods to create a fluence map like this with three static MLC segments. The uppermost combination is called "close in" while the lowermost is known as "leaf sweep". [35]

1.3.1.4.2.3 IMRT with dynamic MLC

IMRT with a dynamic multi leaf collimator (dMLC), also called sliding window IMRT, is a technique where each leaf pair moves a "window of beam" over the field. During planning procedure the computer calculates the speed of each leaf and by varying opening times at different areas and by changing the size of the window a fluence distribution can be created.
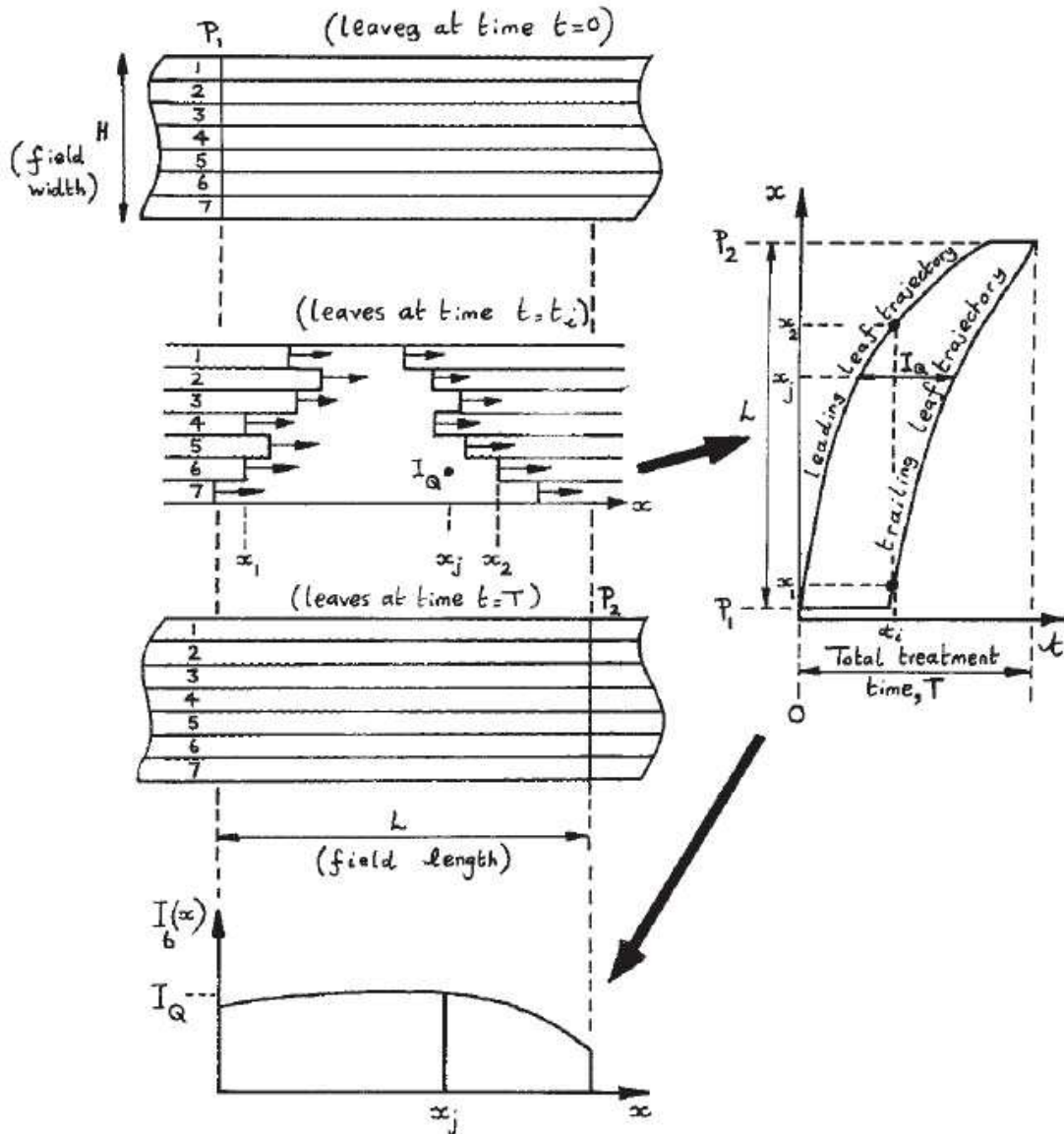
FIG. 30,   Illustration of the dMLC concept delivering IMRT [35]

Fig. 30 shows an example of a seven leaf MLC with leafs labelled from 1 to 7. In the uppermost figure all leaves are parked in the start position P_1 at the left side of the picture at time t = 0. All leafs move, each on its own trajectory, and at an arbitrary time t = t_i the leafs show a constellation like in the middle picture. The space between the leading leaf and the trailing leaf of each leaf pair gets irradiated while the other areas are shielded at the same time (ignoring scattering and interleaf leakage). When total treatment time is over at t = T all leafs have reached the final parking position at P_2 at the right hand side of the last picture, after trailing from P_1 to P_2 through distance L. On the right hand side of the illustration the trajectory diagram for the leading leaf and the trailing leaf of leaf pair number 6 is drawn. The x-axis represents the treatment time while the y-axis shows the travelled distance. In the trajectory

diagram the intensity I_q at any place $x = x_j$ is defined as the horizontal distance between the two leaf trajectories (again ignoring scattering and interleaf leakage). The trajectory diagram corresponds to the intensity modulated beam (IMB) in the lowest diagram of the illustration, where $I_6(x)$ is the actual intensity at a place $x = x_j$. [35]

The method with a dMLC needs a shorter time for dose application than the step-and-shoot technology, but the demands on the MLC are much higher, because not only the exact positions of the leafs but also their exact movements have to be assured. [33]
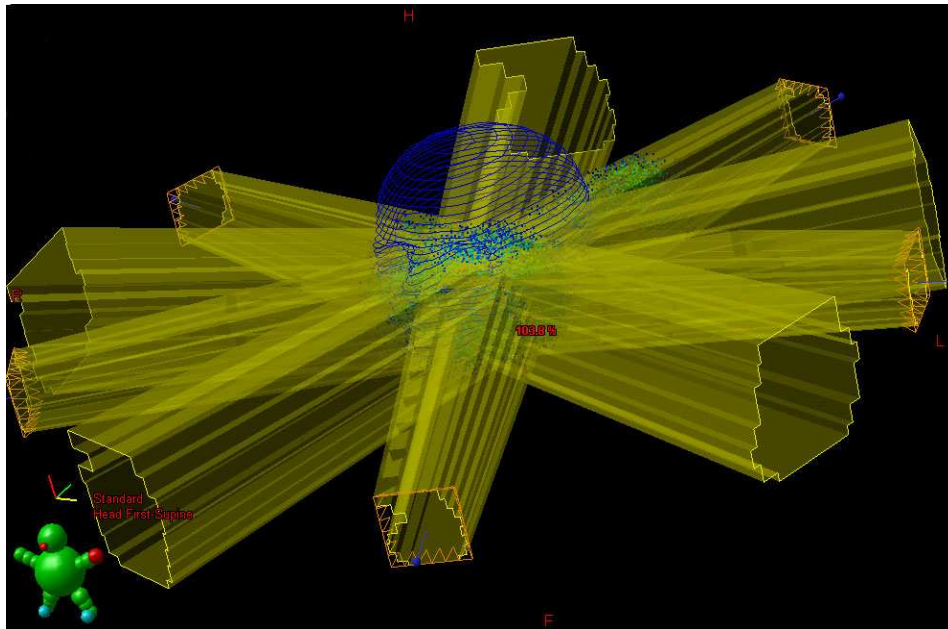
FIG. 31,   5 IMRT fields irradiating a sphenoid tumour, planned in Varian Eclipse

1.3.1.5   Comparison of dose distributions – gamma evaluation method

Gamma evaluation, proposed by Low et al. (1998), offers a method for quantitative comparison of different dose distributions. This quantitative method combines two criteria:

First the measurement of relative dose differences between corresponding pixels in the reference dose distribution (D_m) and the measured dose distribution (D_c). Corresponding pixels of the two images, which dose differences are smaller than a previously chosen value (ΔD_m) are said to be in agreement. This approach is good for areas with small dose gradients.

Secondly the distance-to-agreement (DTA) is studied. DTA is defined as the smallest

distance between a point in the measured image and the point in the reference image which has the same dose value. Of course the resolution of the dose images is limited. So the area between two pixels has to be interpolated. To be in agreement the distance has to be smaller than the chosen criterion (Δd_m). This approach is suitable for parts of the distribution where high dose gradients appear.

These two acceptance criteria combine to an ellipsoid in a space created by dose and spatial dimensions.
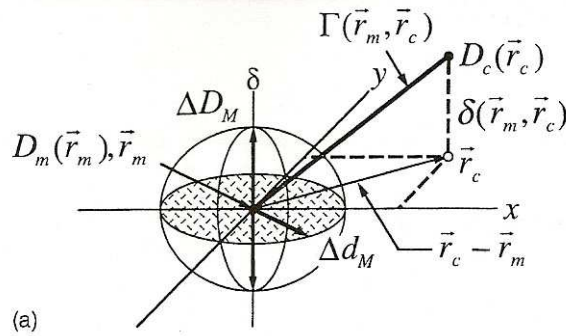
FIG. 32,   Schematic representation of the theoretical concept of the gamma evaluation method
[9]

The surface of the ellipsoid is given by

$$1 = \sqrt{\frac{r^2(r_m, r\ )}{\Delta d_M^2} + \frac{\delta^2(r_m, r\ )}{\Delta D_M^2}}$$

where

$$r(r_m, r) = |r - r_m|$$

and

$$\delta(r_m, r) = D(r) - D_m(r_m)$$

is the dose difference at the position r_m.

The right hand side of the ellipsoid's surface equation is used to define a quality index

$$\gamma(r_m) = \min\{\Gamma(r_{m,} r_c)\} \forall \{r_c\}$$

where

$$\Gamma(r_{m,r_c}) = \sqrt{\frac{r^2(r_m,r_c)}{\Delta d_M^2} + \frac{\delta^2(r_m,r_c)}{\Delta D_M^2}}$$

and $\quad r(r_m,r_c) = |r_c - r_m| \quad$ and $\quad \delta(r_m,r_c) = D_c(r_c) - D_m(r_m)$

This leads to the pass-fail criterion [9]

$\gamma(r_m) \leq 1$,   measured value passes

$\gamma(r_m) > 1$,   measured value fails

2   The physics of semiconductors

2.1   The principle of semiconductors

Semiconductors show an energy band structure like metals where the band gap between conduction band and valence band is below 4 eV. This means that thermal energy at room temperature is sufficient to excite electrons from the filled valence bands into the unfilled conduction bands just by thermal vibration. [5], [23]
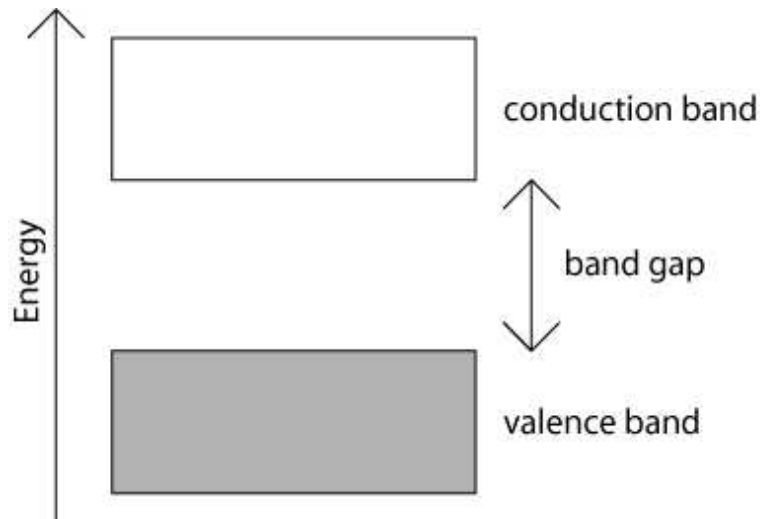
FIG. 33,   Energy bands [23]

Another possibility of defining a semiconductor is through free carrier concentration at room temperature.

TAB. 2,   Classification of solids according to their energy gap E_G and carrier density n at room temperature [5]

Type of solid	E_G (eV)	n (cm^{-3})
Metal	no energy gap	10^{22}
Semimetal	$E_G \leq 0$	$10^{17} - 10^{21}$
Semiconductor	$0 < E_G < 4$	$<10^{22}$
Insulator	$E_G \geq 4$	$<<1$

2.2   Charge Carriers in Semiconductors

If the energy gap is sufficiently small and the temperature is above absolute zero, electrons can be excited into the conduction band either by thermal excitation or by absorption of a photon, which is important for the principle of semiconducting detectors. This can be plotted schematically in an E-k-diagram, where E is the energy and k is the norm of the wave vector. The filled circles represent the electrons while the unfilled circles show empty states (holes).
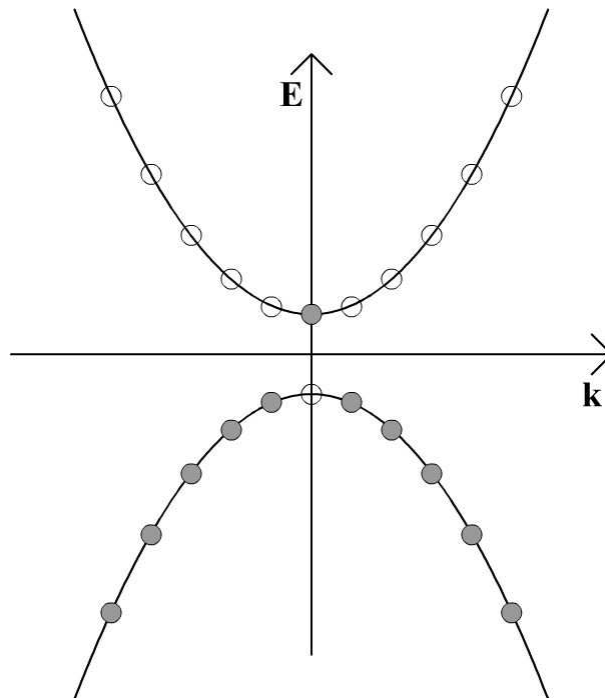
FIG. 34,   Schematic diagram of an electron-hole-pair [23]

If an electric field is applied to the semiconductor, all electrons in the solid feel the force but since no two electrons can fill the same state at the same time, only the

electrons that have an empty state adjacent to their actual state can gain momentum. [23]
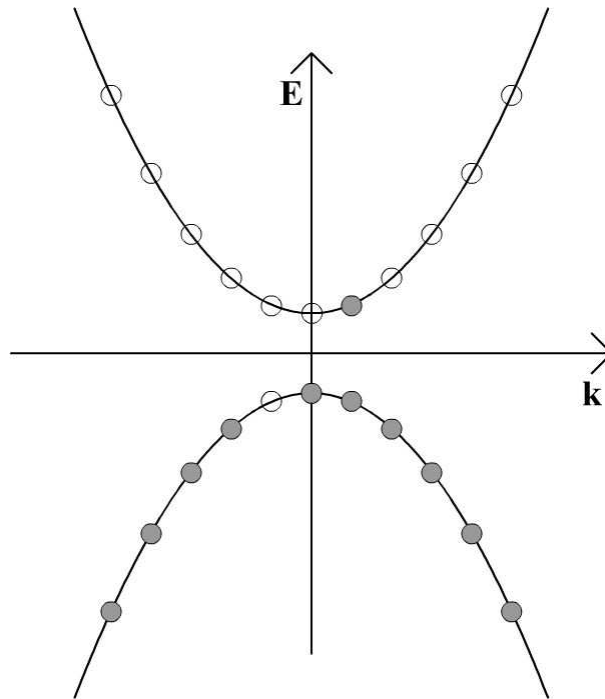
FIG. 35,   Movement of an electron-hole-pair [23]

The empty state can be viewed as a positive particle and therefore it moves in the opposite direction of the electron.

2.3   p-i-n Photodiodes

The intrinsic semiconductor (i-type) is a pure semiconductor without any significant dopant species present. Therefore the number of holes and excited electrons are equal.

If an i-type semiconductor is doped with donator atoms, the electron concentration can be increased at constant temperature and is then called n-type semiconductor. Analogous a p-type semiconductor can be produced by doping a pure semiconductor with acceptor atoms. In that case the number of holes is increased. [15]

If a p-type and a n-type semiconductor are brought together, electrons from the n-type semiconductor fill the holes of the p-type semiconductor near the boundary and a so called depletion zone is formed. If the n-type is connected to the positive terminal and the p-type to the negative terminal, the size of the depletion zone increases. This is called negative biasing and used for photodiodes, where the

photons produce an electron hole pair inside the depletion zone. There the electrons and the holes are separated by the electric field.

To be measured, photons must be absorbed in the depletion zone, therefore the sensitive area should be as large as possible. The size of the depletion zone can be increased by rising the applied voltage, but this method is limited.

By putting an i-type semiconductor between a n-type and a p-type semiconductor the size of the depletion zone (the sensitive area of a detector) can be increased without rising the negative biasing voltage. [23], [32]
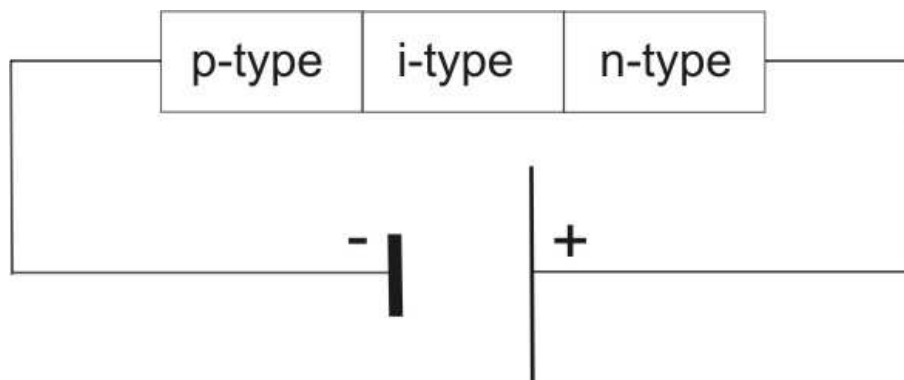
FIG. 36,   Reverse biased p-i-n photodiode

Materials and Methods

1   Hardware

1.1   Varian CLINAC 2300 C/D

The LINAC at the Landesklinikum in Wiener Neustadt, which was used for all measurements, is a CLINAC 2300 C/D, developed and produced by Varian Medical Systems, Palo Alto, CA. The machine was designed for dynamic conformal therapy with enhanced conventional therapy features.

FIG. 37,   *Photograph of a Varian CLINAC 2300C/D with extracted EPID*

The accelerator provides 2 different x-ray beam energies and 6 electron beam energies. Relevant x-ray beam energies and their specifications can be found in the table below. [24]

TAB. 3,   *X-ray beam energies of Varian CLINAC 2300 C/D [24]*

Nominal energy [MV]	d_{max} [cm]	% depth dose at 10 cm depth	Maximum dose rate [MU/min]	Flatness	Symmetry
6	1.5 ± 0.2	67.0 ± 1.0	600	± 3.0 %	2.0 %
15	3.0 ± 0.2	77.0 ± 1.0	600	± 3.0 %	2.0 %

Flatness is defined as the variation of x-ray intensity within 80 % of the field and is measured at a SSD of 100 cm in 10 cm of water for square fields. Symmetry is defined as the difference between the dose delivered at two different points which are equidistant and symmetrically distributed around the central beam axis and also within 80 % of the radial and transverse axis. This specification also applies to square fields.
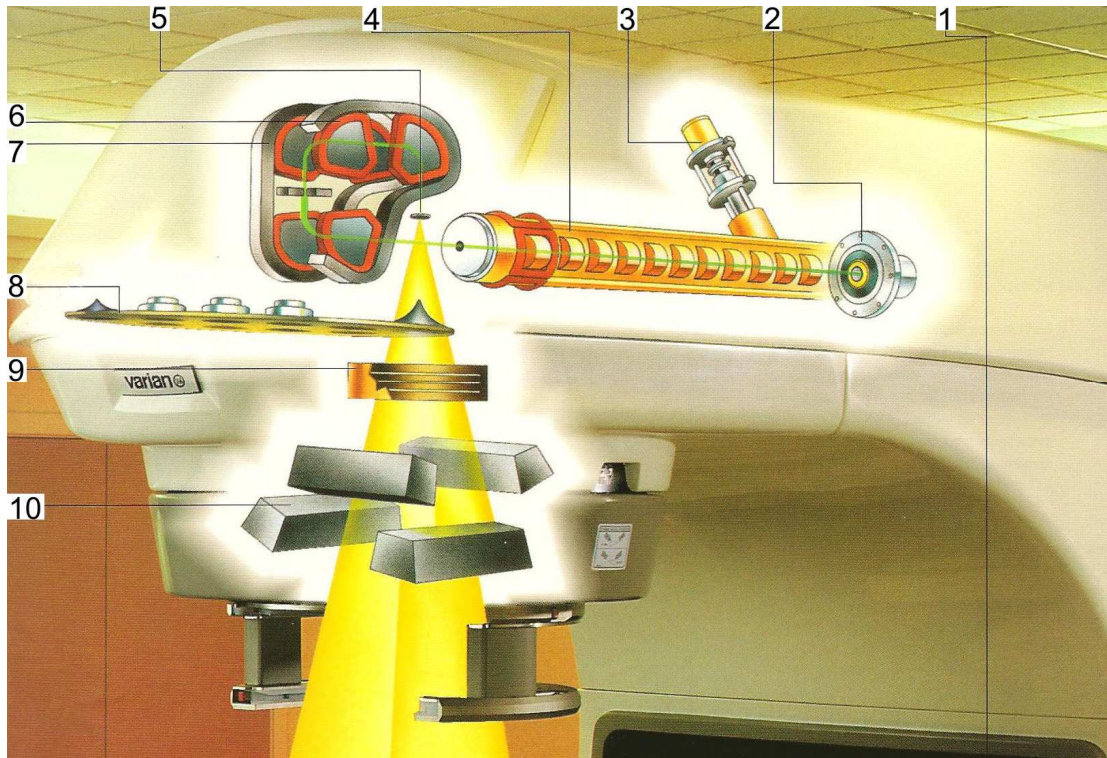
FIG. 38,   *Schematic view of the Varian CLINAC 2300C/D [25]*

The following annotations are taken out of the official Varian manual:

1) **Klystron Power Source:** A Klystron provides the RF power needed at a frequency of 2856 MHz (S band).

2) **Gridded Electron Gun:** The electron gun is gridded and gateable for dynamic treatments. It can be easily demounted and cost-effectively replaced.

3) **Energy Switch:** A patented energy switch provides energies at stable doserates and spectral purity.

4) **Standing Wave Accelerator Guide:** This accelerator tube uses the standing wave guide principle, where the microwave is reflected at the end of the tube and interferes with itself. It is optimized for high dose rates, good bunching, stable dosimetry and low-stray radiation.

5) **Focal spot size:** An achromatic bending magnet keeps the spot size at the target below 3 mm even at high dose rates.

6) **Steering System:** Radial and transverse steering coils and a real time feedback system provide beam symmetry within 2 % at all gantry angles.

7) **Achromatic Dual-Plane Bending Magnet:** The magnet bends the beam by 270° and includes ±3 % energy slits to ensure exact replication of the input beam.

8) **10-Port Carousel with Scattering Foils and Flattening Filters:** The electron scattering foils provide homogenous electron beams at therapeutic depths while the flattening filters flatten the x-ray beams.

9) **Ion Chamber:** Two independently sealed monitoring ion chambers, independent of temperature and pressure changes, monitor beam dosimetry within 2 %.

10) **Asymetric Jaws:** Four independent collimators provide flexible beam definition of symmetric and asymmetric fields.

1.2 Varian aS1000 EPID

The Varian aS1000 EPID (Portal Vision, Varian Medical Systems, Palo Alto, CA) is an amorphous silicon based detector with a sensitive active area of 40 x 30 cm^2. The device is basically a matrix of 1024 x 768 pixels with a pixel size of 0.039 x 0.039 cm^2. A simplified version of the EPID consists of the following layers along beam direction [12]:
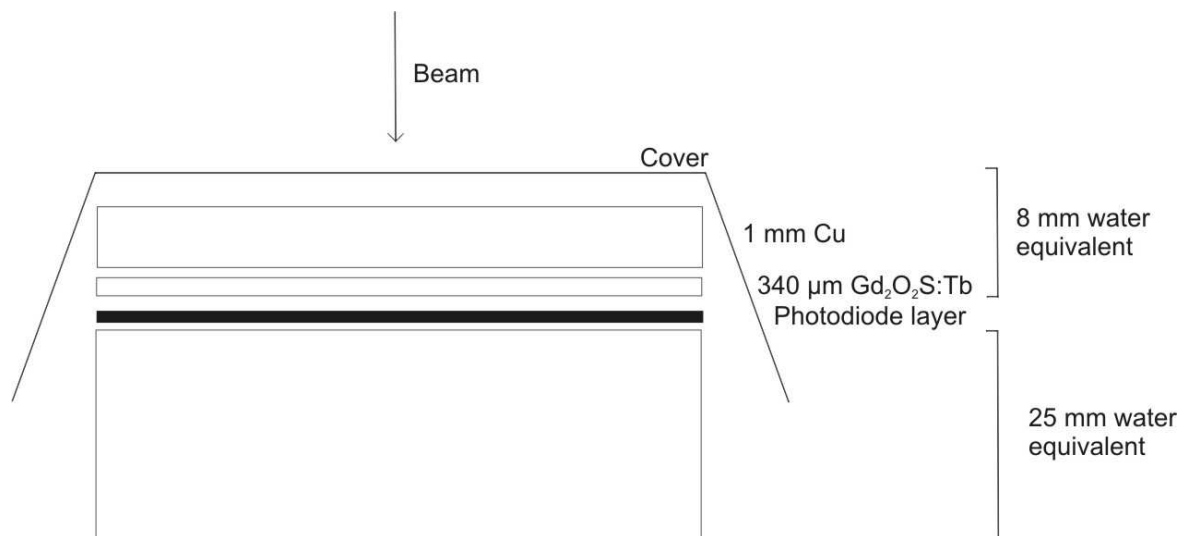
FIG. 39,   Schematic of the simplified EPID-mode

EPID Cover: Here, one part of the Collision detection system is located, which activates a motion interlock to prevent damages on the patient or the device itself. Apart from that the cover protects the detector surface from impacts.

1 mm Copper: This layer absorbs photons and emits recoil electrons. At the same time it protects the scintillation screen from any scattered radiation, especially against low Energy photons (< 1 MeV), because this scintillation screen is oversensitive for

these photons. [13]

340 µm Gd$_2$O$_2$S:Tb: The scintillation screen used in this EPID is a Kodak Lanex Fast B. It is made of Gadolinium Oxysulfide (Gadox) doped with Terbium, which is a very efficient scintillation material in terms of light output per incident x-ray energy and its high atomic number and density make it an effective absorber of x-ray photons. Gadox is produced as a homogenous layer of small crystalline particles. That means any light produced is rapidly scattered and diffuses before it is intercepted in the detector. This is the reason why thick layers of Gadox cannot be used for applications requiring high resolutions, although they are good at absorbing high-energy photons. [22]

Photodiode layer on 1 mm of glass substrate: The light that is produced by the scintillation screen is sensed by an a-Si panel.
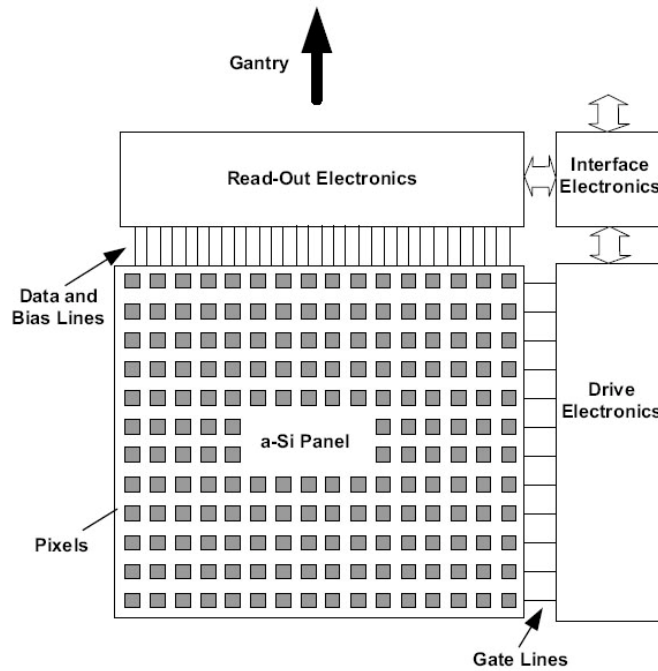
FIG. 40,   *Diagram of the Image Detection Unit (IDU) [26]*

Every pixel consists of a n-i-p photodiode and a Thin Film Transistor (TFT) deposited on a glass substrate. The photodiode integrates the received light and captures it as an electrical charge like a capacitor. When the TFT is switched to transparent by enabling the gate line, the electric charge stored in the photodiode is read out over the data line. [26]
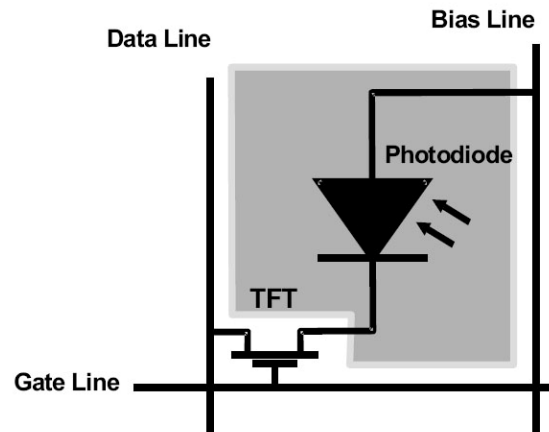
FIG. 41,   a-Si Pixel [26]

The rows are read out sequentially by enabling the gate line. The charge is captured using external charge amplifiers. When all rows are read out, one frame is acquired. Since the image readout timing of the EPID is synchronized with the linac beam pulse delivery, it varies with the linac repetition rate. [26]
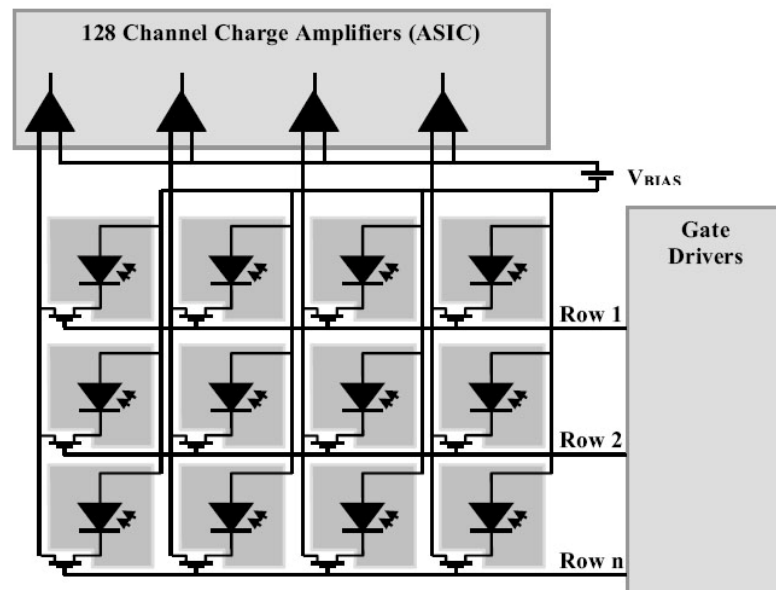
FIG. 42,   Segment of the detector array [26], [12]

Everything that is under the glass substrate, like electronics, mechanical systems and the EPID-housing, is estimated as 2.5 cm water equivalent. [34]

All layers above the detector layer are equivalent to 0.8 cm of water. [28]

1.3   Retractable arm

The EPID is held and moved by a retractable arm. The height positioning is limited between 180 cm SDD and 105 cm SDD. Collision detection is provided at the cassette cover, on the covers on both sides of the upper arm and on top of the counterweight cover. [29]
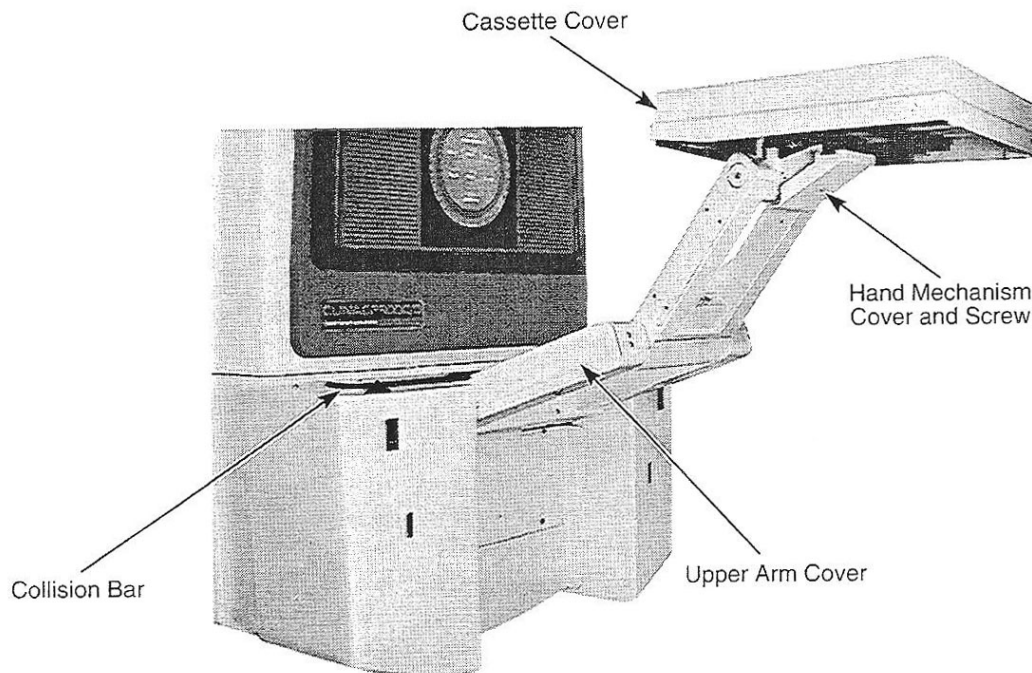
FIG. 43,   Retractable arm and EPID [29]

The arm is operated by an infrared hand pendant, where the three dimensions height, width and length can be changed separately. Because of the design of the arm, when changing the coordinates in one dimension, software has to compensate in the two other dimensions.

The arm can be calibrated in a so-called "physics mode", where the compensation of the software is disabled and each arm can be moved separately. In that mode 100 cm SDD can be reached and, when removing the cassette cover, a crosshair has to match the central axis of the beam for calibration. [29]

FIG. 44,   *EPID without cassette cover*

1.4   Waterphantom

The waterphantom used for the beam profile measurements and the field size measurements was the MP3 Phantom Tank by PTW. The tank stands on the MP3 Lifting Carriage manufactured by the same company. The tank has precision stepper motors to move an ionization chamber in all three dimensions, which can be controlled automatically by the software MEPHYSTO provided by PTW. The horizontal detector moving range is 600 x 500 mm^2 and the vertical range is 407.5 mm. The positioning accuracy of the stepper motors is ±0.1 mm. The MP3 Lifting carriage features additionally a height lifting range of approximately 40 cm. [18]
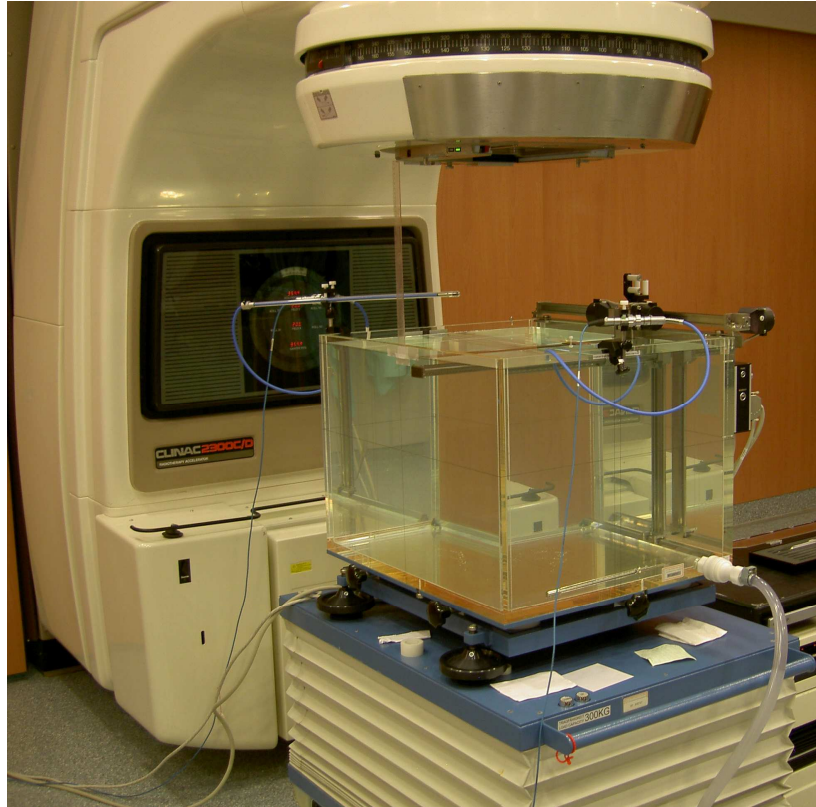
FIG. 45,   Waterphantom and lifting carriage

1.5   Waterproof PTW Pinpoint Chamber Type 31014

This vented ionization chamber was used in the waterphantom. It has a volume of 0.015 cm^3 and an inner diameter of 2 mm. The wall material is graphite with a protective acrylic cover. The voltage between the electrodes is between 300 V and 500 V. [20]

1.6   PTW Farmer Chamber Type 30010

This open ionization chamber was used inside a specially designed RW3 slab. It has a volume of 0.6 cm^3. This means the air density has to be corrected. The inner electrode is made of alloy and has a diameter of 1 mm. The Voltage between the electrodes is between 300 V and 500 V. [19]

1.7   PTW Unidos

This Universal Dosemeter was used in combination with the waterphantom and the Farmer Chamber Type 300001. It can provide voltages up to 400 V in steps of 50 V and the accuracy of measurements is at 10^{-15} A. The Dosemeter can measure

integrated dose (charge) or dose rate (current) or both simultaneously. [17]

1.8   PTW 2D-ARRAY seven29

The array consists of 729 vented cubic ionization chambers. The chambers are arranged with a centre to centre distance of 1 cm. This gives an active area of 27 x 27 cm^2. Each chamber has a volume of 0.125 cm^3 and the reference point is 5 mm below surface. [16]

FIG. 46,   PTW 2D-ARRAY seven29 [21]

1.9   RW3 Slab Phantoms

Made of water-equivalent RW3 material (Goettingen White Water) with a thickness tolerance of ±0.1 mm it makes depth dose measurements in a solid state phantom possible. The slabs are available in thicknesses of 1 mm, 2 mm, 5 mm and 1 cm so that any water depth needed, can be simulated. [18]

FIG. 47, *RW3-slabs on top of the EPID*

2 Dosimetric Calibration of the Electronic Portal Imaging Device

Calibration and acquiring of images is done with the software Varian IAS3 Maintenance. First the software has to be set to Integration Mode. Then a set of calibration images has to be taken, like in the normal calibration procedure for portal imaging.
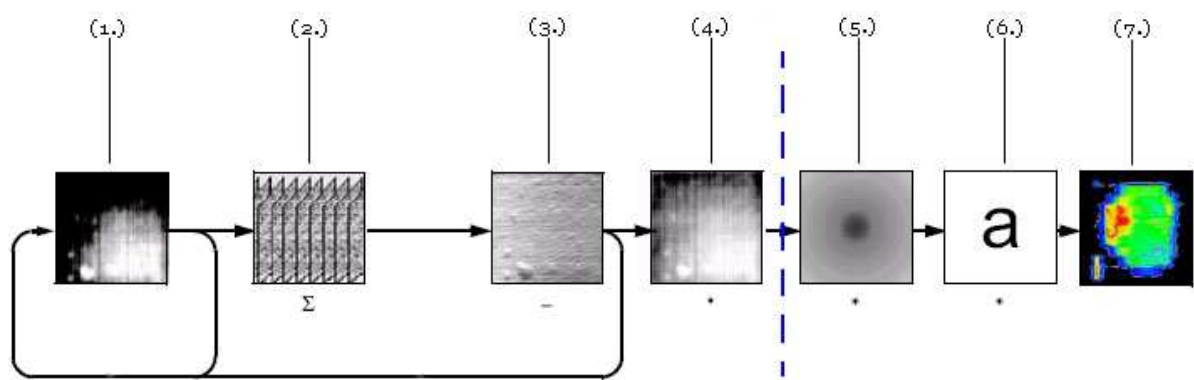
FIG. 48, *Calibration scheme of an amorphous silicon EPID [27]*

Fig. 48 shows all important steps, which are necessary to acquire a calibrated dose image with an amorphous silicon EPID.

(1.)   **Acquire raw frame**

(2.)   **Add to frame buffer**

(3.)   **Acquire dark field image**

The dark field image is taken without any incident beam by taking a number of images in quick succession.
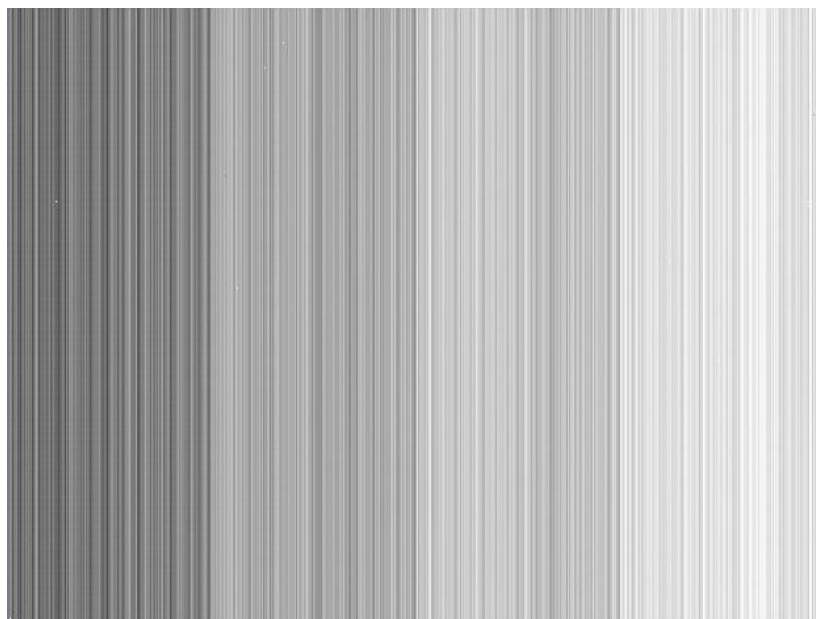
FIG. 49,   Dark field image

These images are then averaged over 30 frames for minimum noise. This should compensate for any array imperfections and electrometer offsets. Therefore the image is subtracted from the integrated raw image. The dark field image usually exhibits light and dark vertical stripes. [26]

(4.)   **Acquire flood field image**
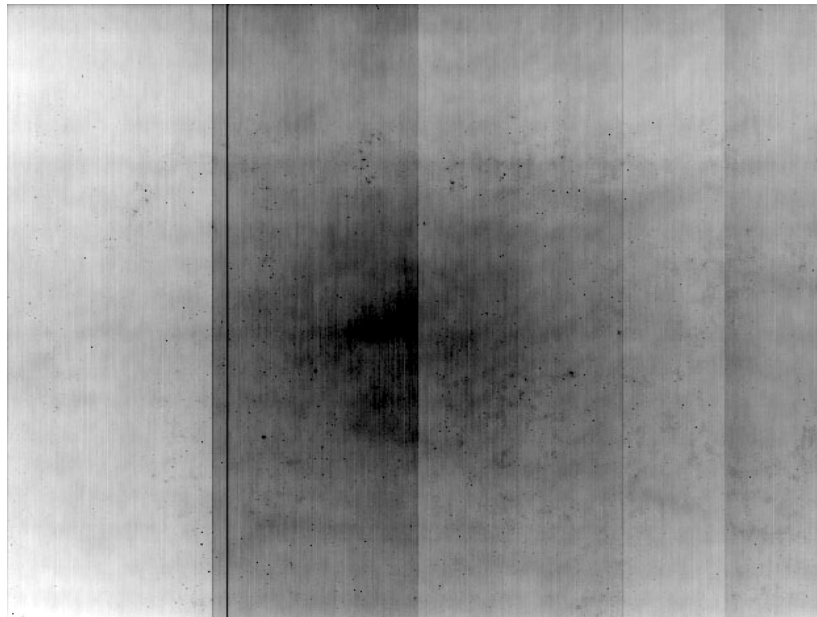
FIG. 50,   Flood field image

The flood field is taken with opened jaws at the desired energy and doserate. SDD has to be set and the beam must irradiate the whole sensitive area of the detector. The software stops automatically after acquiring 200 frames and averages over the 200 images. This should compensate for any field inhomogenities, different cell sensitivities and electrometer gains. Therefore the integrated raw image is divided by the flood field image.

The dark and flood field images have to be taken at the beginning of every measurement session or if parameters like energy, dose rate or SDD have changed.
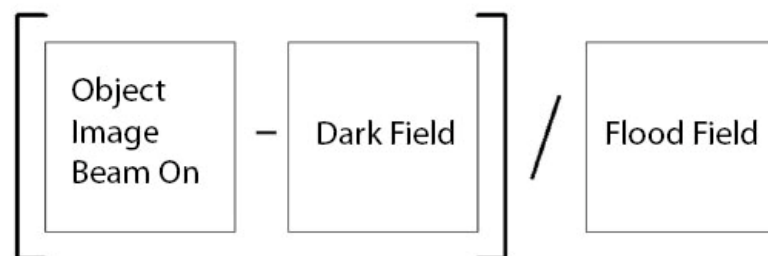
FIG. 51,   Standard correction scheme for dark and flood field images [26]

Fig. 51 shows the standard correction scheme for Gain and Offset. [26]

After that the dosimetric calibration has to be performed for each doserate at each of the available energies. Also important for an exact calibration is that the SDD is set to a distance which will also be used in further measurements. The procedure consists of a beam profile correction and the normalization for absolute dosimetry.

(5.)   Beam profile correction

The flood field correction assumes a uniform intensity across the field and ignores the beam's horns, which is sufficient for portal imaging but not for portal dosimetry. For the beam profile correction the software uses a diagonal profile of the largest possible field size opening of the accelerator and generates, based on the entered profile, automatically a radially symmetric correction. [27]
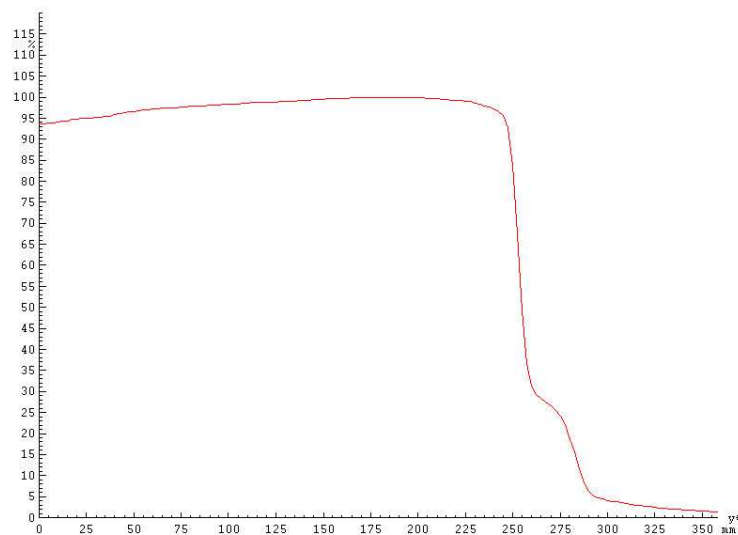
FIG. 52,   *Half sided diagonal profile for 6 MeV photons*

(6.)   Normalization

Finally, if the EPID is used for absolute dosimetry, the acquired data has to be normalized to a known dose. Of course it has to be considered, that the detector layer in the EPID is virtually in a water depth of 8 mm. [27]

Dose calculation example for an SSD of 145 cm with 6 MV photons:

In the calibration procedure for medical accelerators it is common that for 100 MU at a SSD of 100 cm and a fieldsize of 10 x 10 cm^2 the deposited dose equals exactly 1 Gy. This fact can be used to calibrate the EPID for absolute dosimetry. Since the

EPID can not be located at a SSD of 100 cm because of mechanical restrictions, the dose of 1 Gy has to be adapted. The dose at larger SSDs is calculated as follows [8]

$$D = \frac{M \cdot T \cdot F \cdot C}{100 \cdot O}$$

M   Number of chosen monitor units – in this case 100.

T   Relative depth dose – to get the percentage of dose in the depth of 8 mm the depth dose curves for the field sizes of 14 x 14 cm^2 and 15 x 15 cm^2 were taken from the base data of the accelerator and were interpolated to fit the fieldsize of 14.5 x 14.5 cm^2.

F   Mayneord F factor – while the actual dose rate at a point decreases with increasing SSD, the percent depth dose, which is a relative dose in respect to a reference dose (dose maximum in this case), increases with SSD. The Mayneord F factor provides the correction for the dependence of the percent depth dose on the SSD:

$$F = \left(\frac{f_2 + d_{max}}{f_1 + d_{max}} \right)^2 \cdot \left(\frac{f_1 + d}{f_2 + d} \right)^2$$

where d is the actual depth in the phantom and d_{max} is the depth of maximum dose. f_1 is the reference SSD and f_2 is the actual SSD.

C   Correction according to the inverse square law - photon fluence emitted by a point source of radiation varies inversely as a square of the distance from the source. Therefore the photon fluence at 145 cm has to be adapted with the correction term

$$C = \left(\frac{f_1 + d_{max}}{f_2 + d_{max}} \right)^2$$

O   Output factor – including the collimator scatter factor and the phantom scatter factor. In this case the collimator scatter factor is not necessary because the fieldsize does not change caused by a change of the collimator setting but because of the increase in SSD. The output factor principally depends on the

fieldsize and was measured during acquisition of the base data of the accelerator.

This gives a calculated dose of

$$\frac{100 \cdot 95.34 \cdot \left[\left(\frac{146.2+1.3}{100+1.3} \right)^2 \cdot \left(\frac{100+0.8}{146.2+0.8} \right)^2 \right] \cdot \left(\frac{100+1.3}{146.2+1.3} \right)^2}{100 \cdot 97.09} = 0.46173 \text{ Gy}$$

The software automatically shows the results in calibrated units (CU) which should be equivalent to Gy after that calibration.

3   Dosimetric characteristics of the aS1000 EPID

3.1   Linearity

A linear behaviour of the EPID is crucial for dosimetric measurements. The first measurement compares the preselected MUs with the calibrated detector output. During the measurement varying MUs are applied at a doserate of 300 MU/min in a field of 10 x 10 cm^2 at 6 MV and 15 MV. The SDD is set to 145 cm. A measurement with 6 MV and 5 cm of water equivalent RW3-plates placed on top of the EPID was performed additionally. At 15 MV the buildup layer on top is chosen to be 1 cm of RW3-material.

The second measurement is performed to show linearity of the PD over different SDDs which are equivalent to different dose rates. The results are averaged in a circle with a diameter of 30 pixels around the central beam. Therefore the inverse square law is needed to transform to linear results. For that measurement the EPID is calibrated at a SDD of 145 cm. Like in the first measurement 100 MUs 10 x 10 cm^2 are applied at a dose rate of 300 MU/min in a field of 10 x 10 cm^2 at 6 MV and 15 MV.

3.2   Fieldsize dependence of SDD

This measurement should show a linear increase of the field size with rising source to detector distance. The results are compared with waterphantom measurements in a water depth of 0.8 cm. Inside the waterphantom a pinpoint chamber by PTW with a Volume of 0.015 cm^3 is used. During the measurement 100 MUs are applied at a doserate of 300 MU/min in a field of 20 x 20 cm^2 at 6 MV and 15 MV. The SDDs are

measured from the source to the water surface, at the waterphantom and at the EPID. SDDs of 100 cm can not be reached by the EPID in normal mode.

The field sizes are determined in the program MEPHYSTO by PTW. The program defines the limit of the field as the point where 50 % of the dose, normalized to the central beam, are deposited.

The coordinate system which the x- and y-direction are referring to is shown in Fig. 53.
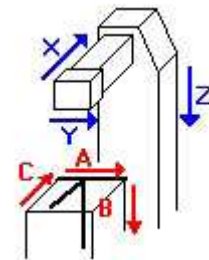
FIG. 53,   *Linac coordinate system*

3.3   Relative depth dose curve

This measurement shows the behaviour of the portal dose with increasing thickness of build-up material. Water-equivalent RW3 slabs (Goettingen White Water) produced by PTW are used as build-up. The slabs are put on top of the cover, while the SDD is increased by the height of the added slab. Thereby the distance from the source to the slab surface stays the same and a real depth dose curve is measured.

The curve is compared to a curve obtained through the use of the RW3 slabs in combination with a 0.6 cm^3 "Farmer"-chamber by PTW. The chamber is connected to a PTW-UNIDOS to integrate over the measured dose rate. [17]

The measurements start at a SDD of 145 cm and during the measurement 100 MUs are applied at a doserate of 300 MU/min in a field of 10 x 10 cm^2 at 15 MV for each depth. Measurements at 6 MV came out to be worthless because the depth of maximum dose at that energy is inside the EPID cover and the depth dose curves just show a decay of dose.

3.4   Ghosting

To examine the existence of a memory effect of the aSi based detector a small 5 x 5 cm^2 field is irradiated with 500 MU. As soon as possible afterwards (about 10 seconds later) a large field of 15 x 15 cm^2 and 10 MU is delivered. The resulting

image is compared to a reference image of 15 x 15 cm^2 and 10 MU without foregoing irradiation.

4   Comparison of IMRT test fields

For the planning procedure, the EPID is demounted and a computerized tomogram (CT) is taken. These slices are sent to the Varian Eclipse program, which is able to create a body in three dimensions out of the slices and interpret the grey values as Hounsfield units (HU). Then a field with a MLC sequence is added and the SSD is set to 145 cm. Based on a setup like this, as close as possible to real EPID setup, the program calculates the dose distribution in the body of the EPID. After estimating the location of the detector layer in the EPID, the dose distribution in the detector layer can be read out and saved. These dose maps are used as reference images for all further comparisons.
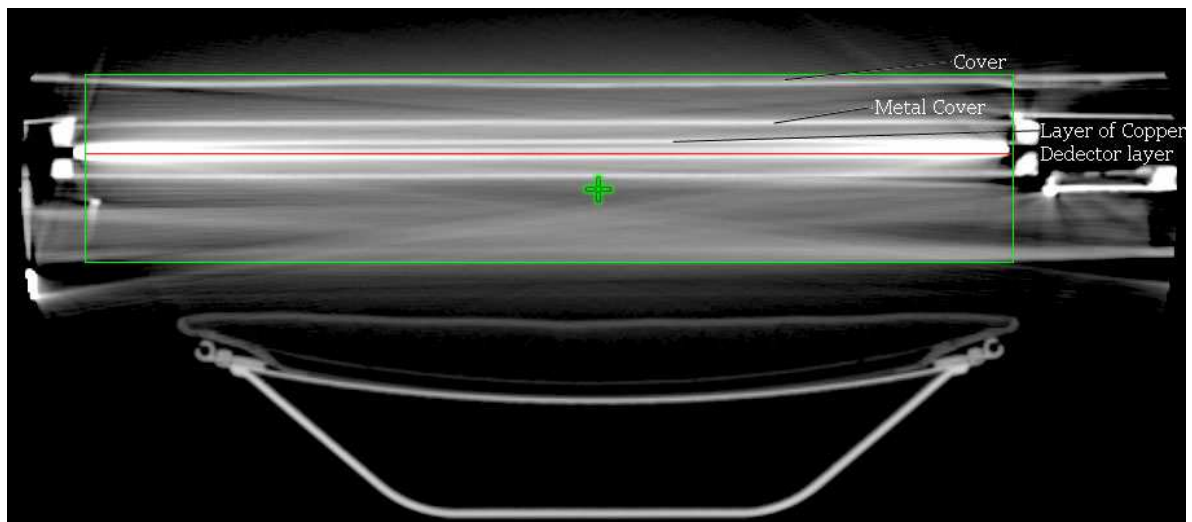
FIG. 54,   CT-slice in transversal direction of the Varian aS1000 EPID

Fig. 54 shows a CT image of the Varian aS1000 EPID. The author tried to identify all visible layers of the EPID, identified the detector layer and marked it with a red line in the figure. The green box marks the body limits for the software.

The picture shows artefacts, especially at the sides of the EPID, but in spite of that the calculated dose matrices fit the measured ones. The reason for the good result is that the field at this SSD is less than 15 cm wide, which is the area where the artefacts are at a tolerable level.

The direction of movement of the MLC leafs on the images is always in horizontal direction.

4.1   Tests

The next step on the way to finally compare IMRT plans is to create test patterns to find weaknesses and inaccuracies in the EPID's image acquisition. Therefore seven test patterns with a fieldsize of 10 x 10 cm^2 are designed with the goal to detect problems of the EPID. The matrices are assembled with a Java based computer program, where the relative fluence for each pixel can be set. The pixel size for the following matrices is 2.5 mm. The program creates text files, which are used by the planning software to calculate IMRT dose distributions. The software then creates MLC files, which can be read by the MLC controlling computer. The gamma evaluation method is chosen for comparison of the measurements with the planned dose matrices. For all test patterns the DTA is chosen to be 3 mm and the relative dose difference is set to 3 %. Compared to other publications, like Dinesh Kumar M. (2006) [4], these are quite low limits for matrices with very complex patterns and high gradient areas but the test patterns should reveal problems in image acquisition and therefore these low limits are justified. All measurements were taken, using photon beams with a maximum energy of 6 MV and at a doserate of 300 MU/min, while SDD was set to 145 cm.

4.1.1   Test1: 4 vertical stripes with increasing relative fluencies

This pattern consists of 4 vertical steps with relative fluencies from 25 % to 100 %. It shell result in large areas of homogenous dose.
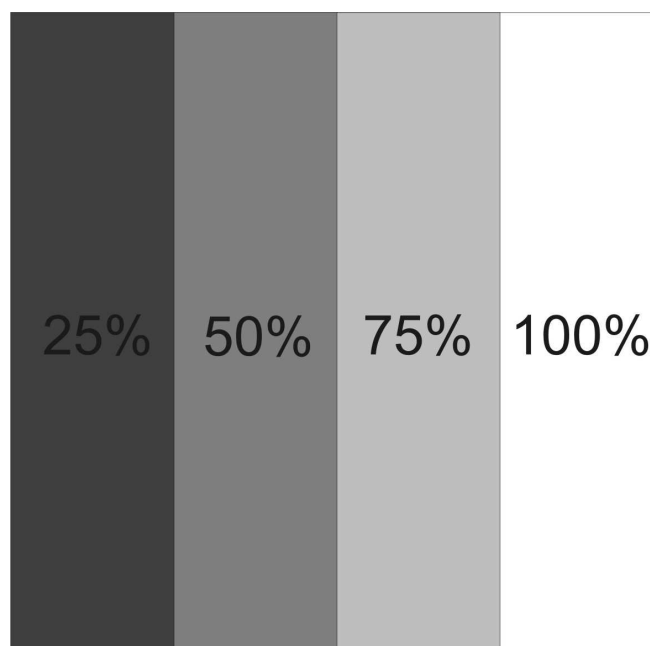
FIG. 55,   Test1: 4 vertical stripes with increasing relative fluencies

4.1.2   Test2: triangles

This pattern shows borders which are neither rectangular nor parallel to the movement direction of the MLC leafs and are therefore difficult to calculate for the software. Additionally, the triangle with 30 % relative fluency on the right hand side of the matrix is very thin.
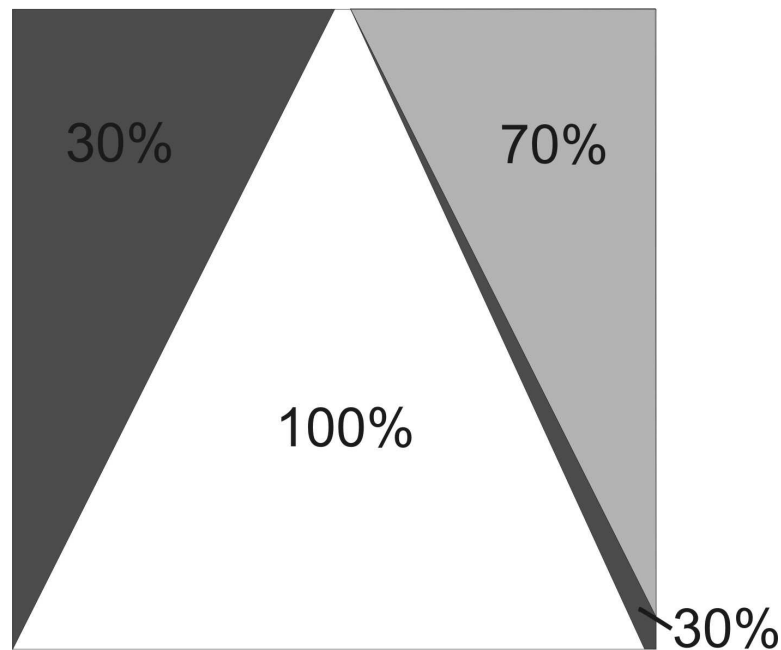
FIG. 56,   *Test2: triangles*

4.1.3   Test3: fluence gradient in horizontal direction

This pattern shows a simple horizontal gradient from 0 % to 100 % relative fluency.
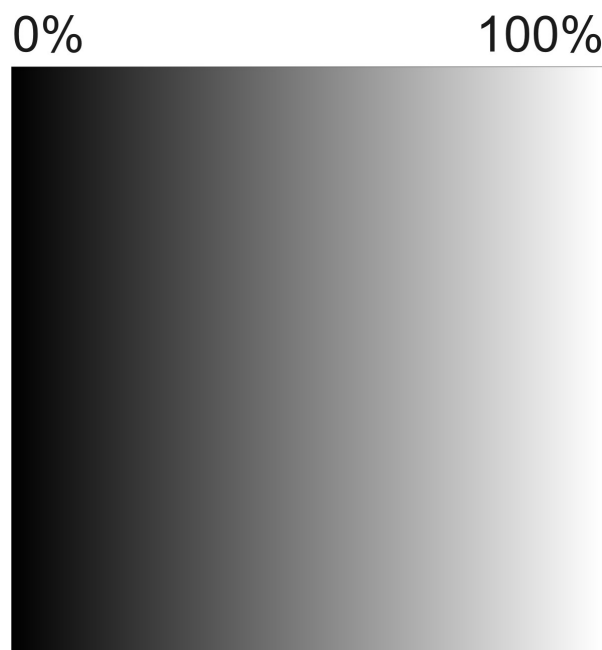
FIG. 57,   *Test3: fluence gradient in horizontal direction*

4.1.4   Test4: 10 vertical stripes

This pattern shows 10 vertical stripes alternating with 0 % and 100 % relative fluency. Between the stripes the highest possible gradient occurs.
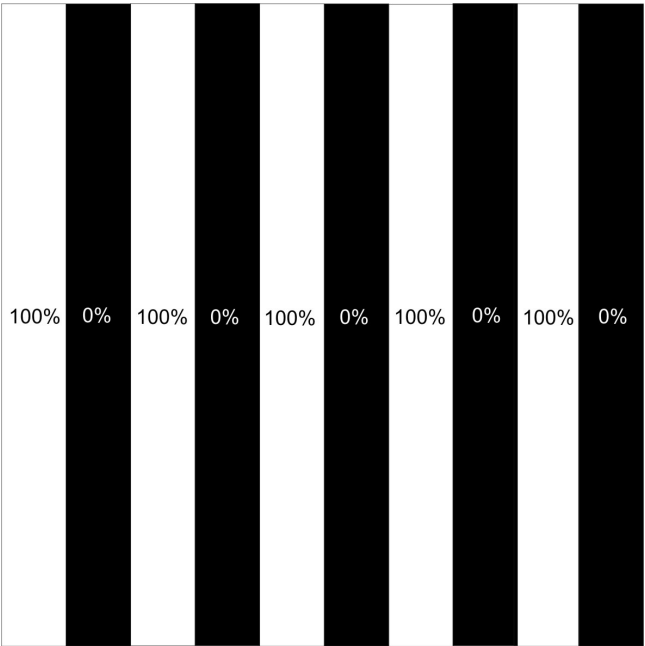
FIG. 58,   Test4: 10 vertical stripes

4.1.5   Test5: 20 vertical stripes

This pattern consists of 20 vertical stripes alternating with 0 % and 100 % relative fluency. The broadness of each stripe is very small and therefore the demand on the precision of the MLC is very high. Again the gradient between the stripes is at maximum value.
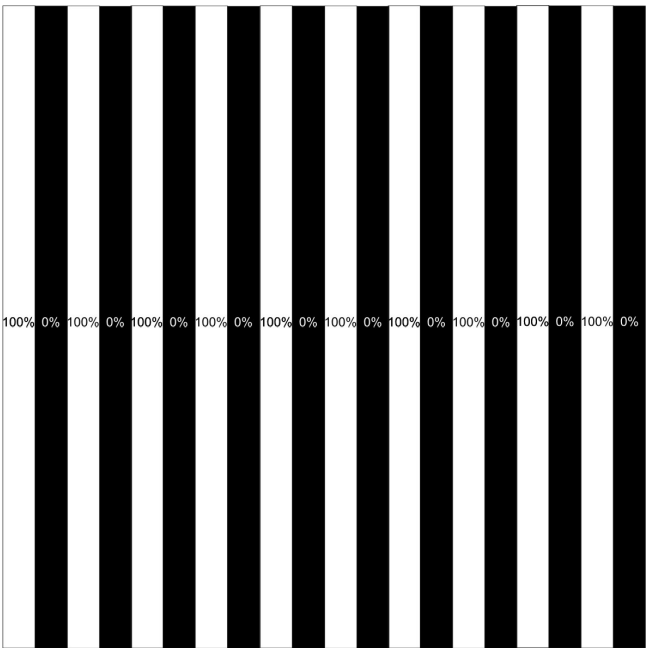
FIG. 59,   Test5: 20 vertical stripes

4.1.6   Test6: 14 vertical stripes, separated by a horizontal line and shifted

This pattern consists of many stripes with different relative fluencies, but additionally in the middle of the matrix there is a shift in the pattern. This shift creates dose areas where 4 different relative fluencies come together, separated by a region of high gradient.
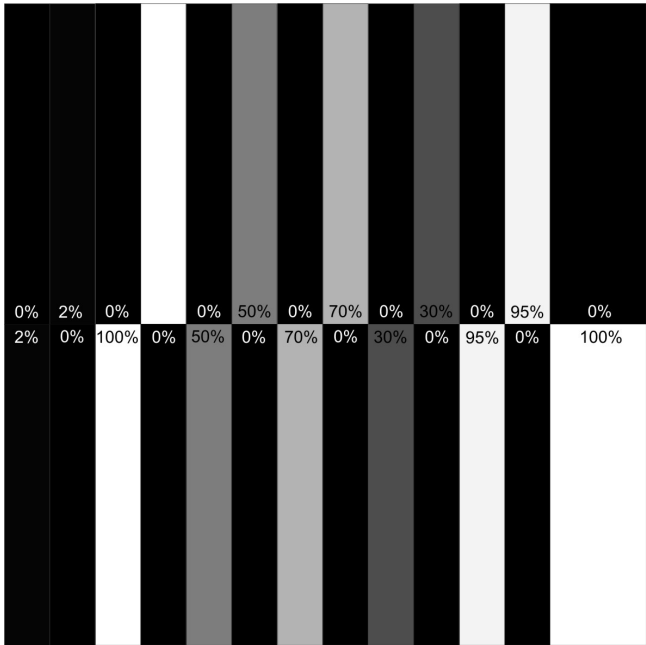
FIG. 60,   *Test6: 14 vertical stripes, separated by a horizontal line and shifted*

4.1.7   Test7: three vertical stripes with different relative fluencies

This pattern shows 3 horizontal steps with different relative fluencies between 20 % and 70 %.
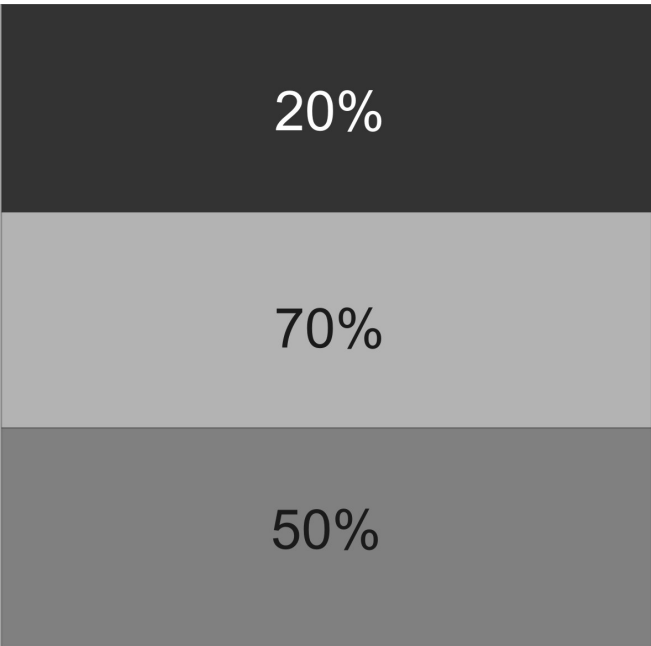
FIG. 61,   *Test7: three vertical stripes with different relative fluencies*

4.2   Comparison between Varian aS1000 EPID and PTW 729 array

The PTW 729 array has been previously used for verification of IMRT plans in the Landesklinikum Wiener Neustadt. But since the array has a very low resolution of 27 x 27 chambers and a low spatial resolution of 1 cm between the chambers the verification procedure has been not very reliable. The use of the aS1000 EPID should bring an improvement in resolution and reliability. Therefore comparison measurements are performed. For the array-measurements the PTW 729 is placed on the couch with 0.3 cm of RW3 slabs for buildup on top of it and 2 cm slabs for back scatter below. By this setup the geometric condition of the EPID should be simulated as good as possible.

The results of these measurements were compared with the planned dose matrices just like the EPID measurements previously. Therefore the PTW 729 array is scanned in the CT and the test patterns are planned on the three dimensional body of the array. Afterwards the dose distributions in the depth of the ionization chambers, marked by a red line in Fig. 62 were extracted.
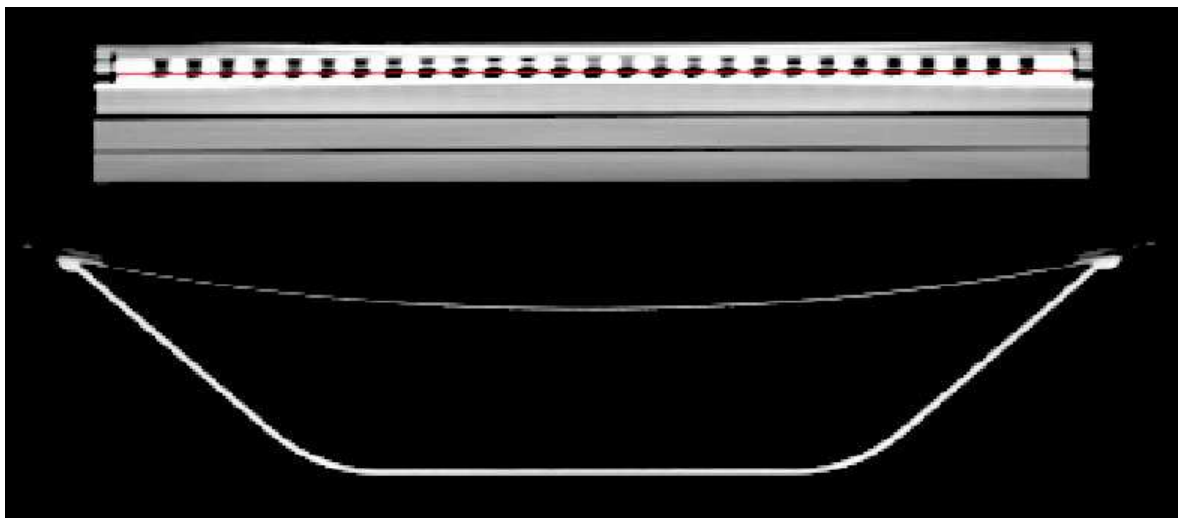
FIG. 62,   *CT-slice in transversal direction of the PTW 729 array*

4.3   Verification of real patients' IMRT plans

To compare real IMRT treatment plans the patient's plans are recalculated by the planning program based on the CT-image of the EPID. The SDD is again set to 145 cm and all fields are irradiated at 6 MV photon energy and 300 MU/min doserate. The gamma evaluation method is used to compare planned and measured dose distributions. As proposed by Dinesh Kumar (2006) [4], the criteria for complex IMRT

fields are set to 4 % relative dose difference and 4 mm DTA.

4.3.1   Treatment plan: patient 1 H&N
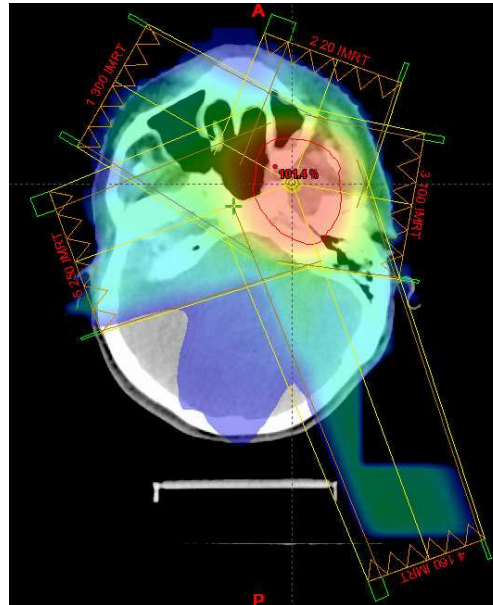
FIG. 63,   Planned dose distribution in patient 1

Patient 1 has a sphenoid tumour on the left side. The picture shows the planned dose distribution of an axial slice as colour-wash. The treatment was planned with 5 IMRT fields shown in the image.

4.3.2   Treatment plan: patient 2 H&N
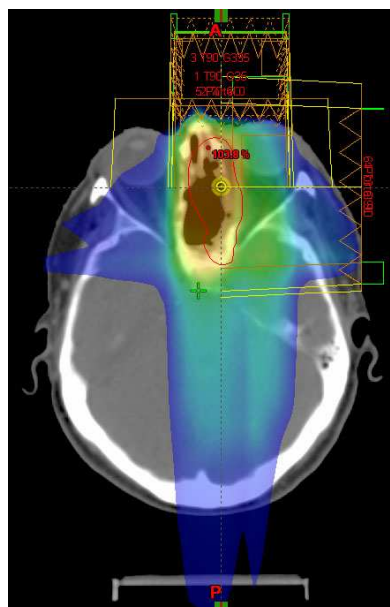
FIG. 64,   Planned dose distribution in patient 2

Patient 2 has a tumour in the paranasal sinuses. The picture shows the planned dose distribution of an axial slice as colour-wash. The treatment was planned with 4 IMRT fields. Additionally 2 portal image fields, used to control the patient's position, are shown in the image.

4.3.3   Treatment plan: patient 3 H&N
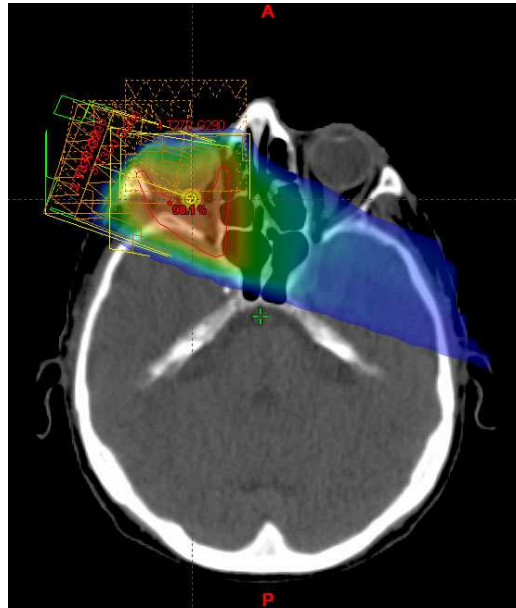
FIG. 65,   Planned dose distribution in patient 3

Patient 3 has a squamous cell carcinoma in the right orbita. The picture shows the planned dose distribution of an axial slice as colour-wash. The treatment was planned with 4 IMRT fields shown in the image.

4.3.4 Treatment plan: patient 4 prostate
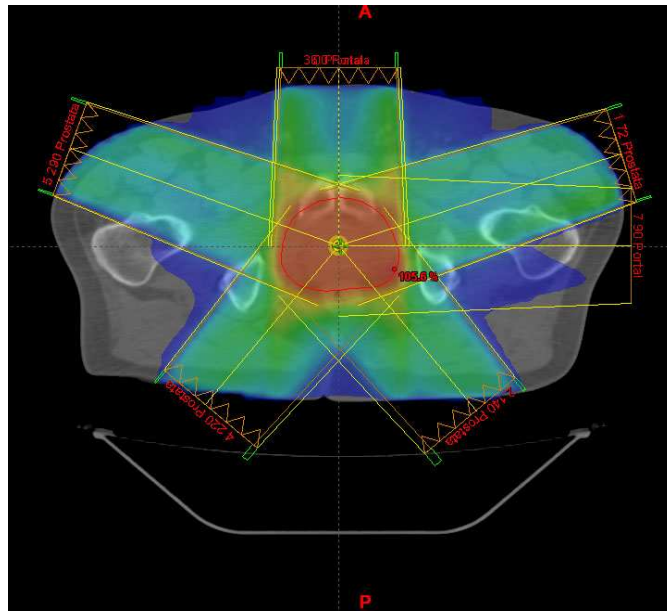
FIG. 66, Planned dose distribution in patient 4

Patient 4 has a prostate carcinoma. The picture shows the planned dose distribution of an axial slice as colour-wash. The treatment was planned with 5 IMRT fields. Additionally 2 portal image fields, used to control the patient's position, are also shown in the image.

4.3.5 Treatment plan: patient 5 prostate
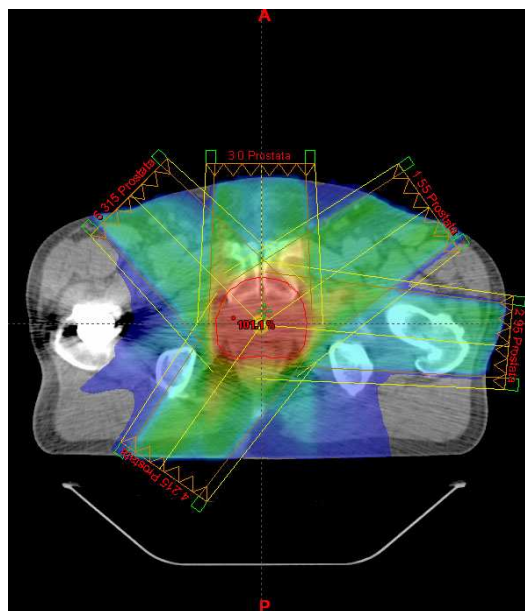
FIG. 67, Planned dose distribution in patient 5

Patient 5 has a prostate carcinoma. The picture shows the planned dose distribution of an axial slice as colour-wash. The treatment was planned with 5 IMRT fields shown in the image.

4.3.6   Treatment plan: patient 6 prostate
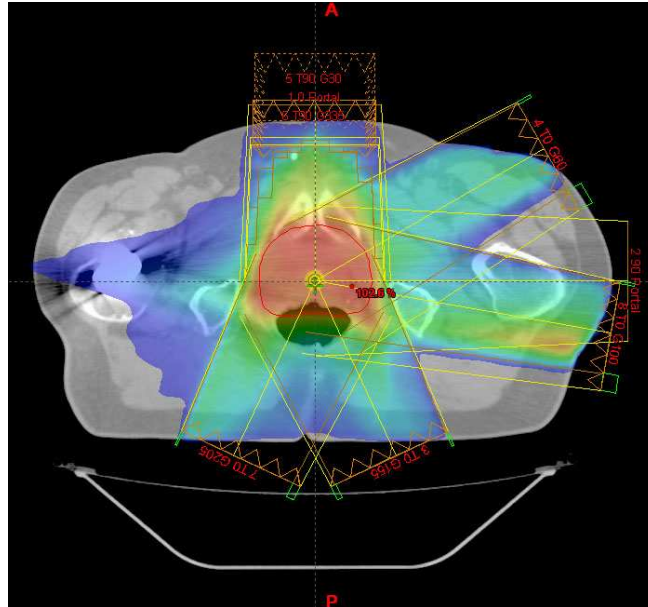
FIG. 68,   *Planned dose distribution in patient 6*

Patient 6 has a prostate carcinoma. The picture shows the planned dose distribution of an axial slice as colour-wash. The treatment was planned with 6 IMRT fields. Additionally 2 portal image fields, used to control the patient's position, are shown in the image.

Results

1   Dosimetric characteristic of the aS1000 EPID

All results are shown in Calibrated Units which should be equivalent to Gray if the EPID is calibrated for absolute dosimetry.

1.1   Linearity

The linearity of the detector response in dosimetric acquisition mode is illustrated in Fig. 69 for 6 MV photons and in Fig. 70 for 15 MV photons. The solid lines show a linear fit.
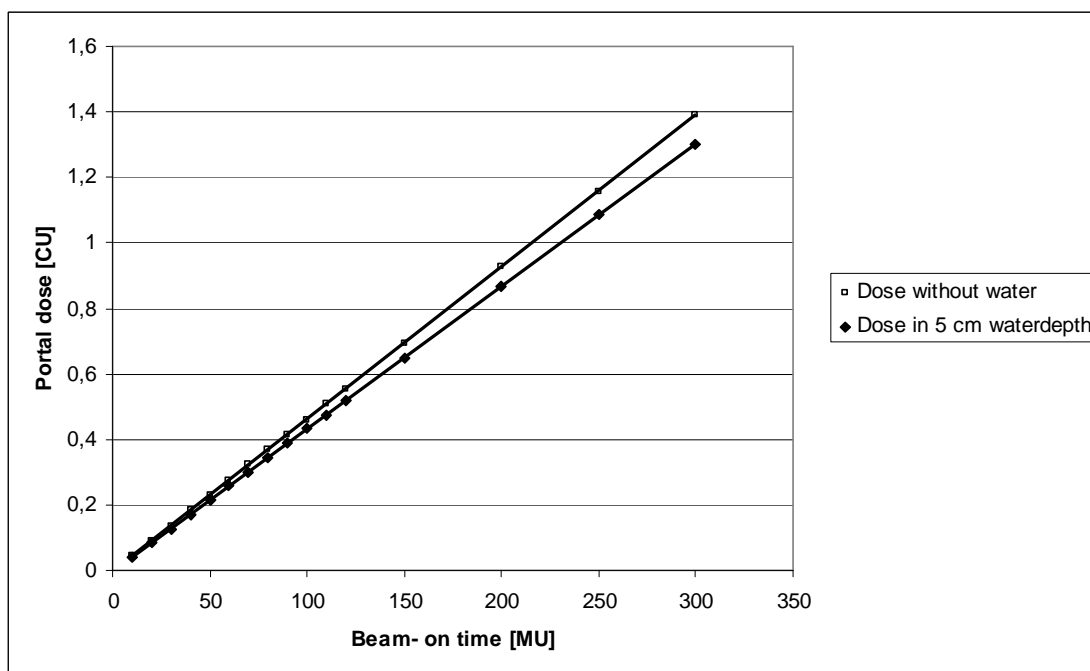
FIG. 69,   *Linearity at 6 MV*
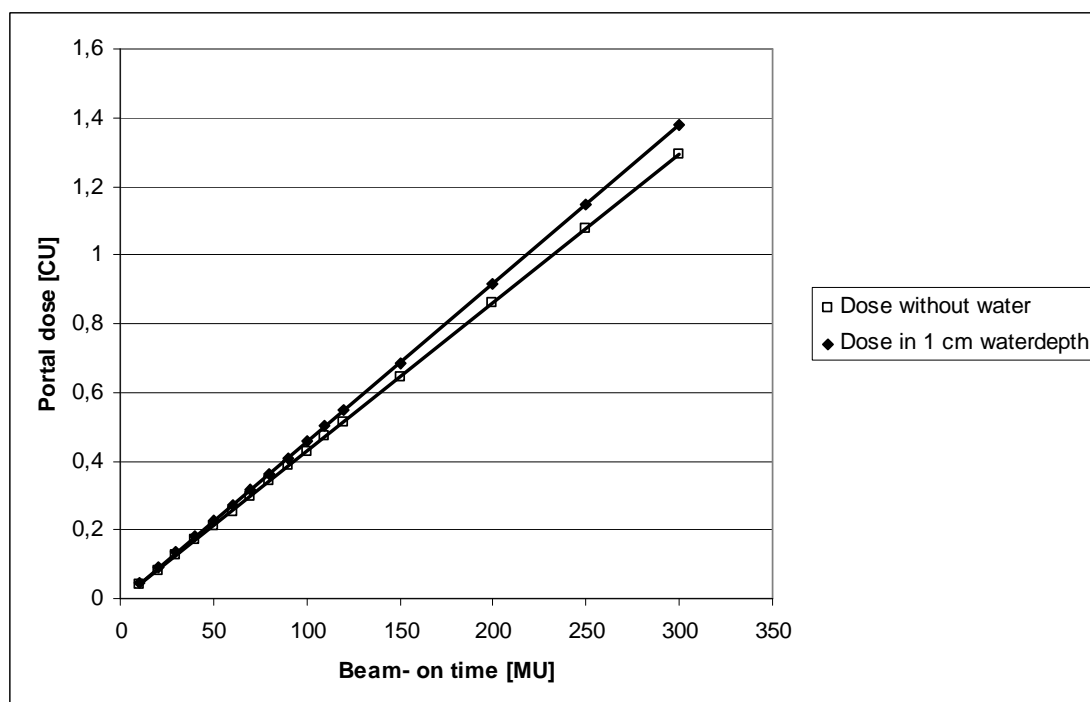
FIG. 70,   *Linearity at 15 MV*

The detected EPID dose is proportional to the amount of preselected MUs over the range of 10 – 300 MU. Above 10 MU the measured EPID dose is within 2 % of the expected value. Below 20 MU the accuracy starts to decrease. This effect is in accordance with the results of A. van Esch et al. (2004) and is shown in tables 4-7. [30]

TAB. 4,   *Deviations from the linear fit for low doses at 6 MV*

dose	dose	calculated	difference	Deviation
[MU]	[CU]	[CU]	[CU]	[%]
10	0.044	0.0428	0.0012	2.80
20	0.09	0.0888	0.0012	1.35
30	0.135	0.1348	0.0002	0.15
40	0.182	0.1808	0.0012	0.66
50	0.229	0.2268	0.0022	0.97
60	0.276	0.2728	0.0032	1.17
…	…	…	…	…

TAB. 5,   *Deviations from the linear fit for low doses at 6 MV in 5 cm of water*

dose	dose	calculated	difference	Deviation
[MU]	[CU]	[CU]	[CU]	[%]
10	0.041	0.0405	0.0005	1.23
20	0.084	0.0845	0.0005	0.59
30	0.127	0.1285	0.0015	1.17
40	0.171	0.1725	0.0015	0.87
50	0.213	0.2165	0.0035	1.62
60	0.257	0.2605	0.0035	1.34
…	…	…	…	…

TAB. 6,   *Deviations from the linear fit for low doses at 15 MV*

dose	dose	calculated	difference	Deviation
[MU]	[CU]	[CU]	[CU]	[%]
10	0.041	0.0392	0.0018	4.59
20	0.083	0.0822	0.0008	0.97
30	0.126	0.1252	0.0008	0.64
40	0.169	0.1682	0.0008	0.48
50	0.212	0.2112	0.0008	0.38
60	0.254	0.2542	0.0002	0.08
…	…	…	…	…

TAB. 7,   *Deviations from the linear fit for low doses at 15 MV in 1 cm of water*

dose	dose	calculated	difference	deviation
[MU]	[CU]	[CU]	[CU]	[%]
10	0.043	0.0421	0.0009	2.14
20	0.089	0.0881	0.0009	1.02
30	0.134	0.1341	0.0001	0.07
40	0.18	0.1801	0.0001	0.06
50	0.226	0.2261	1E-04	0.04
60	0.272	0.2721	1E-04	0.04
…	…	…	…	…

The result of the second measurement is shown in Fig. 71. The solid lines show a
linear fit.
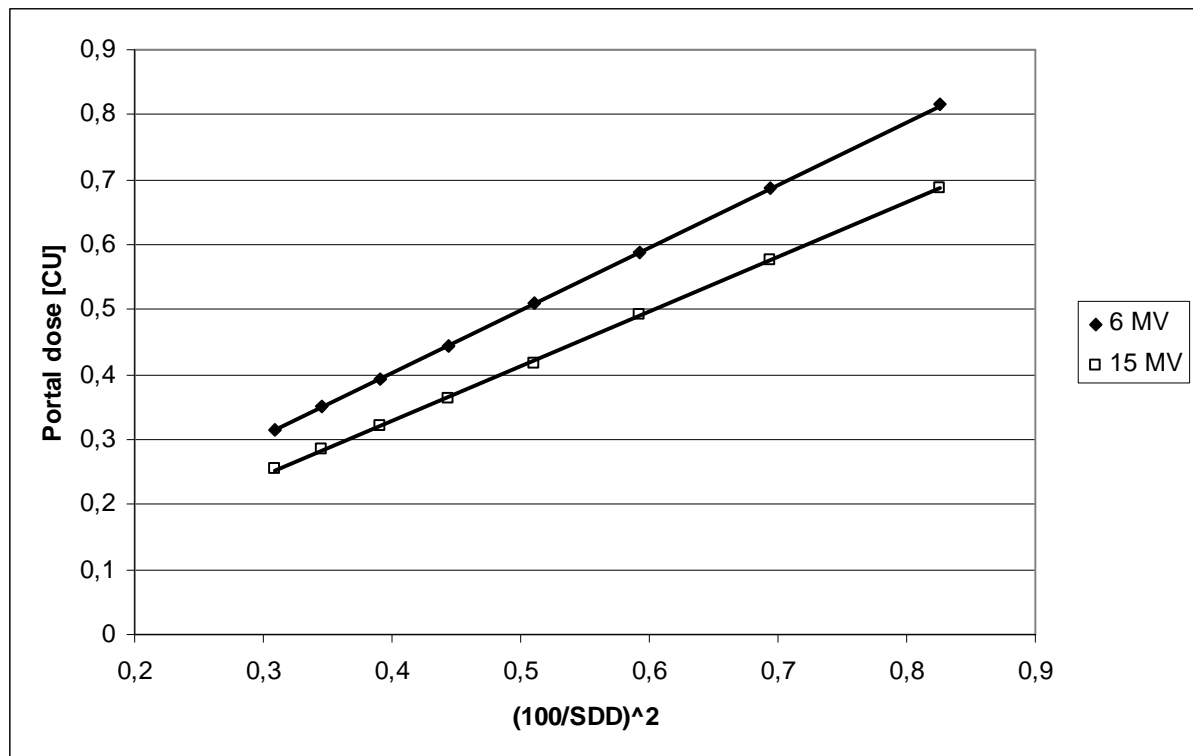
FIG. 71,   *Portal dose over SDDs (= dose rates)*

The results show good linearity, especially for the 6 MV measurements where the error is around 0.1 %. For the 15 MV the results are linear but show an error up to 1 % according to Van Esch et al. (2004) [30].

1.2   Fieldsize dependence of SDD

The following graphs show the field size dependence of the SDD. The solid line shows the ideal linearity based on the waterphantom measurement at an SDD of 100 cm.
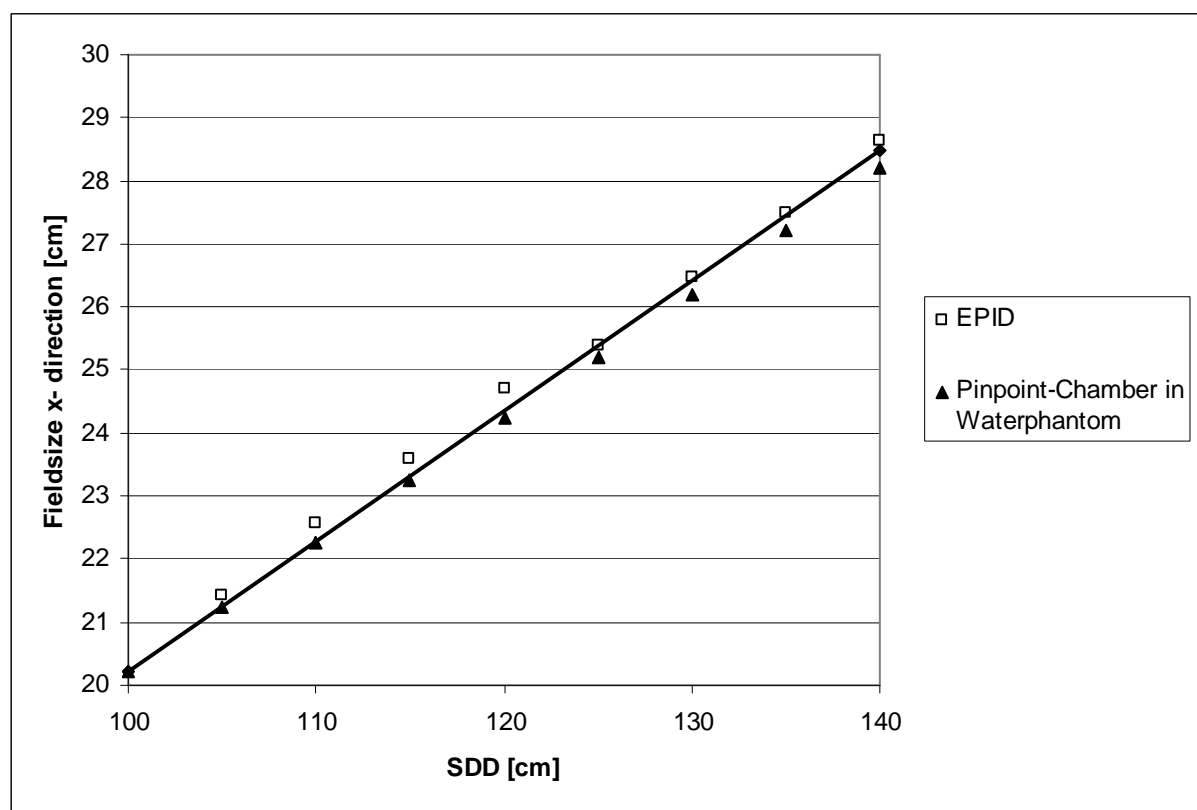
FIG. 72,   Fieldsize in x- direction at 6 MV
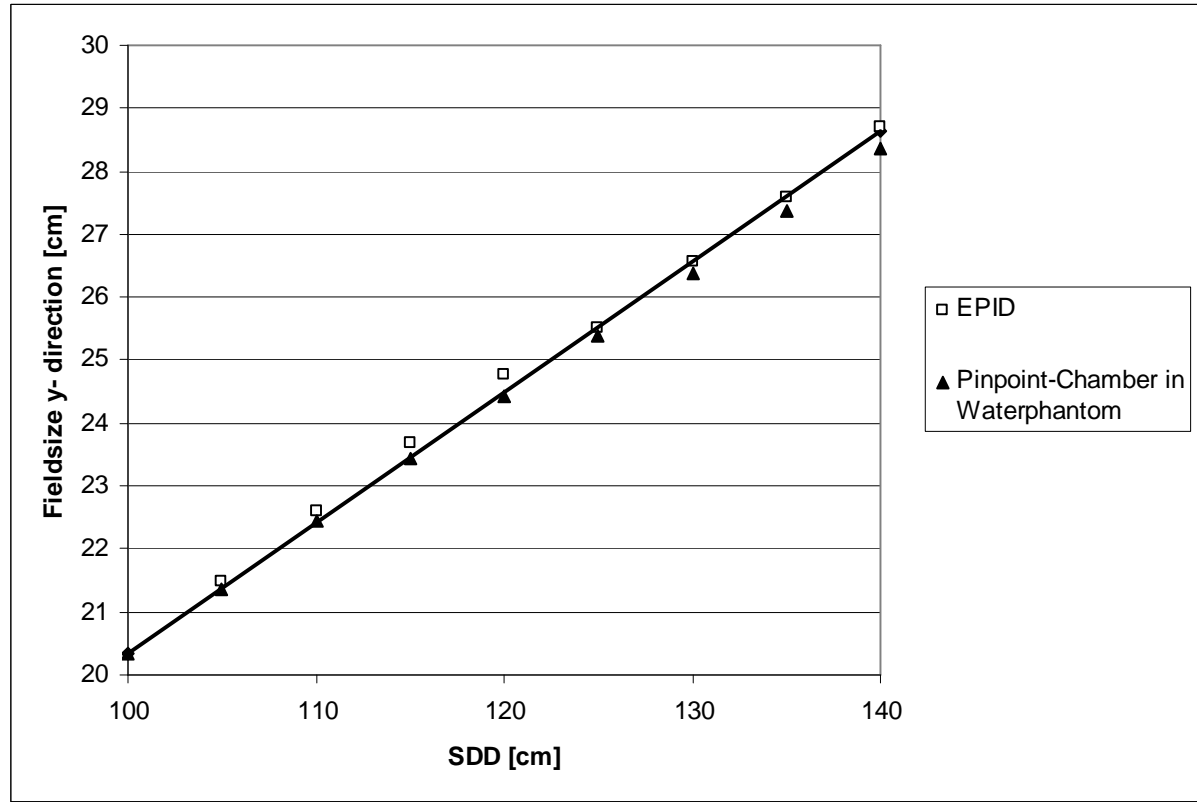
FIG. 73,   Fieldsize in y- direction at 6 MV
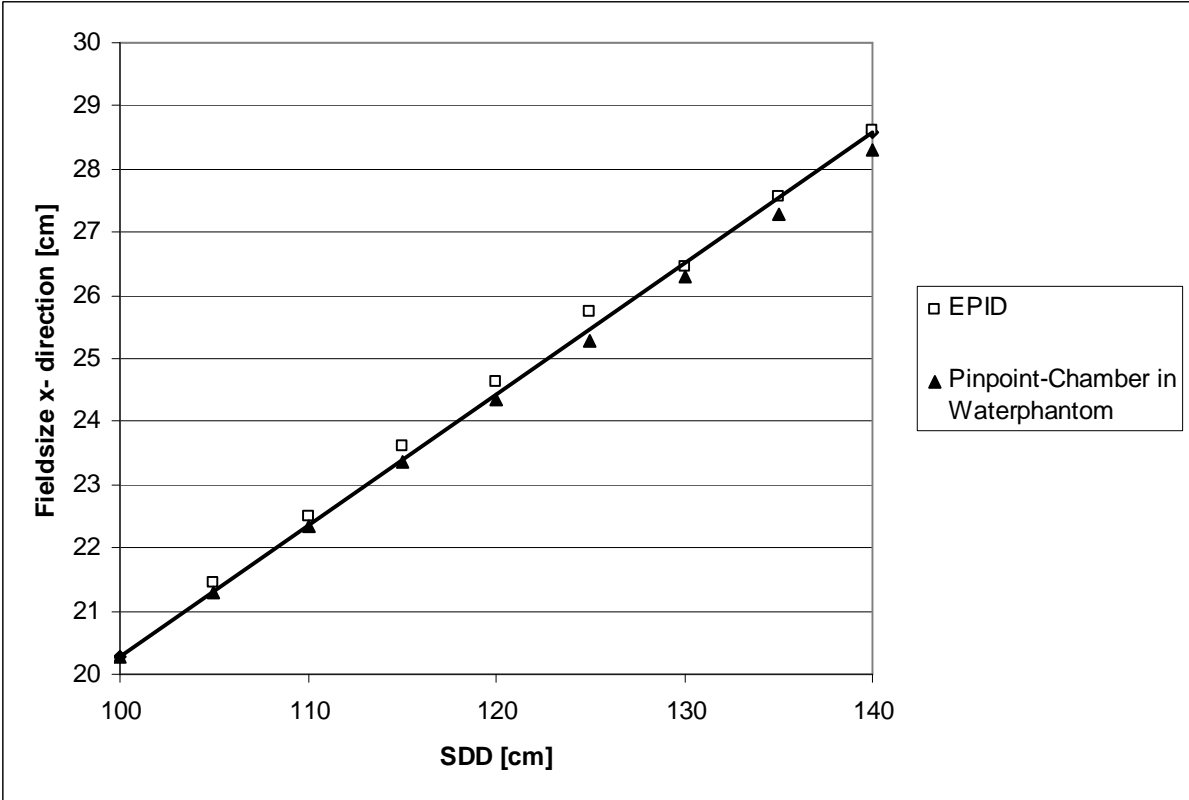
FIG. 74,   *Fieldsize in x- direction at 15 MV*
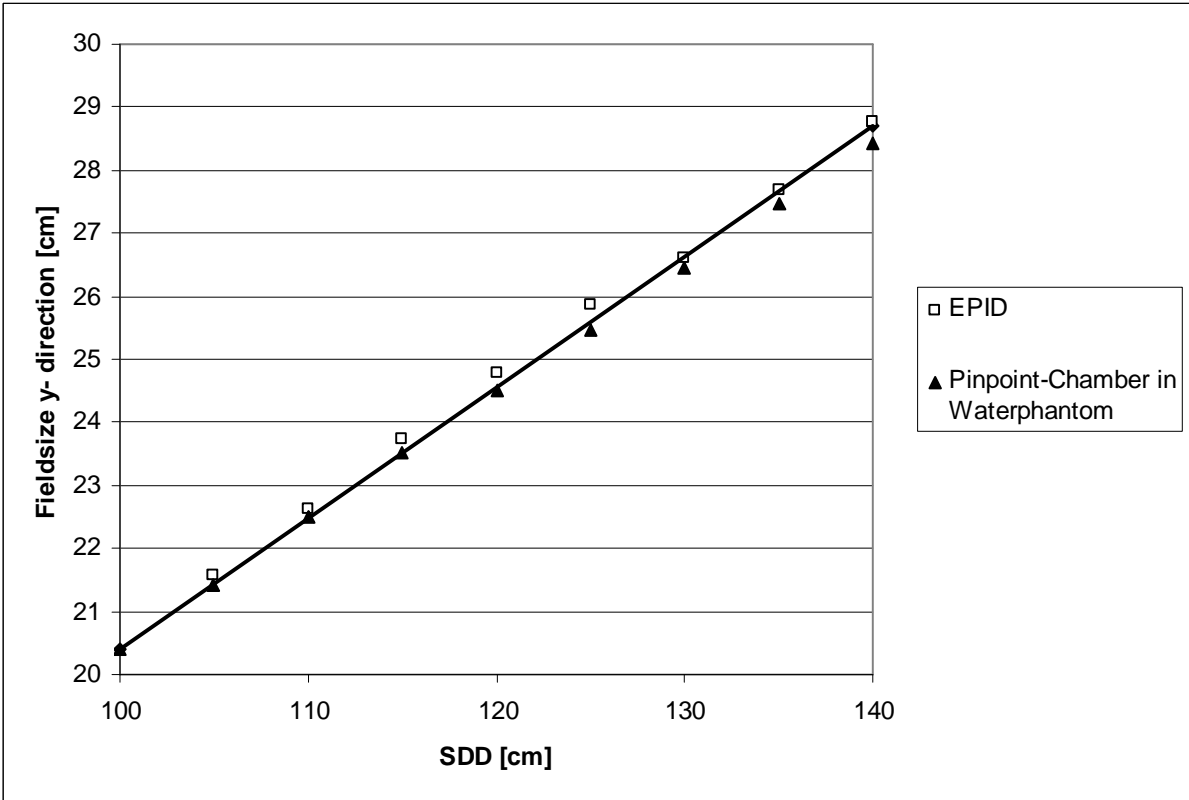
FIG. 75,   *Fieldsize in y- direction at 15 MV*

The results by the EPID show errors up to 2 % while the results of the waterphantom

deviate below 1 %.

1.3   Relative Depth dose Curve

The following graph shows the depth dose curves normalized to the maximum dose. 0.8 cm water-equivalent material above the detector surface [28] is already included in the depth.
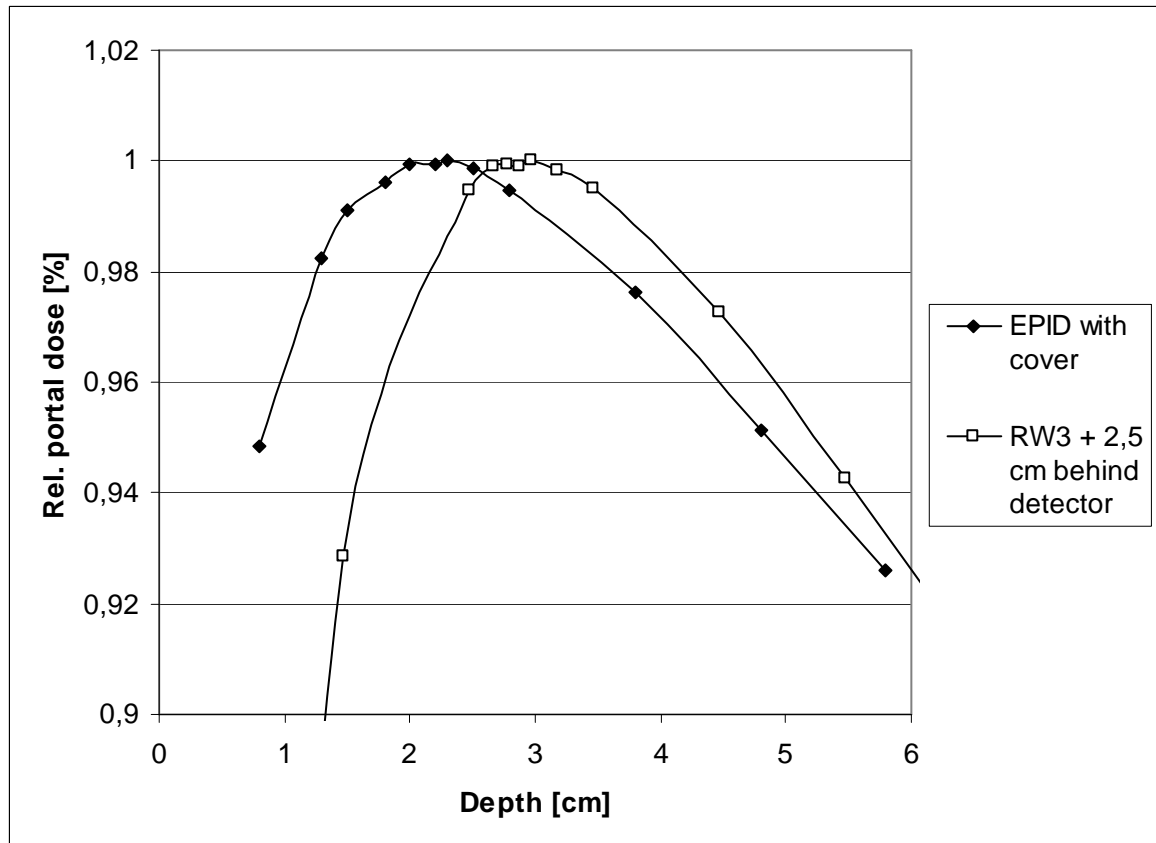
FIG. 76,   Relative depth dose curve of the EPID and the slab phantom at 15 MV

The plan was to verify the 0.8 cm of build-up material inside the detector, but the curve of the EPID shows the depth of maximum dose in shallower water than the slab-phantom. This is in agreement with van Esch et al. (2004). [30] Trials to "push" the maximum dose into deeper water by adding more water-equivalent material behind or by adding 2 mm of glass below the chamber (to simulate the glass substrate which holds the photodiodes) were not successful. The effect of backscattering at these high energies seems very small.

With photon energies of 6 MV it is not possible to show the whole depth dose curve, because the dose maximum depth is about 1.3 cm and so the measurement starts exactly at the peak of the curve.

But compared to Van Esch et al. (2004) the curves shown here have a much smaller plateau and show a shape that is much closer to a depth dose measured by a waterphantom. The reason for that lies probably in the fact that the aS1000 EPID is a newer device providing higher resolution than the as500 used by Van Esch (2004).

1.4   Ghosting

This picture shows a ghosting effect and was taken at a photon energy of 6 MV.
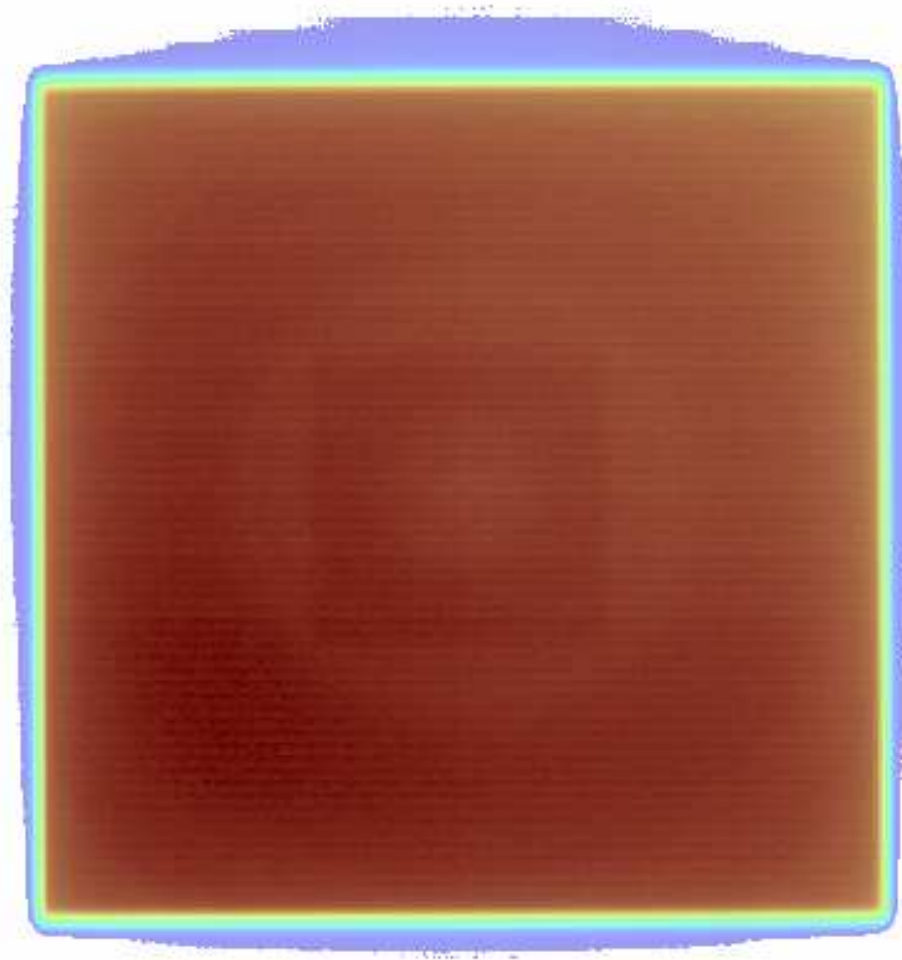
FIG. 77,   *Ghosting effect at 6 MV*

Unfortunately the effect can not be quantified in a line profile, because the effect is in the same magnitude as the noise in constant field but the quadratic shape in the middle can be seen by eye.

2   Comparison of IMRT test fields

2.1   Tests

All figures on the left hand side will represent the test pattern measured with the EPID and the images on the right hand side show the planned dose matrices resulting from the manually created fluence patterns. These two pictures show the dose distributions in colour-wash, where the colours represent the deposited doses. Below these two pictures there is the result of the gamma evaluation shown as an image, where the red pixels indicate areas where the criteria of 3 %/3 mm are not fulfilled. Each gamma evaluation considered 84100 dose points within a real fieldsize of 14.5 x 14.5 cm^2 at an SDD of 145 cm.

2.1.1   Test1: 4 vertical stripes with increasing relative fluencies
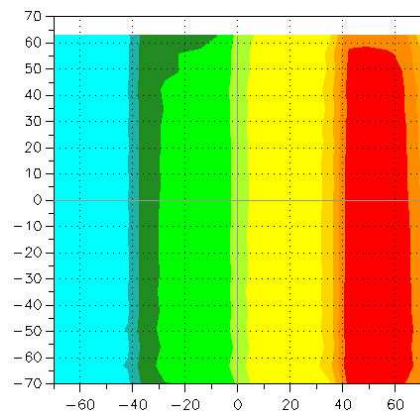
FIG. 78,   Test pattern: test1 measured   FIG. 79,   Test pattern: test1 planned
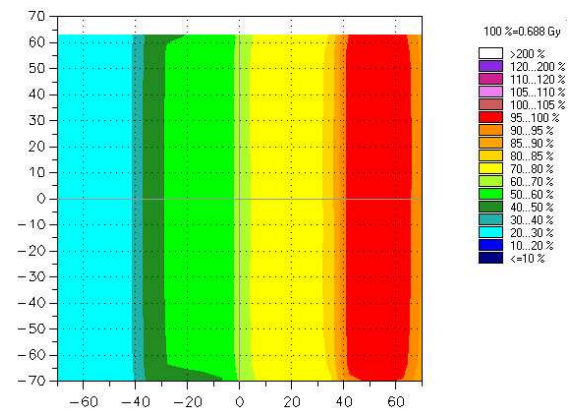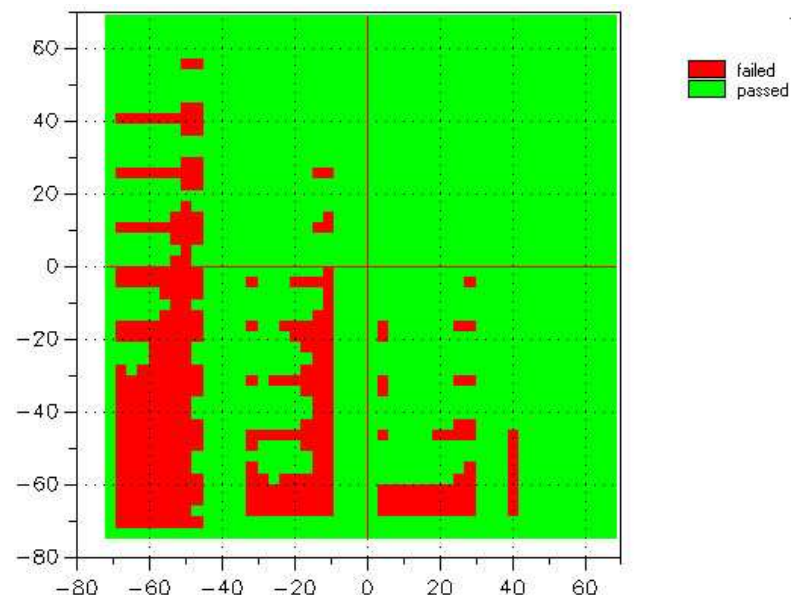
FIG. 80,   Gamma evaluation of test pattern test1

64205 of 84100 of all dose points were evaluated as positive, which means with a gamma factor below or equal one → 76.34 % of all pixels passed the gamma evaluation. The red areas in the picture consist mainly of interleaf leakage, which is not simulated properly during planning procedure, and are therefore not visible in the reference image. The lower left corner of the picture shows a red area, which can also be seen in homogenous fields and seems to occur in a specific area of the EPID. It is not clear why the flood field correction does not compensate for that during calibration. Further measurements would be necessary to verify that effect.

2.1.2   Test2: triangles
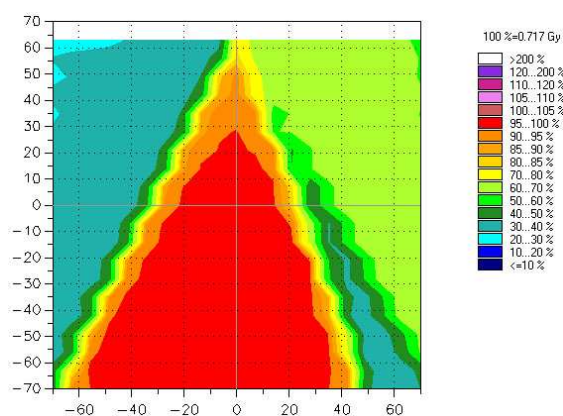
FIG. 81,   Test pattern: test2 measured
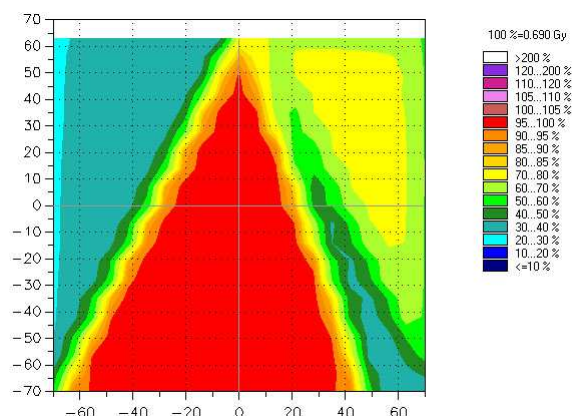
FIG. 82,   Test pattern: test2 planned
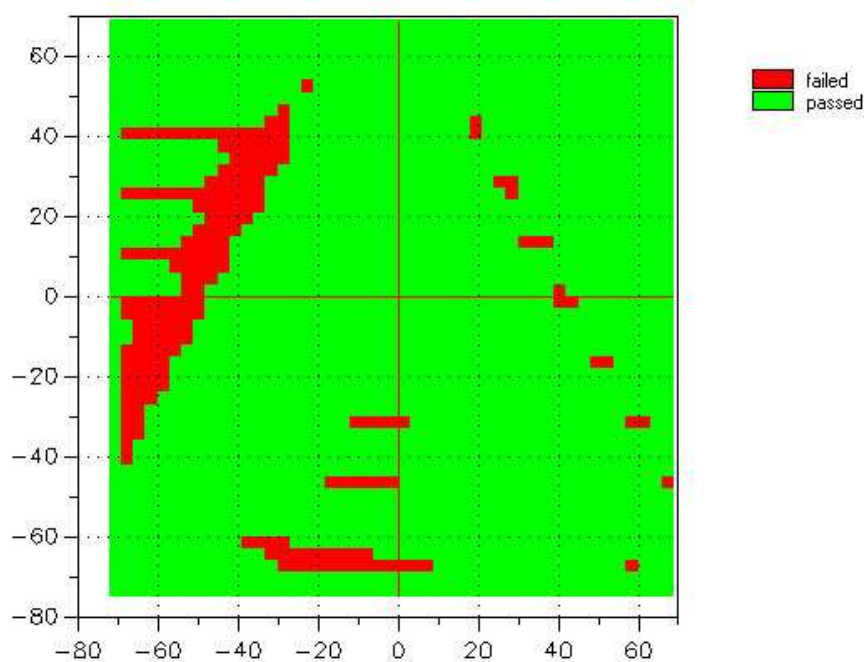
FIG. 83,   Gamma evaluation of test pattern test2

70744 of 84100 of all dose points were evaluated as positive, which means with a gamma factor below or equal one → 84.12 % of all pixels passed the gamma evaluation. Deviations between measured and planned dose patterns are a result of interleaf leakage, the red horizontal lines indicate the edges of the MLC leafs.

2.1.3   Test3: fluence gradient in horizontal direction
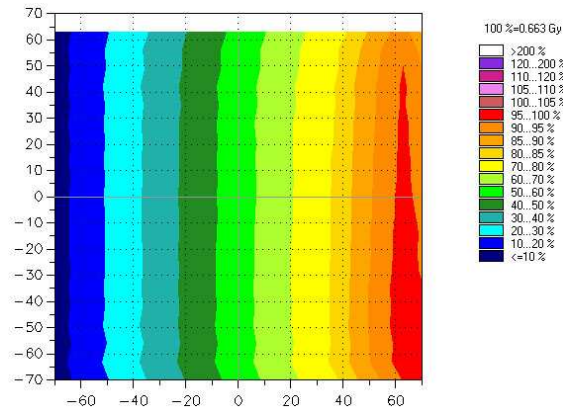
FIG. 84,   Test pattern: test3 measured
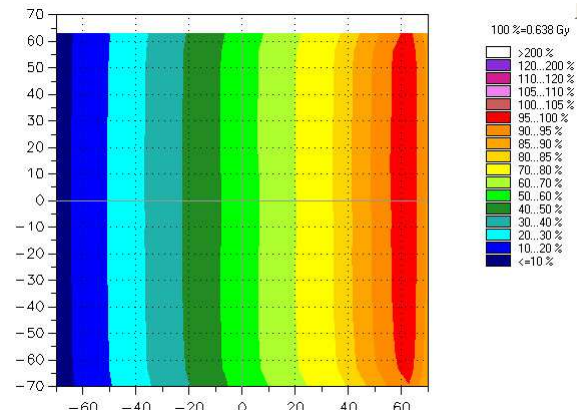
FIG. 85,   Test pattern: test3 planned
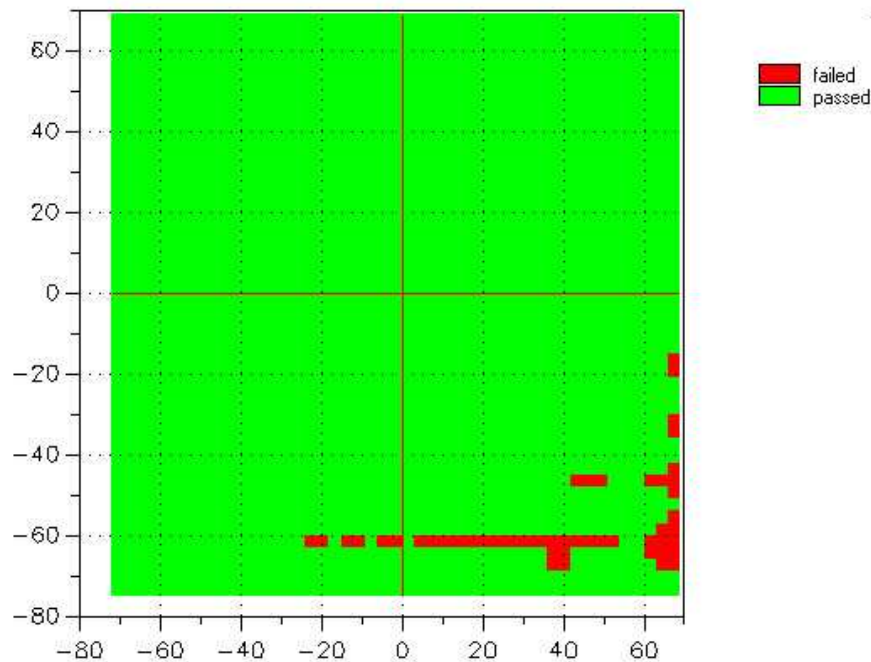
FIG. 86,   Gamma evaluation of test pattern test3

74760 of 84100 of all dose points were evaluated as positive, which means with a gamma factor below or equal one → 88.89 % of all pixels passed the gamma evaluation. The gamma evaluation shows a very good result, except for some interleaf leakage.

2.1.4 Test4: 10 vertical stripes
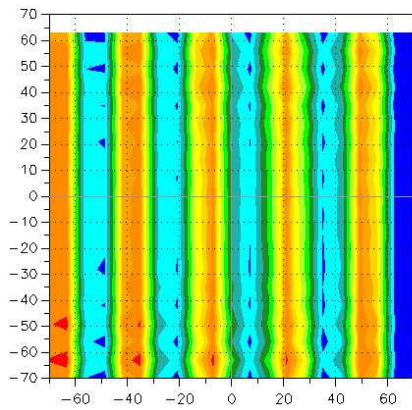
FIG. 87, Test pattern: test4 measured
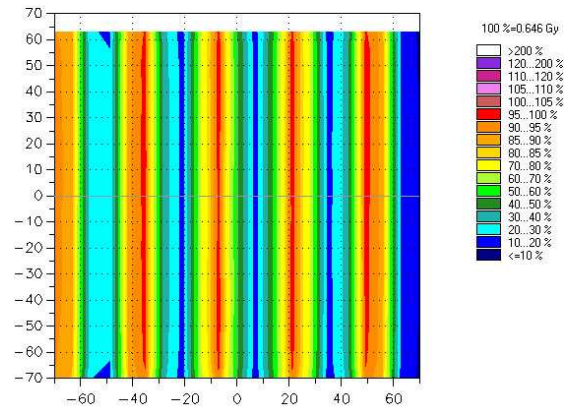
FIG. 88, Test pattern: test4 planned
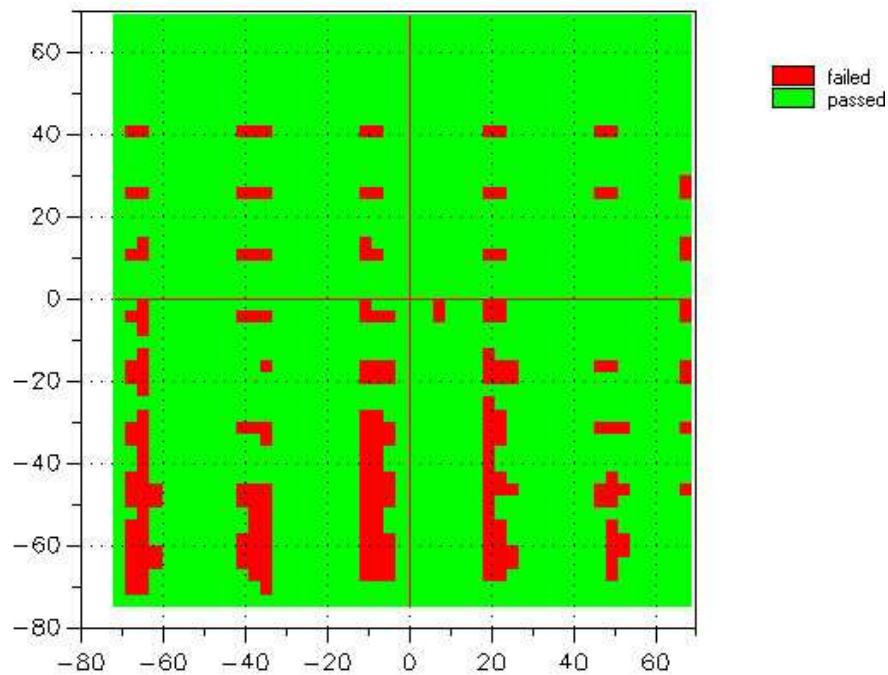
FIG. 89, Gamma evaluation of test pattern test4

65263 of 84100 of all dose points were evaluated as positive, which means with a gamma factor below or equal one → 77.60 % of all pixels passed the gamma evaluation. The MLC movement starts to deviate from the simulated MLC-motion in areas of high gradients because of limitations in movement velocity. In areas, where this hardware related phenomenon adds up with interleaf leakage, the criterion 3 %/3 mm can not be met.

2.1.5 Test5: 20 vertical stripes
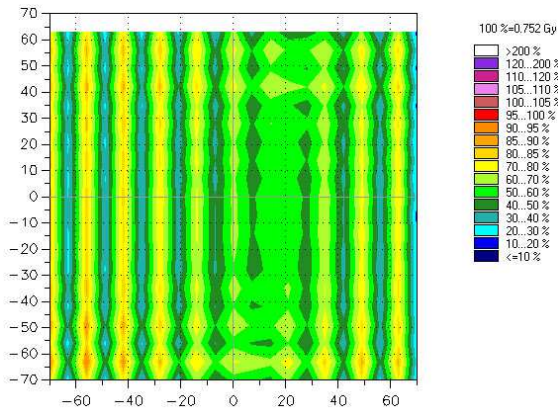
FIG. 90, Test pattern: test5 measured
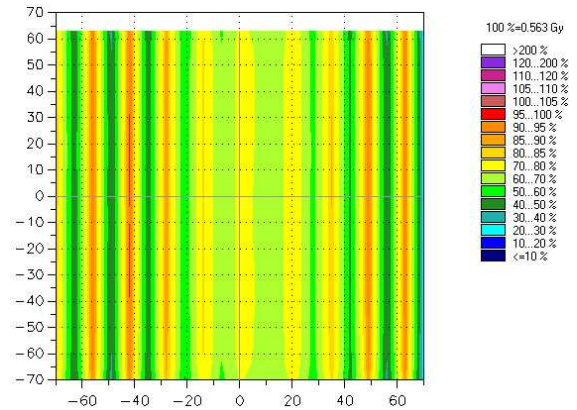
FIG. 91, Test pattern: test5 planned
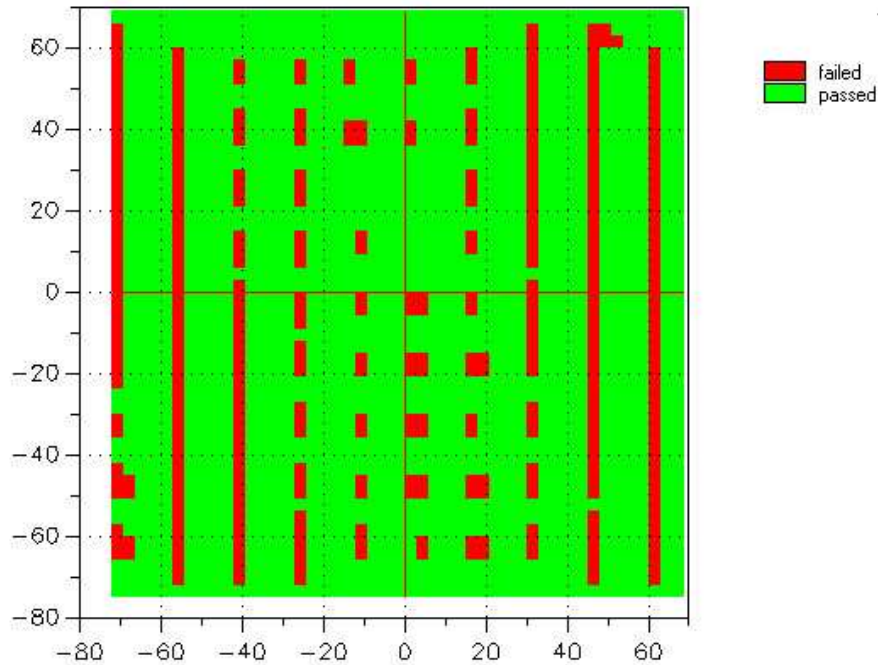
FIG. 92, Gamma evaluation of test pattern test5

55676 of 84100 of all dose points were evaluated as positive, which means with a gamma factor below or equal one → 66.20 % of all pixels passed the gamma evaluation.

The high spatial resolution in the dose distribution cannot be satisfyingly modelled by the MLC movement.

2.1.6   Test6: 14 vertical stripes, separated by a horizontal line and shifted
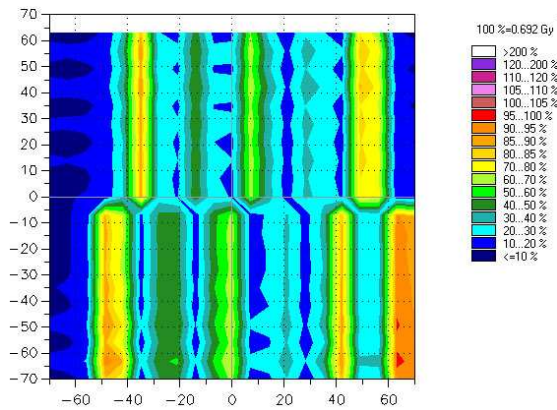
FIG. 93,   *Test pattern: test6 measured*
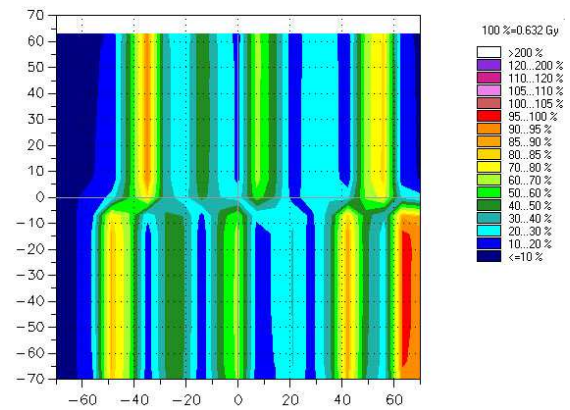
FIG. 94,   *Test pattern: test6 planned*
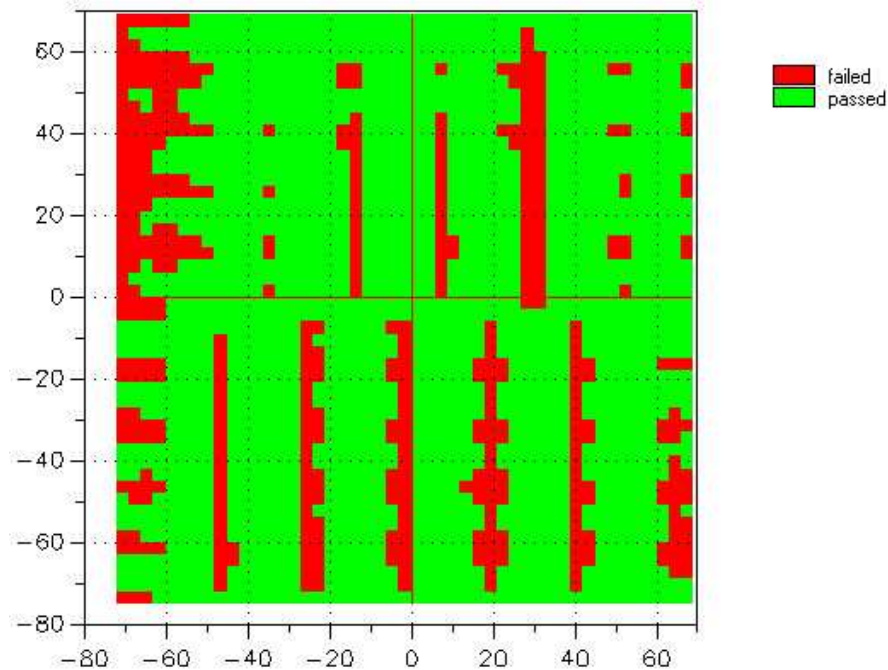
FIG. 95,   *Gamma evaluation of test pattern test6*

57597 of 84100 of all dose points were evaluated as positive, which means with a gamma factor below or equal one → 68.37 % of all pixels passed the gamma evaluation. Test6 is like test5 of high complexity, where the MLC is not properly simulated by the planning program. Real IMRT fields for treatment would most likely not include high gradient areas like this test pattern.

2.1.7   Test7: three vertical stripes with different relative fluencies
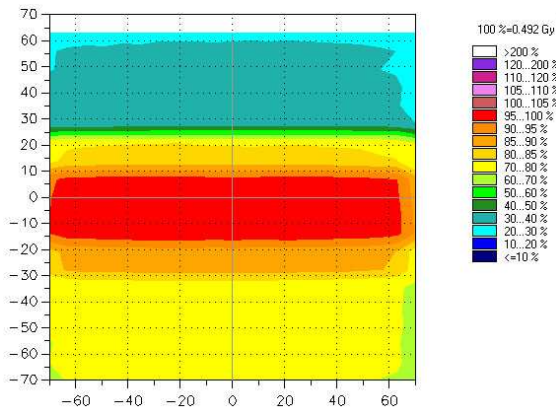
FIG. 96,   *Test pattern: test7 measured*
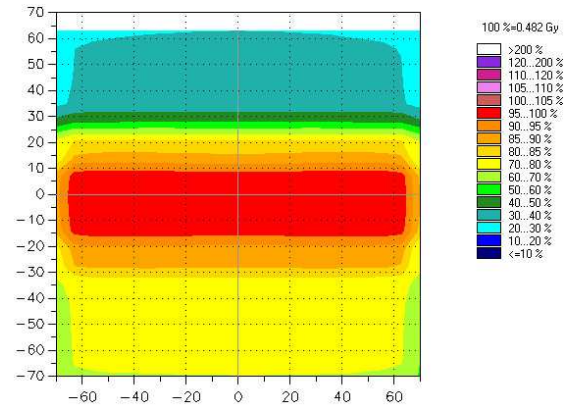
FIG. 97,   *Test pattern: test7 planned*
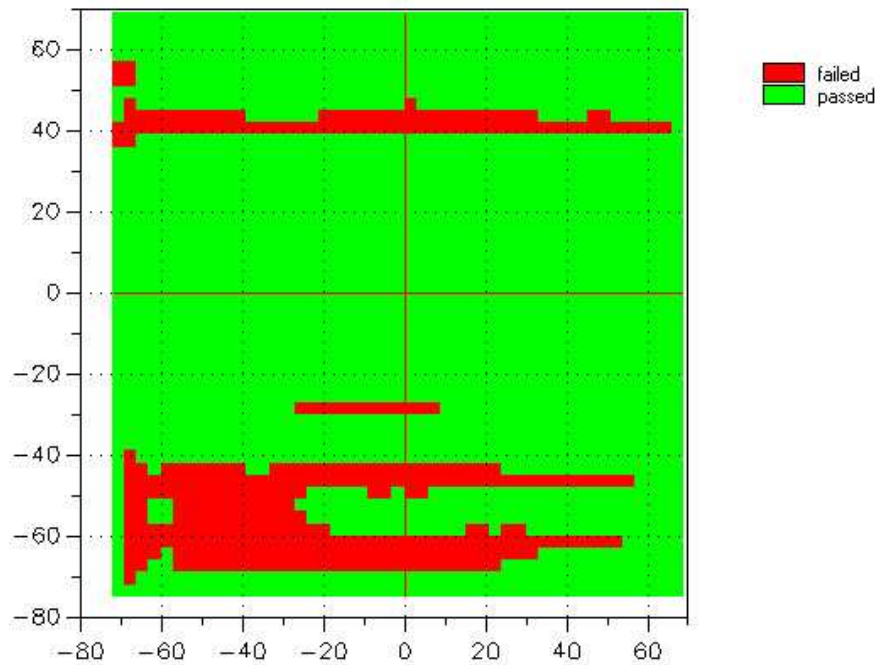
FIG. 98,   *Gamma evaluation of test pattern test7*

63324 of 84100 of all dose points were evaluated as positive, which means with a gamma factor below or equal one → 75.30 % of all pixels passed the gamma evaluation. This test pattern shows a discrepancy between the designed dose distribution and the planned one. The horizontal "dose edges" could not be realized during planning, because the edge is not in the same place as the MLC leaf's edge and can not be properly modelled by MLC movement.

2.2   Comparison between Varian aS1000 EPID and PTW 729 array

Representative for all other test-measurements the result of test4 is shown here. The red lines show the profiles of the planned matrices, the green dots mark the locations of the ionization chambers and the blue line is the profile of the EPID-measurement.
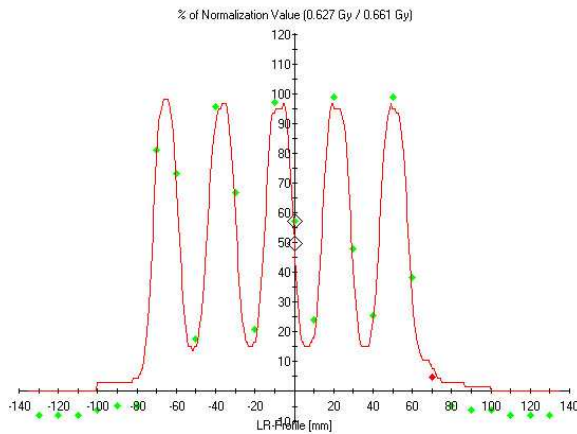
FIG. 99,   Line profile in array-measurement (test4)
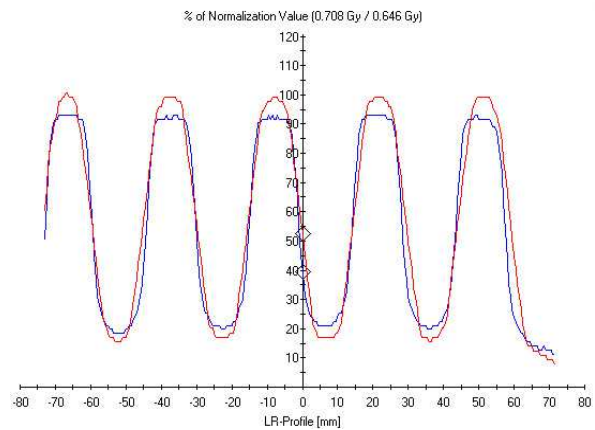
FIG. 100,   Line profile in EPID-measurement (test4)

Even though the results of the gamma evaluation for the array measurement is quantitatively better (90.32 % of all evaluated dose points passed) compared to the EPID-measurement (77.6 % of all evaluated dose points passed) it is obvious that the result of the array-measurement is not reliable. Areas of $1 \times 1 \, cm^2$ are unconsidered in the evaluation. While in the array-measurement only 217 dose points were evaluated, the EPID result offers 84100 dose points for evaluation.

2.3   Verification of real patients' IMRT plans

Almost all deviations between measured and planned dose patterns are either due to interleaf leakage or due to scattered radiation outside the planned field.

2.3.1   Treatment plan: patient 1 H&N

TAB. 8,   Results of plan verification for patient 1

	evaluated dose points	passed dose points	failed dose points			
field 1	63624	54636	8988	→	**85.87 %**	**passed**
field 2	58650	49186	9464	→	**83.86 %**	**passed**
field 3	65750	59844	5906	→	**91.02 %**	**passed**
field 4	66234	58754	7480	→	**88.71 %**	**passed**
field 5	63624	54636	8988	→	**85.87 %**	**passed**

2.3.1.1   <u>Field 1</u>
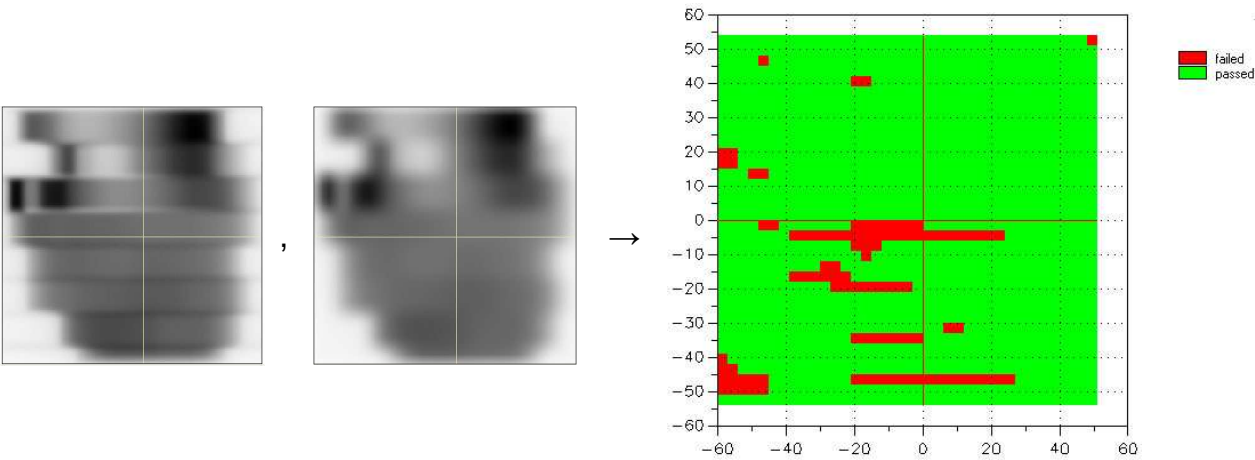
FIG. 101,   Patient 1, field 1: measured matrix, planned matrix → gamma evaluation
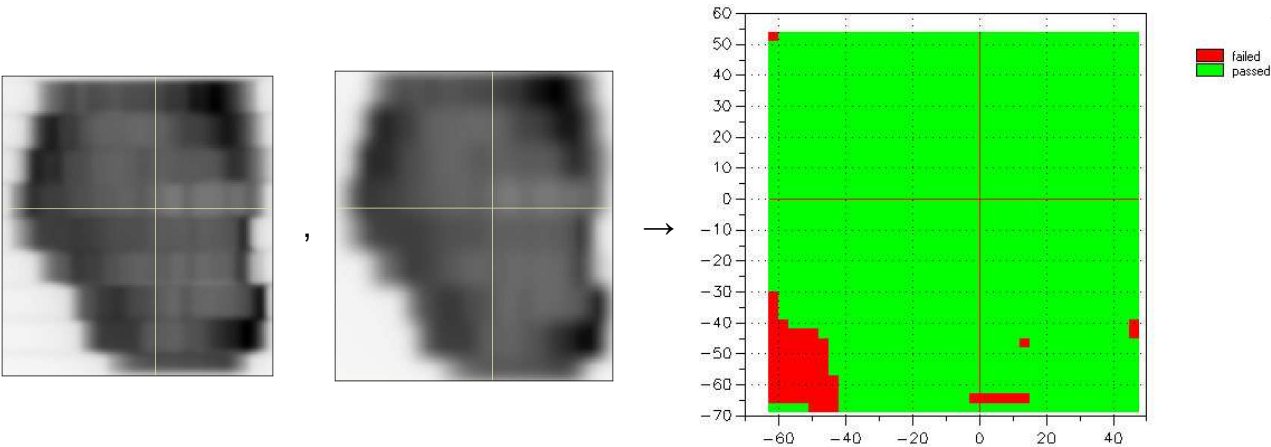
2.3.1.2   <u>Field 2</u>
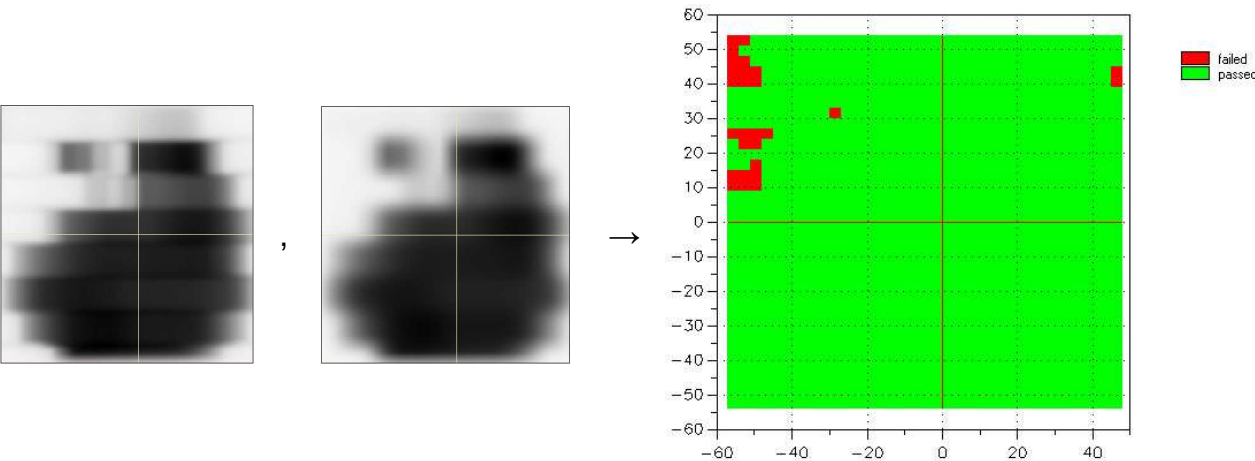
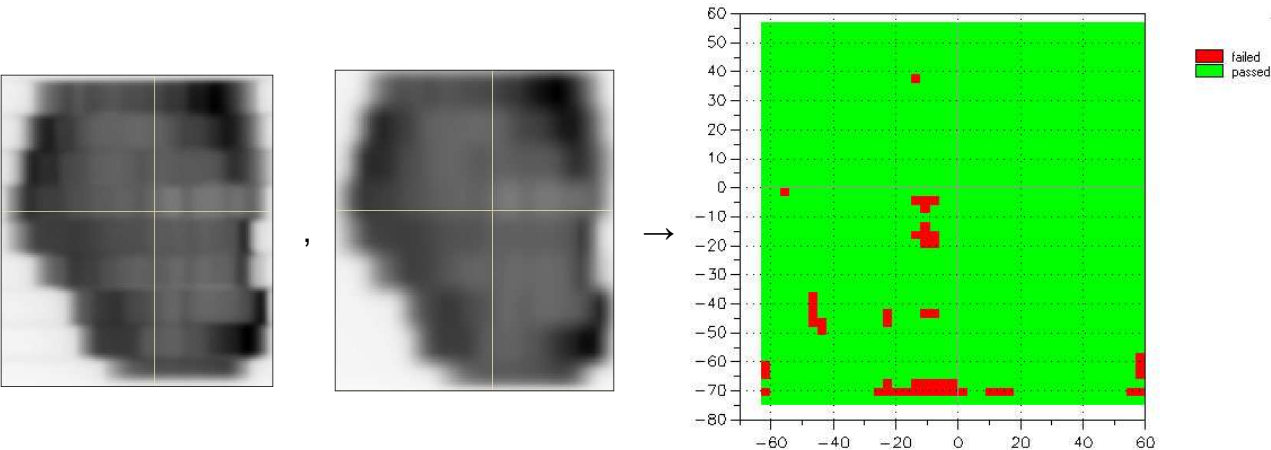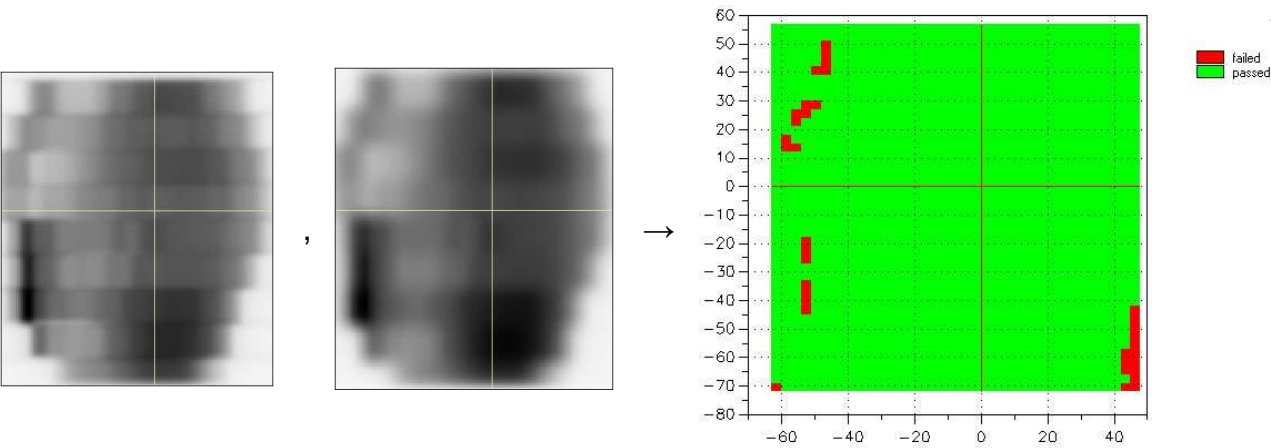*FIG. 102,   Patient 1, field 2: measured matrix, planned matrix → gamma evaluation*

2.3.1.3   Field 3
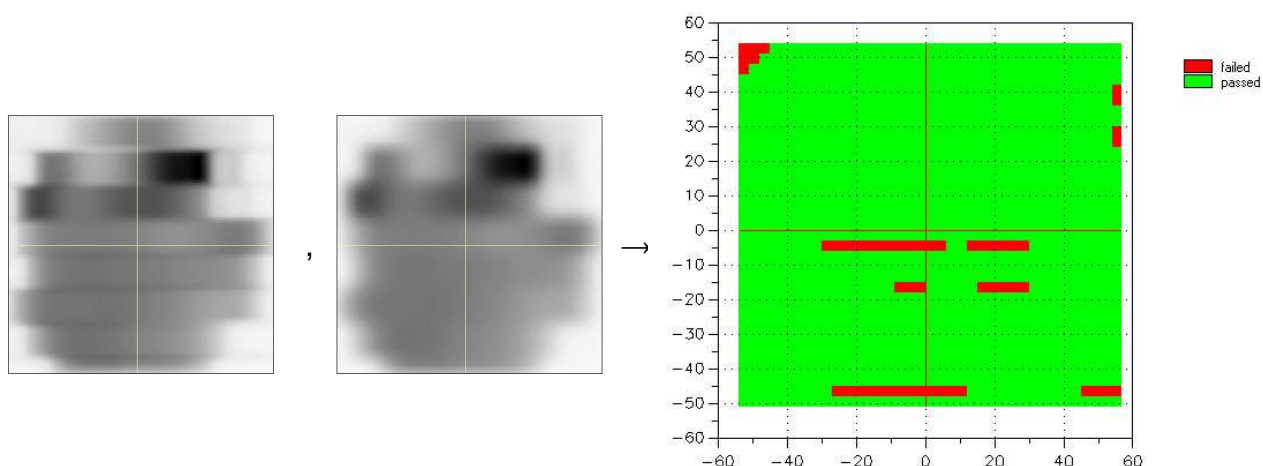
FIG. 103,   Patient 1, field 3: measured matrix, planned matrix → gamma evaluation

2.3.1.4   Field 4
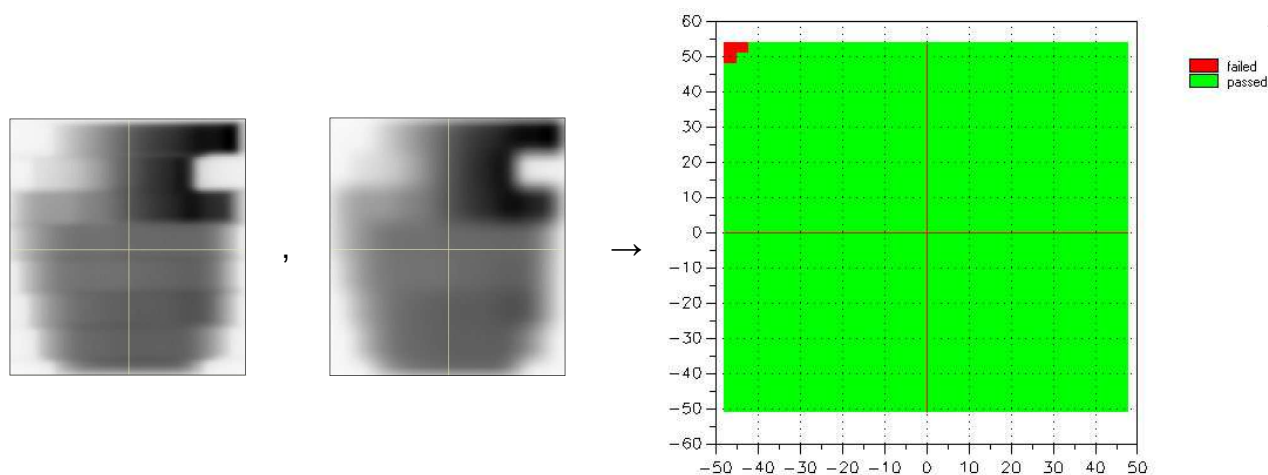
FIG. 104,   Patient 1, field 4: measured matrix, planned matrix → gamma evaluation
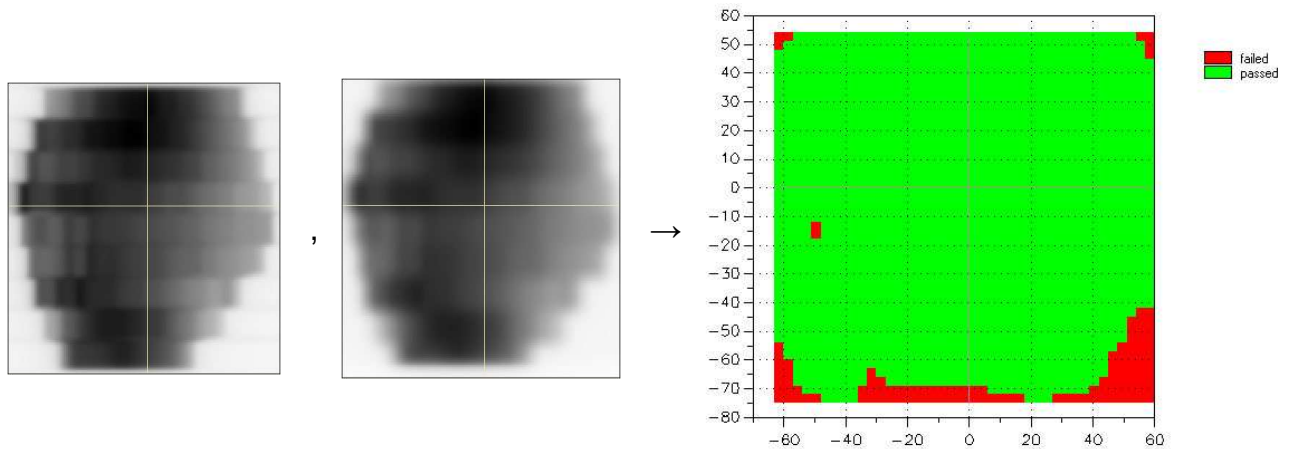
2.3.1.5   Field 5
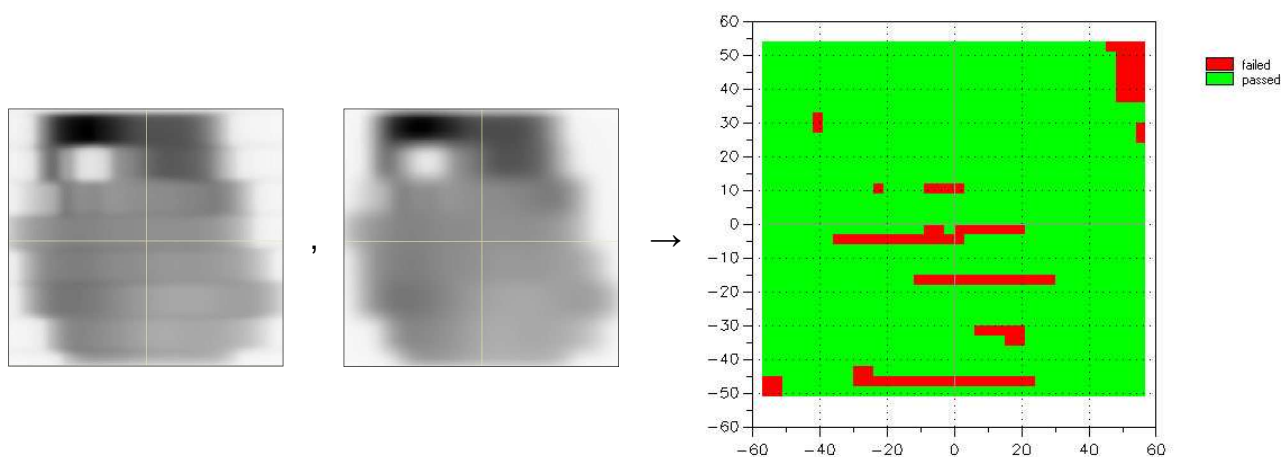
FIG. 105,   Patient 1, field 5: measured matrix, planned matrix → gamma evaluation

2.3.2   Treatment plan: patient 2 H&N

TAB. 9,   Results of plan verification for patient 2

	evaluated dose points	passed dose points	failed dose points			
field 1	34026	30057	3969	→	**88.34 %**	**passed**
field 2	39544	34952	4592	→	**88.39 %**	**passed**
field 3	49226	42503	6723	→	**86.34 %**	**passed**
field 4	61482	54130	7352	→	**88.04 %**	**passed**

2.3.2.1   Field 1
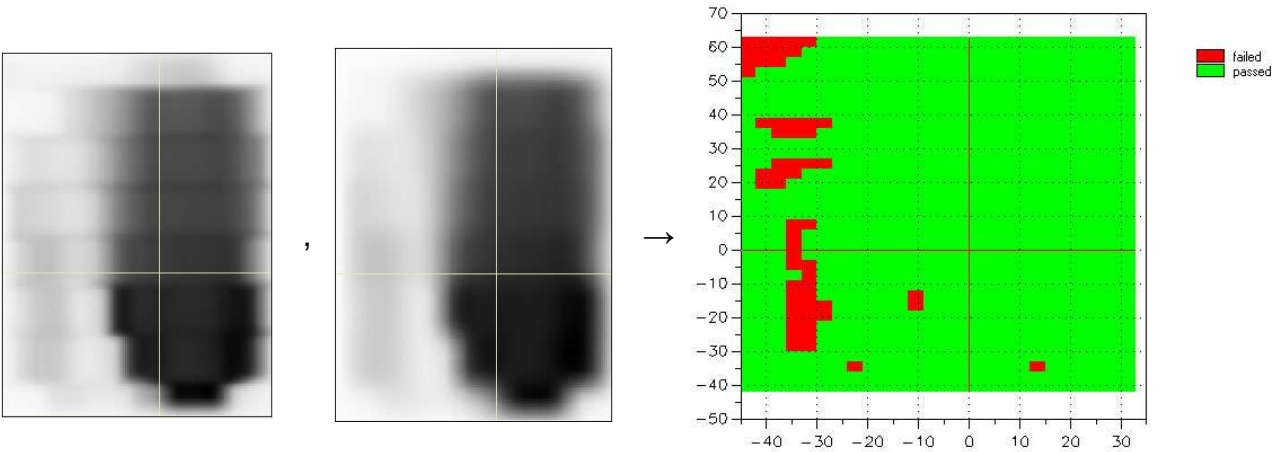
FIG. 106,   Patient 2, field 1: measured matrix, planned matrix → gamma evaluation
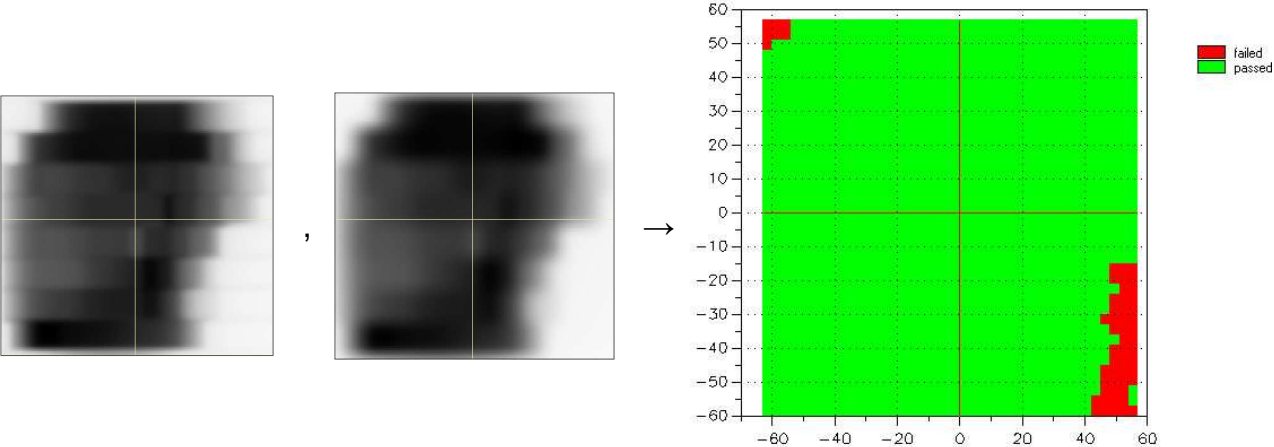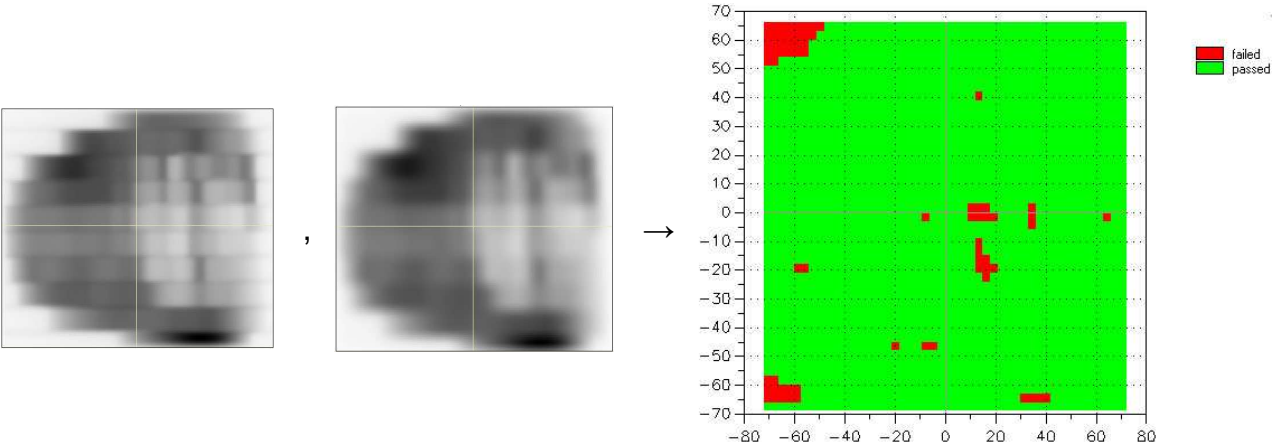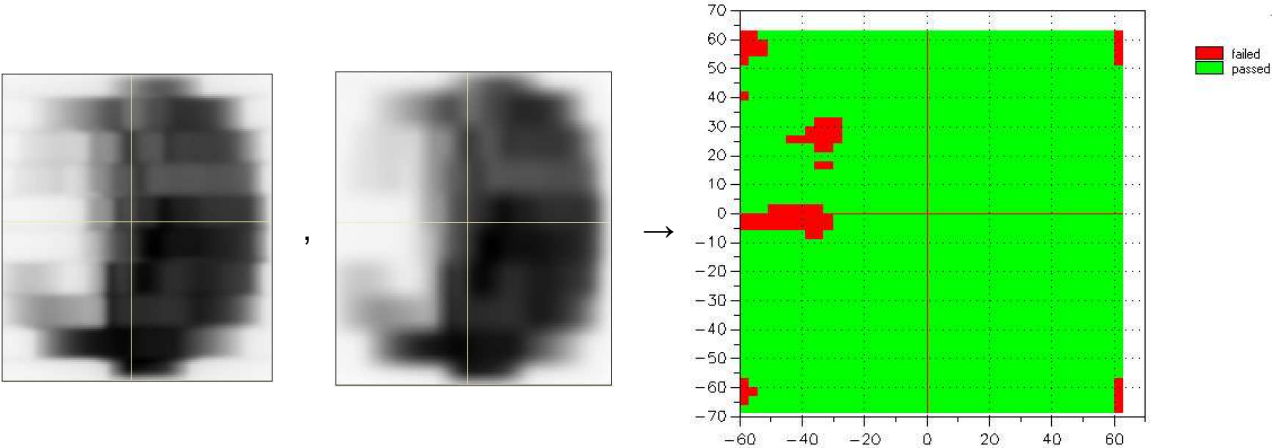
2.3.2.2   Field 2
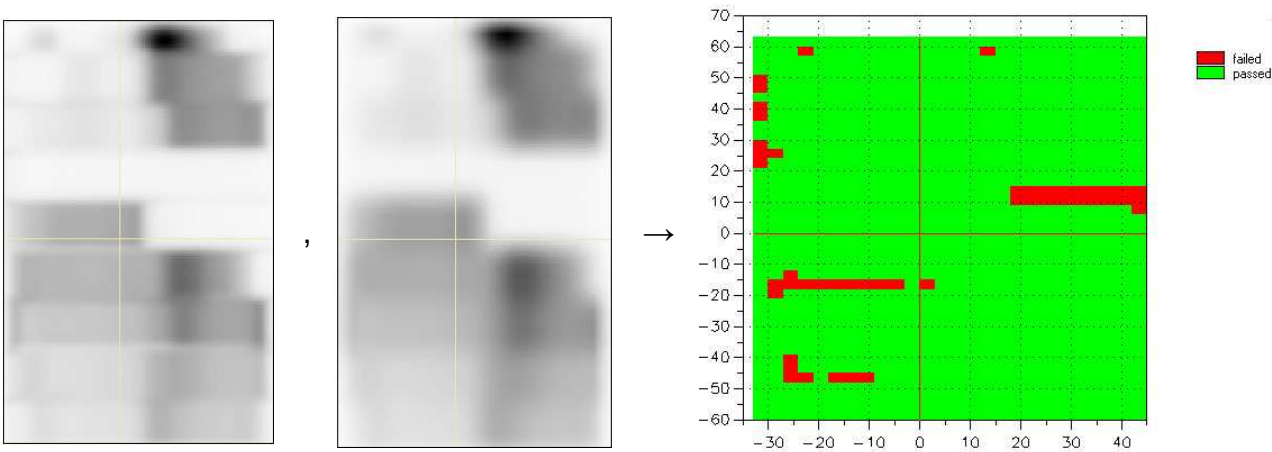
FIG. 107,   Patient 2, field 2: measured matrix, planned matrix → gamma evaluation

2.3.2.3 Field 3
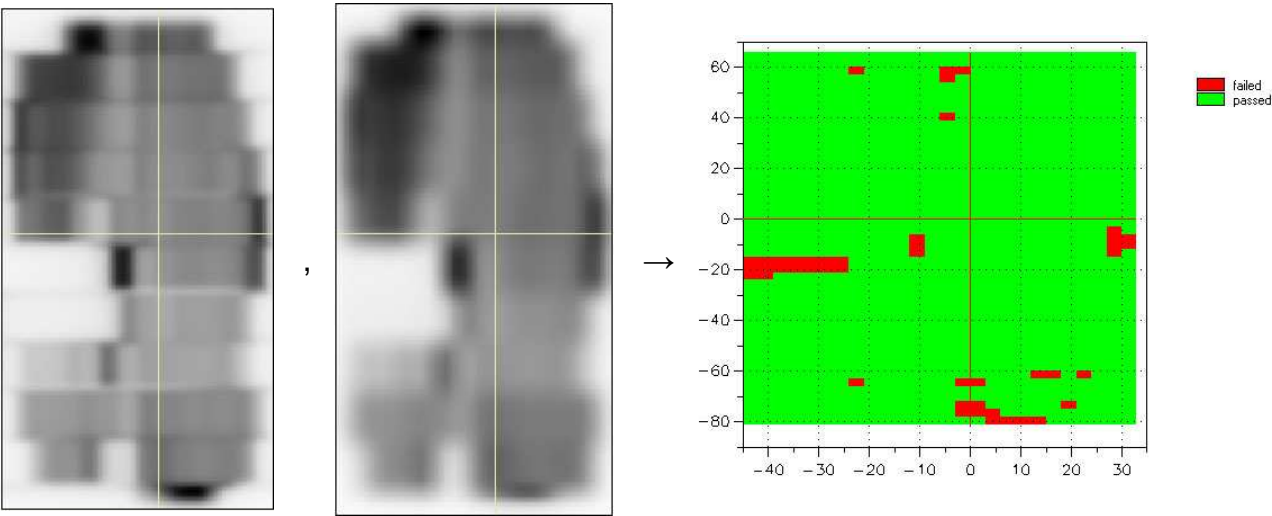
FIG. 108,   *Patient 2, field 3: measured matrix, planned matrix → gamma evaluation*

2.3.2.4 Field 4
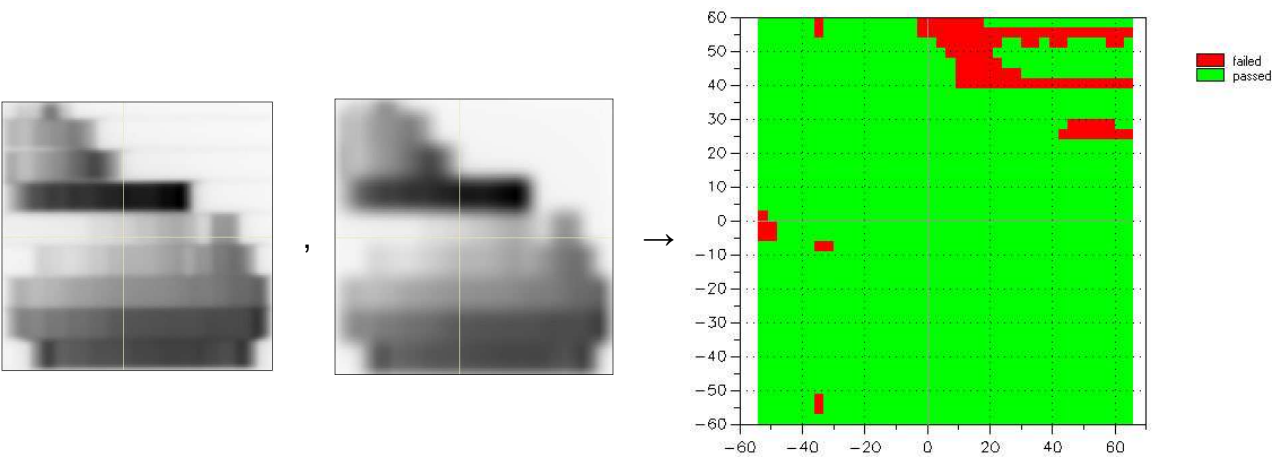
FIG. 109,   *Patient 2, field 4: measured matrix, planned matrix → gamma evaluation*

2.3.3 Treatment plan: patient 3 H&N

TAB. 10,   *Results of plan verification for patient 3*

	evaluated dose points	passed dose points	failed dose points			
field 1	21423	19432	1991	→	**90.71 %**	**passed**
field 2	23701	22148	1553	→	**93.45 %**	**passed**
field 3	22605	21002	1603	→	**92.91 %**	**passed**
field 4	21066	19152	1914	→	**90.91 %**	**passed**

2.3.3.1   Field 1
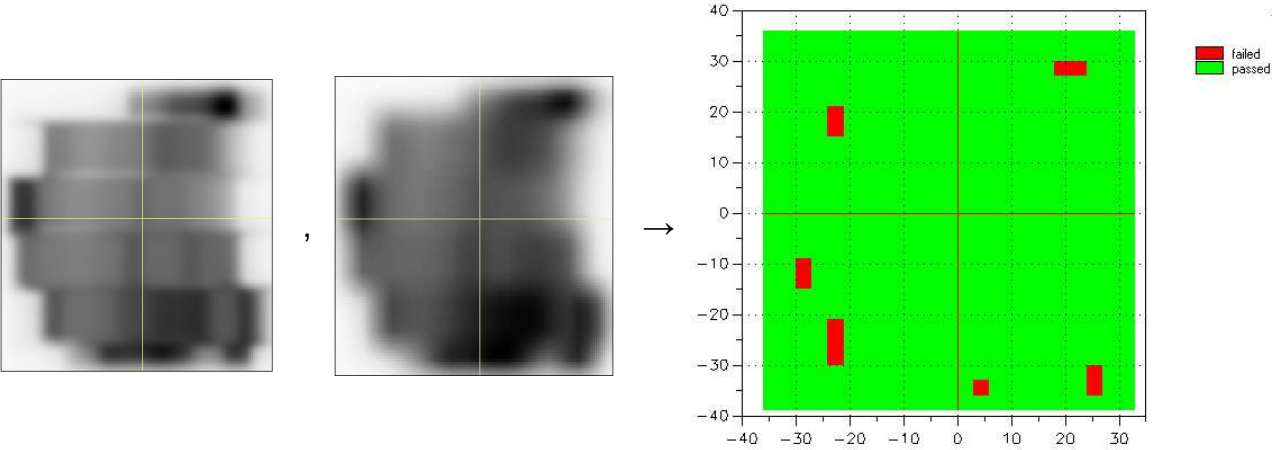
FIG. 110,   *Patient 3, field 1: measured matrix, planned matrix → gamma evaluation*

2.3.3.2   Field 2
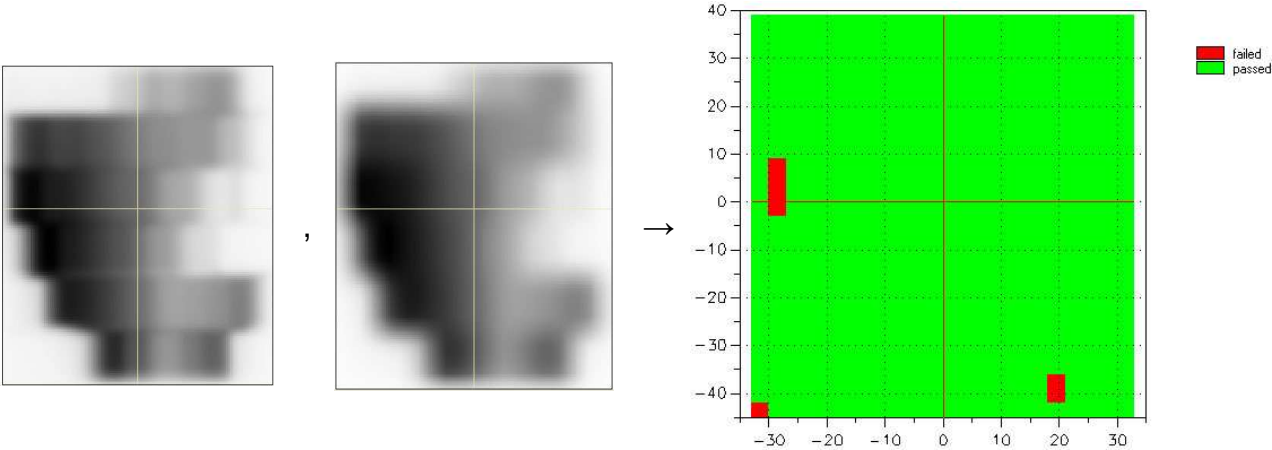
FIG. 111,   *Patient 3, field 2: measured matrix, planned matrix → gamma evaluation*

2.3.3.3   Field 3
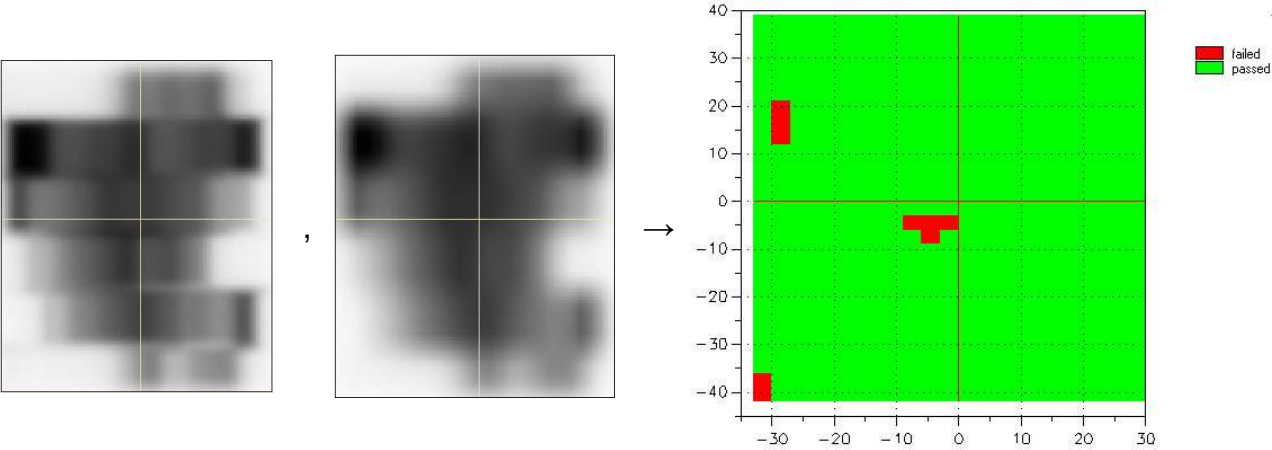
FIG. 112,   *Patient 3, field 3: measured matrix, planned matrix → gamma evaluation*

2.3.3.4   Field 4
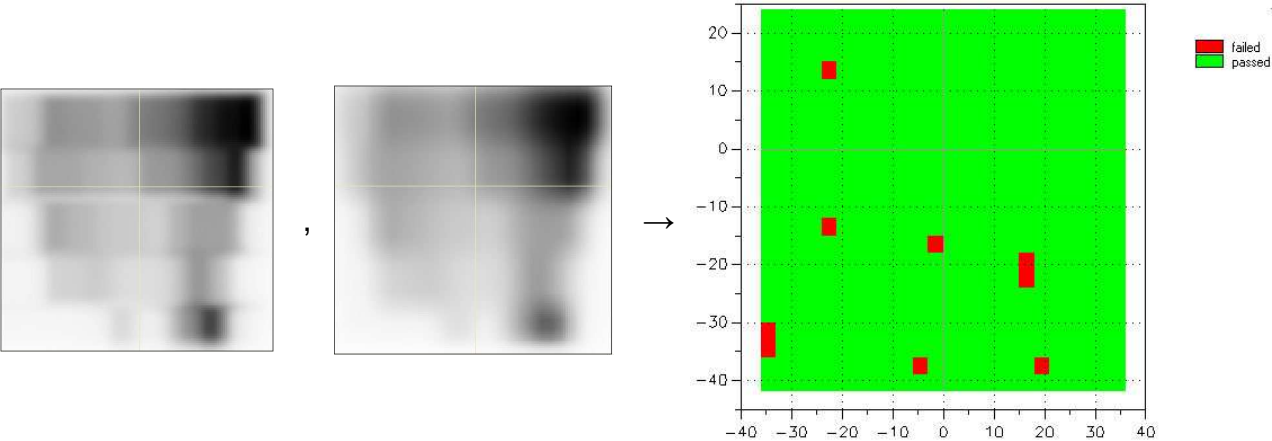
FIG. 113,   Patient 3, field 4: measured matrix, planned matrix → gamma evaluation

2.3.4   Treatment plan: patient 4 prostate

TAB. 11,   Results of plan verification for patient 4

	evaluated dose points	passed dose points	failed dose points			
field 1	54036	48496	5540	→	**89.75 %**	**passed**
field 2	57828	54464	3364	→	**94.18 %**	**passed**
field 3	60435	54961	5474	→	**90.94 %**	**passed**
field 4	58065	54421	3644	→	**93.72 %**	**passed**
field 5	57112	52063	5049	→	**91.16 %**	**passed**

2.3.4.1   Field 1
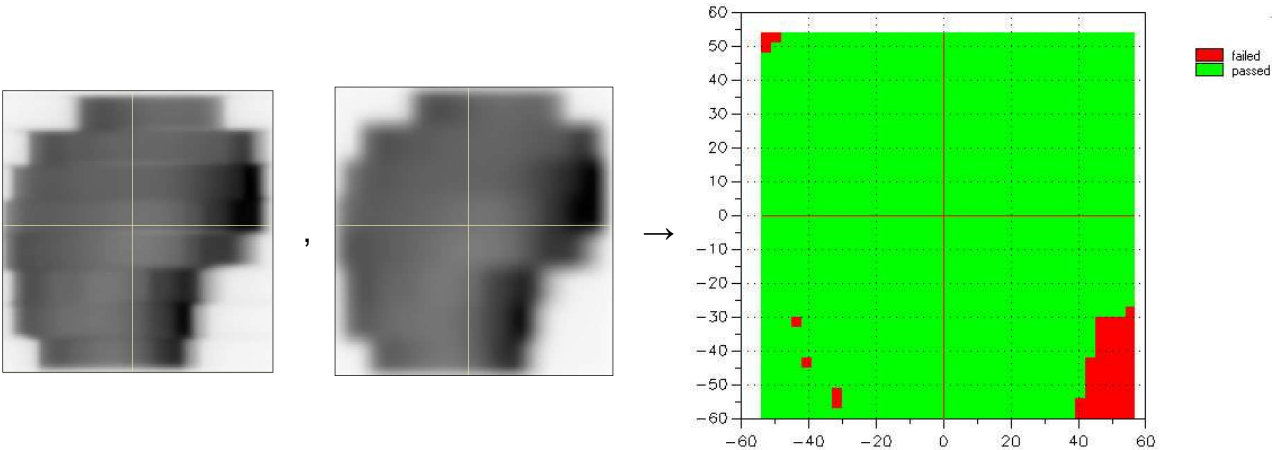
FIG. 114,   Patient 4, field 1: measured matrix, planned matrix → gamma evaluation

2.3.4.2 Field 2
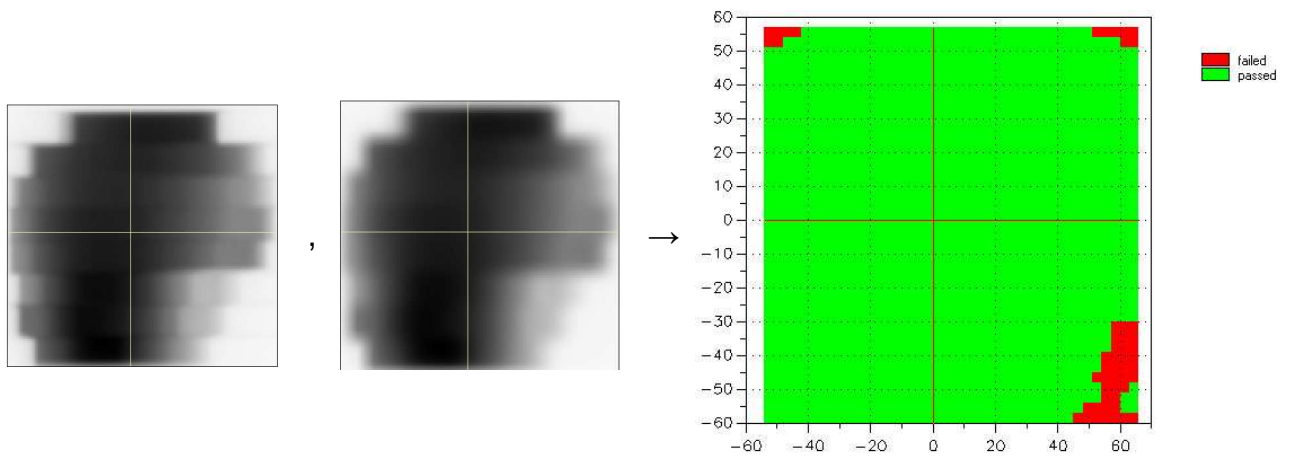
FIG. 115, *Patient 4, field 2: measured matrix, planned matrix → gamma evaluation*

2.3.4.3 Field 3
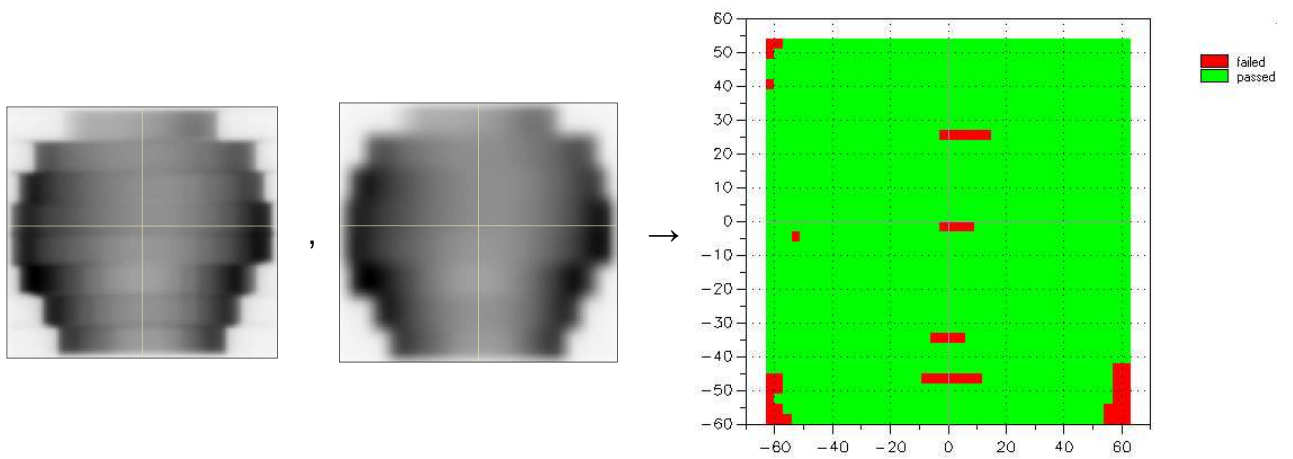
FIG. 116, *Patient 4, field 3: measured matrix, planned matrix → gamma evaluation*

2.3.4.4 Field 4
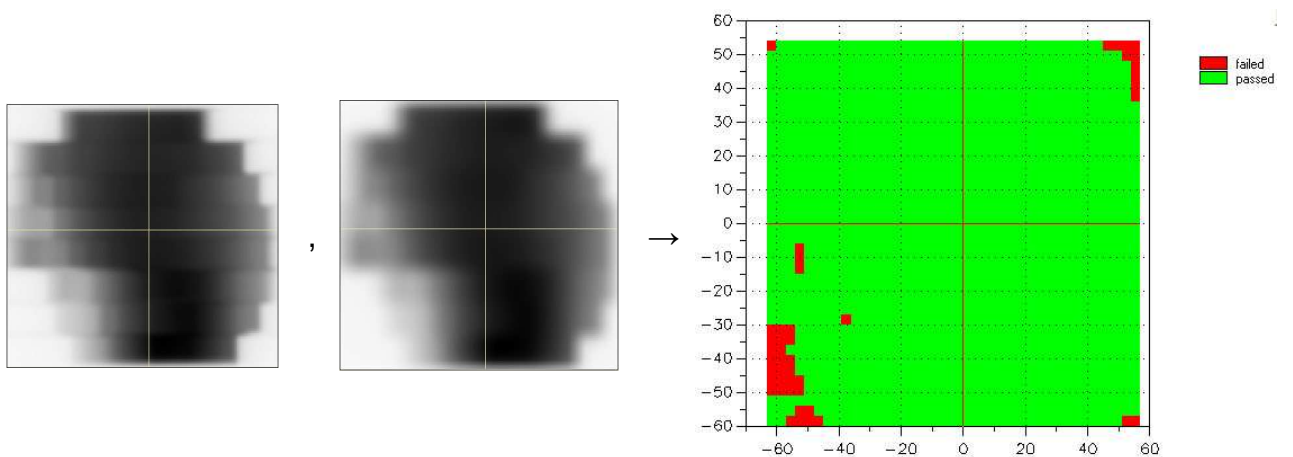
FIG. 117, *Patient 4, field 4: measured matrix, planned matrix → gamma evaluation*

2.3.4.5   Field 5
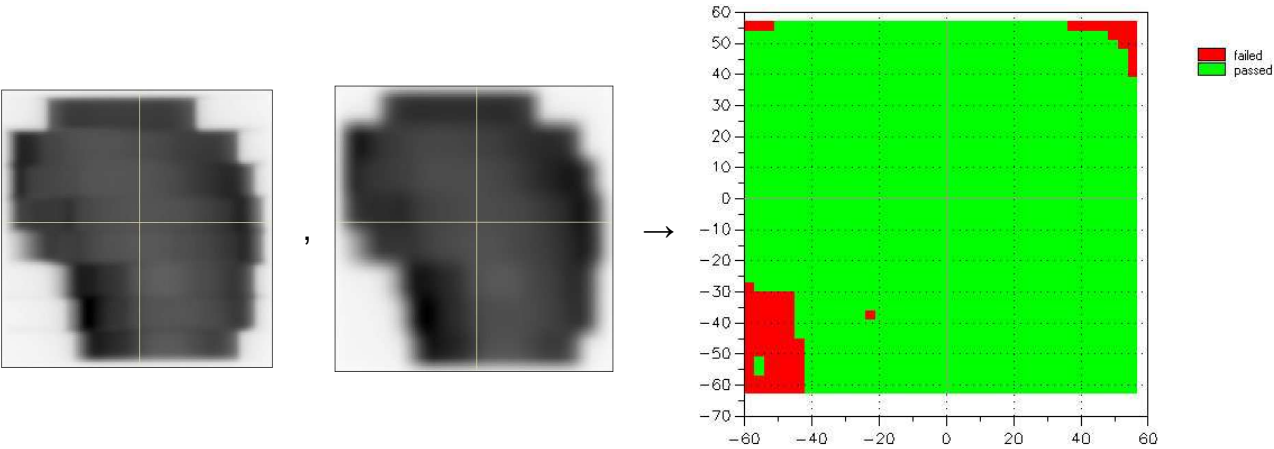
FIG. 118,   *Patient 4, field 5: measured matrix, planned matrix → gamma evaluation*

2.3.5   Treatment plan: patient 5 prostate

TAB. 12,   *Results of plan verification for patient 5*

	evaluated dose points	passed dose points	failed dose points			
field 1	63624	54636	8988	→	**85.87 %**	**passed**
field 2	58650	49186	9464	→	**83.86 %**	**passed**
field 3	65750	59844	5906	→	**91.02 %**	**passed**
field 4	58986	54911	4075	→	**93.09 %**	**passed**
field 5	66234	58754	7480	→	**88.71 %**	**passed**

2.3.5.1   Field 1
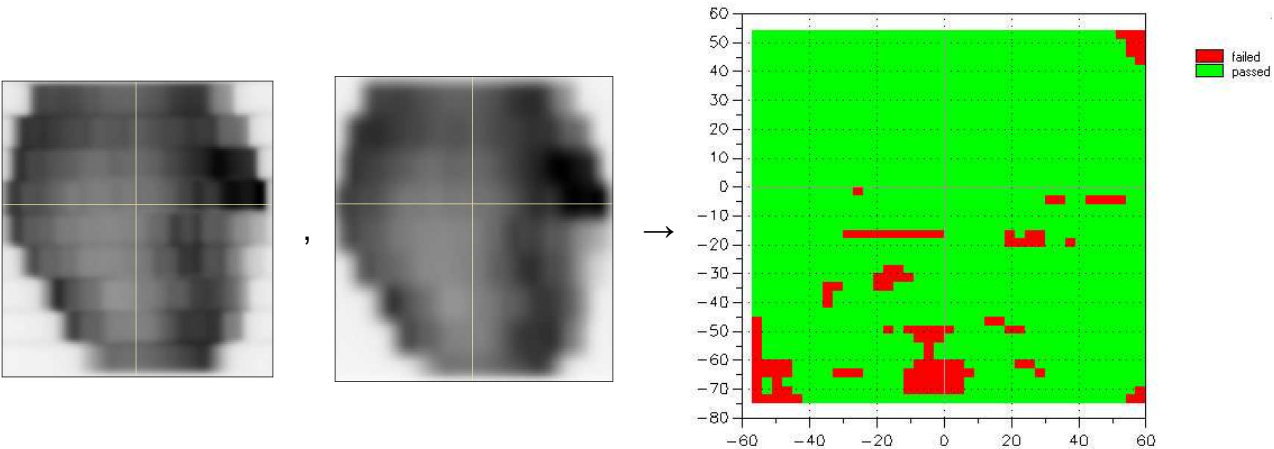
FIG. 119,   *Patient 5, field 1: measured matrix, planned matrix → gamma evaluation*

2.3.5.2   Field 2

FIG. 120,   *Patient 5, field 2: measured matrix, planned matrix → gamma evaluation*

2.3.5.3   Field 3

FIG. 121,   *Patient 5, field 3: measured matrix, planned matrix → gamma evaluation*

2.3.5.4   Field 4

FIG. 122,   *Patient 5, field 4: measured matrix, planned matrix → gamma evaluation*

2.3.5.5 Field 5

FIG. 123,   *Patient 5, field 5: measured matrix, planned matrix → gamma evaluation*

2.3.6   Treatment plan: patient 6 prostate

TAB. 13,   *Results of plan verification for patient 6*

	evaluated dose points	passed dose points	failed dose points			
field 1	69048	65960	3088	→	**95.53 %**	**passed**
field 2	59290	54871	4419	→	**92.55 %**	**passed**
field 3	82566	75412	7154	→	**91.34 %**	**passed**
field 4	70963	65921	5042	→	**92.89 %**	**passed**
field 5	73396	65711	7685	→	**89.53 %**	**passed**
field 6	59961	52790	7171	→	**88.04 %**	**passed**

2.3.6.1 Field 1
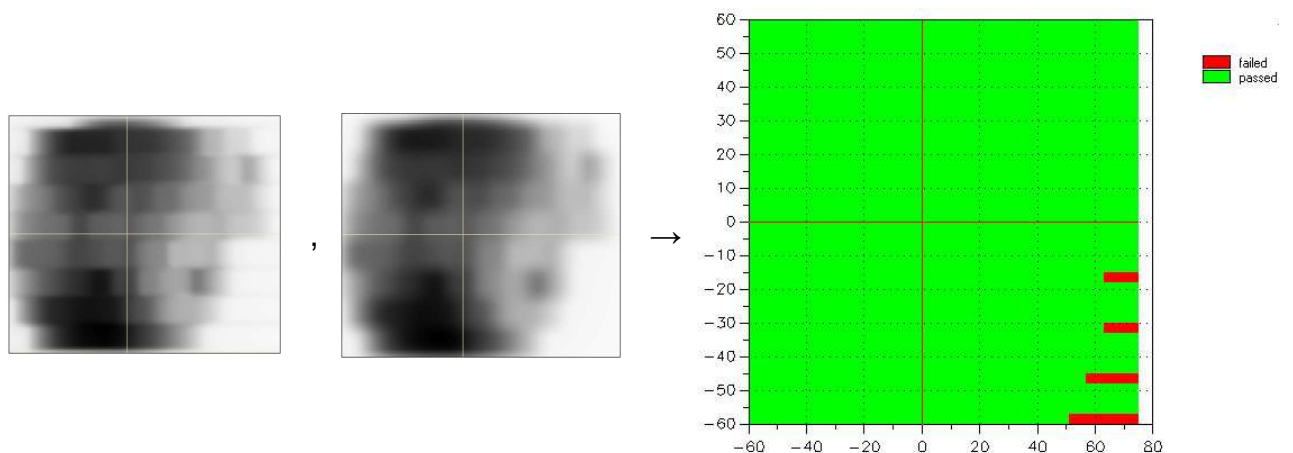
FIG. 124,   *Patient 6, field 1: measured matrix, planned matrix → gamma evaluation*

2.3.6.2   <u>Field 2</u>

FIG. 125,   *Patient 6, field 2: measured matrix, planned matrix → gamma evaluation*

2.3.6.3   <u>Field 3</u>

FIG. 126,   *Patient 6, field 3: measured matrix, planned matrix → gamma evaluation*

2.3.6.4   <u>Field 4</u>

FIG. 127,   *Patient 6, field 4: measured matrix, planned matrix → gamma evaluation*

2.3.6.5   Field 5
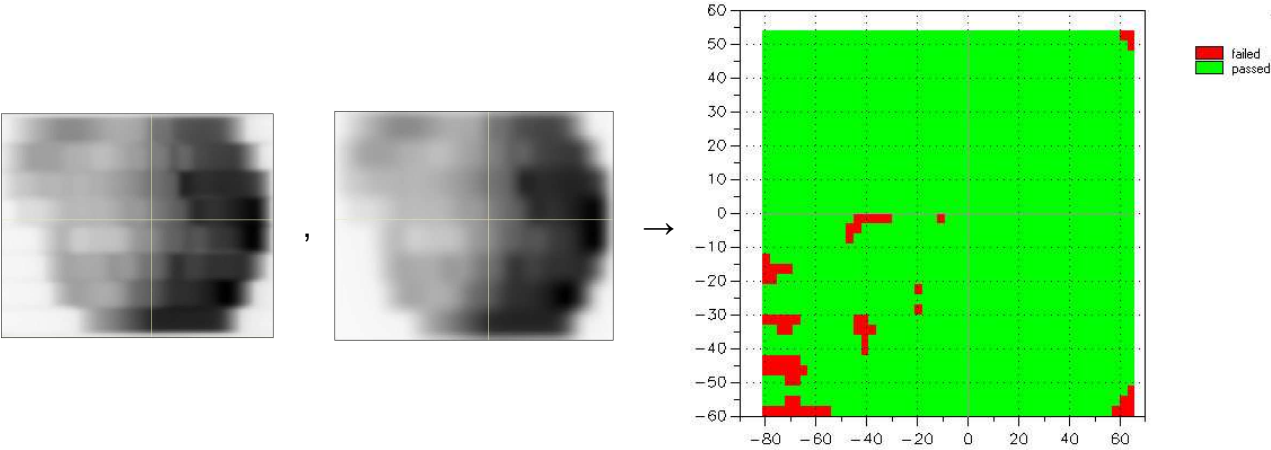
FIG. 128,   *Patient 6, field 5: measured matrix, planned matrix → gamma evaluation*

2.3.6.6   Field 6
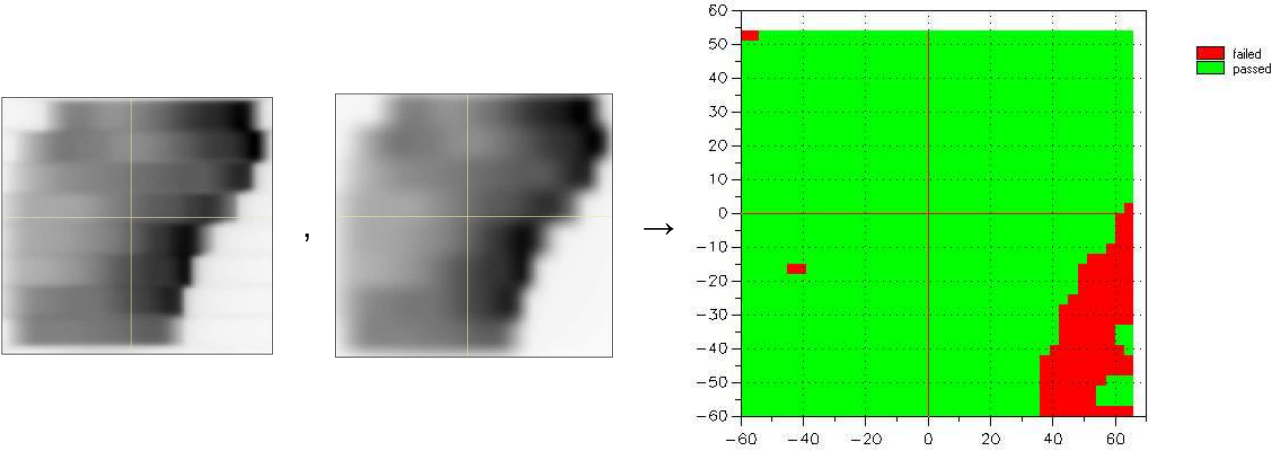
FIG. 129,   *Patient 6, field 6: measured matrix, planned matrix → gamma evaluation*

Discussion

While Cozzi et al. (2004) [3] were measuring at an SSD of 100 cm in a water depth of 10 cm this work does not try to reproduce a dose distribution inside the body, but the chosen measurement geometry accommodates the fact, that exit beam dosimetry will probably be available in clinical routine soon. Therefore the SSD is set to 145 cm and no build-up material is used above the EPID, except layers which are part of the device itself. The whole planning procedure for the verification is based on CT slices, produced at the institute's CT scanner General Electric Prospeed Power SX after the EPID has been demounted, and does not include any computer generated waterphantoms. In fact there have been plans which used a waterphantom with 0.8 cm of water above the detector layer and 2.5 cm below [28], but these plans should reproduce the EPIDs geometry to verify the dose matrices extracted from the EPID CT based plan. This comparison was done because it was not clear if the EPID CT images are appropriate to be used as a base for a planning procedure since the images contain artefacts caused by metal parts of the EPID. The comparison between the plans based on the phantom and the plans based on the EPID CT, showed good agreement and therefore all further reference dose distributions were extracted from plans based on the EPID CT slices. The result of this comparison confirms the information, which Varian gives about the thickness of water equivalent material above and below the detector layer of the EPID [28].

The measurement of a relative depthdose curve with the EPID, where the water depth was simulated by RW3 slabs and the EPID was moved vertically between the measurements to keep the SSD constant, does not correspond with Varians information, because the result of this measurement is a build up layer between 1.6 cm and 1.8 cm thickness above the detector layer. But this deviation can be relativized by considering that Varian announces the depth of maximum dose to be 3.0 ± 0.2 cm for 15 MV photons [24] and that the measured curve does not show a clear maximum but a plateau with a width of 0.5 cm. The plateau is still much smaller than the plateaus described by van Esch et al. (2004) [30] measured in tissue maximum ratio curves showing a width of approximately 3 cm.

The good results in the linearity measurements and the increasing deviation below 20 MU is in good accordance to van Esch et al. (2004) [30], to Greer (2007) [6] and slightly better than McCurdy et al. (2001) [10] who all three used a Varian aS500

EPID for their measurements.

All measured IMRT plans were compared to the planned fluence matrices by the gamma evaluation method. Since there is no international consensus (yet) which values should be used for DTA and relative dose comparison, in this work 4 %/ 4 mm were used for gamma evaluation of the real patient plans according to Cozzi et al. (2004) [3] and Dinesh et al. (2006) [4].

Even though the results look very promising, there is still one question left:

Are the deviations between measurement and plan due to problems in the image acquisition of the EPID or is the MLC not simulated properly by the software to calculate dose distributions in the EPID?

Interleaf leakage for example is considered in the calculation as an average value but the measurement results show clearly that this additional dose is deposited in the areas of leaf edges and not in between. This effect is stronger in areas where the deposited dose is small, because the gamma evaluation criterion is defined for relative doses.

Another deviation between the planned and the measured dose distributions occurs in areas where no dose distribution was planned but cannot be shielded by the collimators due to a non-rectangular field shape. These very low dose areas in the measurement do not agree with the planned dose distributions.

Responsible for most dose points which did not pass the gamma evaluation are these two effects, mentioned above.

But apart from these two effects, which have their origin in an inadequate simulation, the question mentioned at the beginning cannot be answered without further investigations. There might be more attributes of the MLC which are not simulated properly.

During months of measurements with the EPID at different vertical positions, the exactness of the retractable arm, on which the EPID is mounted, apparently became a weak point. Contrary to the retractable arm's manual, the arm lost its calibration in all three dimensions after some time without any notice on the handheld display. It was also not predictable if the arm would stop at preselected coordinates because the movement of the arm was very imprecise. This, of course, had an impact on the measured images, because horizontal deviations affect the position of the image and vertical deviations result in a slightly different image size. Both effects corrupt the results of the gamma evaluation.

Additionally the metal parts of the EPID, which produce artefacts in the CT images are another cause of uncertainty. But these artefacts do not influence the grey values of the CT images in an area of 15 cm around the beam centre and since IMRT fields are usually not very large this effect should not influence the verification process.

Besides these minor difficulties it became clear, that the EPID is a very powerful tool for all kinds of quality assurance measurements, which had to be performed with the use of films before. Nowadays most x-ray departments in hospitals switch to digital imaging and processing machines become rare in hospitals. This fact, the fact that the EPID is able to perform absolute dose measurements after calibration and an enormous time saving factor, are arguments for the use of an EPID.

Conclusion

The use of an amorphous silicon based EPID for verification of IMRT plans is a good choice. It combines the advantage of film, the high spatial resolution, and the advantage of an array of ionization chambers, the capability to perform absolute dosimetric measurements. The absence of an additional device for dose measurements simplifies the workflow and the whole verification process is less time-consuming. The result that an amorphous silicon based EPID is capable to perform quality assurance measurements and pre-treatment IMRT plan verification is in agreement with many other publications like van Esch et al. (2004) [30], Menon et al. (2004) [12], Warkentin et al. (2003) [34], Patridge et al. (1998) [14] and many more.

References

[1]   Aiginger H. and Poljanc K.: lecture notes: Strahlenphysikalische Methoden in der Medizin, TU-Wien, 2008.

[2]   Bortfeld T., Schmidt-Ullrich R., De Neve W. and Wazer D. E. (editors): Image-Guided IMRT. Springer-Verlag, Berlin Heidelberg, 2006.

[3]   Cozzi L., Fogliata A. and Nicolini G.: Pre-treatment verification of intensity modulated photon beams with films and portal imaging – Two years of clinical experience. Med. Phys. 2004;14: 239-215.

[4]   Dinesh Kumar M., Thirumavalavan N., Venugopal Krishna D. and Babaiah M.: QA of intensity-modulated beams using dynamic MLC log files. Journal of Medical Physics 2006;31: 36-41.

 [5]   Grahn H. T.: Introduction to Semiconductor Physics, World Scientific Publishing Co., 1999.

[6]   Greer P. B.: Off-axis dose response characteristics of an amorphous silicon electronic portal imaging device. Med. Phys. 2007;34: 3815-3824.

[7]   Hendee W. R., Ibbott G. S.: Radiation Therapy Physics. Mosby-Year Book, Inc., St. Louis, MO, USA, 1996.

[8]   Kahn F. H.: The Physics of Radiation Therapy. Williams & Wilkins, Baltimore, Maryland, MD, USA, 1994.

[9]   Low D. A., Harms W. B., Mutic S. and Purdy J. A.: A technique for the quantitative evaluation of dose distributions. Med. Phys. 1998;25: 656-661.

[10]   McCurdy B. M. C., Luchka K. and Pistorius S.: Dosimetric investigations and portal dose image prediction using an amorphous silicon electronic portal imaging device. Med. Phys. 2001;28: 911-924.

[11] Macian R.: EPFL Doctoral Course PY-031: Radioisotope and Radiation Applications. École Polytechnique Fédérale de Lausanne, http://lrs.web.psi.ch/educational/courses/2006_EPFL_DOCTORAL_PSI_COURSE/week5/Week_5_Lecture_09_Radiobiology.pdf, 11.08.2008

[12] Menon G. V., Sloboda R.S.: Quality assurance measurements of a-Si EPID performance. Medical Dosimetry 2004;1: 11-17.

[13] Nijsten S. M. J. J. G., van Elmpt W. J. C., Jacobs M. et al.: A global calibration model for a-Si EPIDs used for transit dosimetry. Med. Phys. 2007;34: 3872-3884.

[14] Patridge M., Evans P. M., Mosleh-Shirazi A. and Convery D.: Independent verification using portal imaging of intensity-modulated beam delivery by the dynamic MLC technique. Med. Phys. 1998;25: 1872-1879.

[15] Pongratz P.: lecture notes: Festkörperphysik 2, TU-Wien.

[16] PTW Freiburg: Manual 2D-ARRAYseven29, 2006

[17] PTW Freiburg: Manual Universal Dosimeter PTW-UNIDOS, Firmware 2.20 or higher.

[18] PTW Freiburg: Ionizing Radiation Product Catalog, Edition 2003/2004.

[19] PTW Freiburg: Spec sheet: Ionization Chamber Type 30010.

[20] PTW Freiburg: Spec sheet: Ionization Chamber Type 31014.

[21] PTW Freiburg: webpage: http://www.ptw.de/2d-array_seven29.html?&L=0, 28.07.2008

[22] Rad-icon Imaging Corp.: AN07: Scintillator options for Shade-o-Box cameras http://www.rad-icon.com/pdf/Radicon_AN07.pdf, 10.06.2008.

[23]   University of Cambridge, Teaching and Learning packages: Introduction to semiconductors   http://www.doitpoms.ac.uk/tlplib/semiconductors/index.php, 05.06.2008.

[24]   Varian Medical Systems: CLINAC 2300C/D Equipment Specifications, 1992.

[25]   Varian Medical Systems: CLINAC 2300C/D - The New Gold Standard for Radiation Therapy, 1992.

[26]   Varian Medical Systems: Image Acquisition System 3 Reference Guide, 2007.

[27]   Varian Medical Systems: Portal Imaging and Portal Dosimetry Reference Guide, 2008.

[28]   Varian Medical Systems: Preliminary: Varian IMRT School, Berlin, December 2007.

[29]   Varian Medical Systems: Retractable Arm Operator Manual, October, 1994.

[30]   Van Esch A., Depuydt T. and Huyskens D. P.: The use of an aSi-based EPID for routine absolute dosimetric pre-treatment verification of dynamic IMRT fields. Radiotherapy & Oncology 2004;71: 223-234.

[31]   Van Dyk J. (editor): The Modern Technology of Radiation Onclology. Medical Physics Publishing, Madison, WI, USA, 1999.

[32]   Van Zeghbroeck B.: Principles of Semiconductor devices
http://ece-www.colorado.edu/~bart/book/, 12.06.2008.

[33]   Wannenmacher M., Debus J. and Wenz F. (editors): Strahlentherapie. Springer-Verlag, Berlin Heidelberg, 2006.

[34]   Warkentin B., Steciw S., Rathee S., et al.: Dosimetric IMRT verification with a flat-panel EPID. Medical Physics 2003;30: 3143-3155.

[35]   Webb S.: Intensity-Modulated Radiation Therapy. Institute of Physics Publishing, Bristol and Philadelphia, USA, 2001.

List of Figures

List of Tables

Curriculum Vitae

Lukas Jägerhofer

Komarigasse 17b

2700 Wiener Neustadt

Born at August, 3rd 1981 in Vienna, Austria

Education:

- University of Technology Vienna (2000-2008)
- Secondary and High school (1991-1999)
- Primary School (1986 – 1991)

Publications:

- September 2005: Co-Author of Poster-presentation at the Conference of the Austrian Physical Society CERN-IH Linac verification via CERN DYNAC-source code
- Sannibale F., Baptiste K., Barry W., Chin M., Filippetto D., Jaegerhofer L., Julian J., Kwiatkowski S., Low R., Plate D., Portmann G., Robin D., Scarvie T., Stupakov G., Weber J., Zolotorev M.: Recent beam measurements and new instrumentation at the Advanced Light Source. 2008 Beam Instrumentation Workshop, Tahoe City, CA USA, May 2007. LBNL-661E.

Work experiences:

- Summer 2007: Lawrence Berkeley National Laboratory – 2 months Student Assistant in ALS Physics Division

Special education:

- January 2008: special course "Fundamentals of Storage Ring Design"
- January 2008: special course "Magnetic Systems: Insertion Device Design"
  Both at the US Particle Accelerator School in Santa Rosa, CA
  (URL: http://uspas.fnal.gov/)
- January 2006: special course "Fundamentals of Accelerator Physics" at the US Particle Accelerator School in Phoenix, AZ
  (URL: http://uspas.fnal.gov/)